VILNIUS UNIVERSITY

CENTER FOR PHYSICAL SCIENCES AND TECHNOLOGY

EVA RAUDONYTĖ-SVIRBUTAVIČIENĖ

LIGHT INDUCED SYNTHESIS OF CERIA BASED MATERIALS AND THEIR APPLICATIONS FOR PHOTOCATALYSIS

Doctoral Dissertation

Physical Sciences, Chemistry (03 P)

Vilnius, 2018

VILNIAUS UNIVERSITETAS

FIZINIŲ IR TECHNOLOGIJOS MOKSLŲ CENTRAS

EVA RAUDONYTĖ-SVIRBUTAVIČIENĖ

CERIO OKSIDO NANODALELIŲ IR NANOHETEROSTRUKTŪRŲ SU PLAZMONINĖMIS NANODALELĖMIS FOTOCHEMINĖ SINTEZĖ BEI GAUTŲ DARINIŲ PRITAIKYMAS FOTOKATALIZĖJE

Daktaro disertacija

Fiziniai mokslai, Chemija (03 P)

Vilnius, 2018

The dissertation was carried out in Vilnius University in the period 2013-2017.

Scientific supervisor:

Assoc.Prof. Dr. Artūras Katelnikovas

(Vilnius University, Physical Sciences, Chemistry 03P)

Scientific consultant:

Prof. Dr. Thomas Jüstel

(Münster University of Applied Sciences, Physical Sciences, Chemistry 03P)

Table of Contents

LIST OF ABBREVATIONS

Arb. Unit	Arbitrary Unit
BF	Bright Field
DET	Direct Energy Transfer
DLLME	Dispersive Liquid-Liquid Microextraction
DOS	Density of States
DTG	Differential Thermogravimetry
E^0_{CB}	Conduction Band Electron
E^0_{VB}	Valence Band Hole
E_g	Band Gap
EM	Electromagnetic
EtOH	Ethanol
FTIR	Fourier Transform Infrared Spectroscopy
FWHM	Full Width at Half Maximum
GC	Gas Chromatograph
HAADF	High Angle Annular Dark Field
LED	Light Emitting Diode
LSPR	Localized Surface Plasmon Resonance
MIEC	Mixed Ionic-electronic Conductivity
MS	Mass Spectrometer
NHE	Norma Hydrogen Electrode
NIR	Near-infrared
NPs	Nanoparticles
NRs	Nanorods
OSC	Oxygen Storage Capacity
OV	Oxygen Vacancies
PSP	Propagating Surface Plasmon
PTFE	Polytetrafluoroethylene
PVP	Poly (N-vinylpyrrolidone)
SEM	Scanning Electron Microscopy
SIM	Selected Ion Monitoring
SP	Surface Plasmon
SPB	Surface Plasmon Absorption Band
SPR	Surface Plasmon Resonance
STEM	Scanning Tunneling Electron Microscopy
TBT	Tributyltin
TEM	Transmission Electron Microscopy
TG	Thermogravimetry
UV/VIS	Ultraviolet/Visible
VUV	Vacuum Ultraviolet
XPS	X-ray Photoelectron Spectroscopy
XRD	X-ray Diffraction

Chapter1. Introduction

With industrialization and population growth, the environmental contamination caused by organic pollutants is becoming a major concern all over the world. Decontamination of anthropogenic organic pollutants, particularly those with high toxicity but at relatively low concentration, is an overwhelming challenge which is not possible to overcome by applying conventional biological and physical treatment methods. Among numerous approaches, chemical utilization of clean and sustainable solar energy through photocatalysis has been perceived as one of the most promising methods [1, 2].

1955 is considered as a year when photoelectrochemistry has started with Brattain's electrochemical studies on germanium electrolyte junction [3]. Numerous researches in the field followed later on with the discovery of water photoelectrolysis at illuminated TiO_2 electrodes being reported by Fujishima and Honda in 1971 [4, 5], which established the use of photoelectrochemical cells for 'artificial photosynthesis'. In 1981, Nozik assumed that the basic functions of a photoelectrosynthetic cell could be copied in suspended micro- or nanoscale particles and formulated the concept of 'photochemical diodes' [6]. Ever since, a remarkable progress has been made in the area of nanoscale photoelectrochemistry with semiconducting nanomaterials being almost exclusively applied as photocatalysts for various chemical transformations induced by UV or visible light [7-10].

The majority of photocatalytic studies have been, however, focused on titanium dioxide (TiO_2) and zinc oxide (ZnO) based materials mainly, with comparatively sparse reports on other n-type semiconductors [8, 11]. To this end, the quest of a diverse set of high-performance photocatalysts is beneficial for both fundamental and applied photocatalyses, especially taking into consideration some recent studies revealing TiO_2 and ZnO biological effects and potential damage to the marine populations [12-15].

Ceria (CeO_2), besides being reported to be less toxic than ZnO and TiO_2 and even to induce cellular resistance to an exogenous source of oxidative

stress [16, 17], is also known for its stability at high temperatures, UV absorption ability, and, most interesting, the oxygen storage activity [18-20]. In particular, ceria is a unique catalyst which can take and release oxygen through reversible shifts between Ce^{3+} and Ce^{4+} [21] thus modifying the catalytic performance of the elements combined to it by either providing to or withdrawing oxygen from them [22]. All this brands CeO_2 a potential substitute for TiO_2 or ZnO.

The main disadvantage of semiconductor photocatalysts is, undoubtedly, their limited solar-energy-conversion efficiency as UV region represents only ~4% of the solar spectrum [23]. One of the possible attempts to overcome this problem could be the incorporation of plasmonic metal nanostructures into semiconductors which could result in extended light absorption to longer wavelengths, increased light scattering and additional excitation of electron−hole pairs in the semiconductor [24-26].

The motivation of this work was to prepare and characterize Ag-CeO_2 nanoheterostructure, a potential novel photocatalyst with the visible light activity, via photochemical inorganic synthesis. The proposed photochemical approach enables to produce silver - semiconductor system without employing organic stabilizers and additives, thus resulting in formation of nanoparticles with “clean”, highly reactive metal surface. The tasks of the present thesis were formulated as follows:

1. To synthesize ceria nanoparticles via an inorganic photochemical route using sodium azide as a photoactive material;
2. To characterize the obtained products and find the optimum synthesis conditions seeking to further apply ceria NPs for the preparation of Ag-CeO_2 nanoheterostructures;
3. To synthesize Ag-CeO_2 nanoheterostructures via inorganic photochemical route;
4. To examine photocatalytic activity of the obtained nanoparticles and nanoheterostructures on the photocatalysis of tributyltin (TBT).

Statements for defense:

1) Sodium azide may be used as a photoactive material for preparation of nanoscale CeO_2 particles in aqueous solutions.
2) Crystallite size of CeO_2 nanoparticles is radiation dose exposure, surfactant concentration and post-synthetic heat-treatment temperature dependent. Shorter irradiation time and higher surfactant concentration result in the formation of smaller particles while increasing the calcination temperature leads to the formation of significantly larger particles.
3) Ag-CeO_2 nanoheterostructures can be prepared via inorganic photochemical synthesis route with ceria nanoparticles serving both as a photoactive material and a metal nanoparticle support. Ceria ability to generate conduction band electrons after being irradiated with UV radiation is playing a key-role in the reduction of silver ion.
4) Ethanol enhances the reduction process by an efficient radical/hole scavenging and the additional silver ion reduction by the emerging $H_3CHC•OH$ radicals.
5) Silver nanoparticle size, shape, and oxidation state depend on concentration of the silver precursor, irradiation time and the presence of radical/hole scavenger.
6) Ceria nanoparticles show no visible light photocatalytic activity while samples containing silver exhibit photocatalytic activity on TBT degradation under visible light irradiation. Both ceria nanoparticles and Ag-CeO_2 nanoheterostructures show photocatalytic activity on TBT degradation under UV radiation irradiation. Samples containing silver are more efficient even in UV radiation driven photocatalysis.

Chapter 2. Cerium and cerium oxide nanoparticles: properties, electronic structure and nano-size effects

Among the rare earth family, cerium (Ce) is the most abundant element, although the exact values of crustal abundance are still quite controversial. However, the value of 66.5 ppm, representing the median of the various reported values, is usually accepted as a most reliable [27]. This means that cerium is more plentiful in the Earth's crust than copper (60 ppm) or tin (2.3 ppm) [27]. Cerium belongs to the lanthanide group and has an atomic number of 58. The electron configuration of cerium is [Xe] $4f^1 5d^1 6s^2$ with two common valence state cerium(III) and cerium(IV) [28].

CeO_2-based materials play an essential role in environmental and energy related applications as ceria is one of the most reactive rare earth oxides with a wide optical band gap (E_g ~ 3.19 eV for the bulk material) and a high dielectric constant ($\mathcal{E}$ = 23 – 26) [29, 30], possessing unique properties, such as strong UV absorption [31, 32], stability at high temperature (melting point ~2500 °C; boiling point ~3500 °C) [33], and high oxygen ion conductivity [34]. Therefore, it is widely applied in many technical fields, viz. catalysts/catalyst supports [35], UV absorbents [36, 37], and chemi-sensors [38]. Similar to the yttria stabilized zirconia, cerium oxide can accommodate a high oxygen deficiency by the substitution of lower valence elements on the cation sublattice, resulting in a high oxygen ion conductivity and potential applications in solid oxide fuel cells [18, 39-41]. At the same time, CeO_2 is also well known to release significant levels of oxygen at reduced oxygen partial pressures and elevated temperatures, which leads to a mixed ionic-electronic conductivity (MIEC) [18].

2.1. Electronic structure of ceria

Cerium, as well as other heavy metals such as Yb [42], Eu [43] and Sm [44], belong to an exciting class of materials that have extraordinary properties arising from their partially filled valence shell [45, 46]. It was revealed that not only does the appearance of different phase transitions change the distribution of the valence electrons under extreme conditions [43, 47], but it can also be linked to the formation of mixed valence states [44, 48].

Cerium has the $[Xe]4f^{1}5d^{1}6s^{2}$ electronic configuration, exhibiting a 4+ oxidation state in the CeO_2 fluorite phase [49]. Ce^{4+} and O^{2-} ions have closed shells with the electronic structure of Xenon and Neon, respectively. In a perfectly stoichiometric CeO_2, all of Ce 6s, 5d and 4f valence electrons leave the host atoms and are donated to the oxygen atoms [28]. Empty Ce 4f states are present in a stoichiometric CeO_2 while deviations from the ideal bulk stoichiometry CeO_2 lead to the reduction of Ce^{4+} ions to Ce^{3+} and to the occupied electronic Ce $4f^{1}$ states within the band gap [50]. It was suggested by Skorodumova *et al*. that the mechanism of the CeO_2-Ce_2O_3 reduction simultaneously involves the formation of an oxygen-vacancy and the localization of an 4f electron on the Ce atom [28].

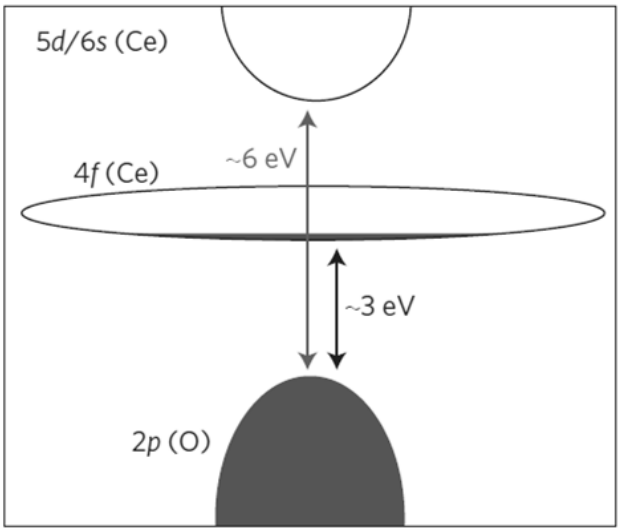

Figure 1. *Schematic electronic structure of CeO_2. Reprinted from reference [51].*

In fact, CeO_2 is known to contain some oxygen vacancies and thus the oxide of mixed oxidation states is forming, denoted as CeO_{2-x}. As a result, the ground state of 4f orbitals is believed to be a mixed valence state of 4f 0 and 4f 1$\underline{v}$ contributions (where $\underline{v}$ denotes a hole in a ligand orbital) [52]. In the case of oxygen-deficient CeO_{2-x}, increased $f^1\underline{v}$ contribution in the presence of strong orbital mixing and an unchanged ^1S spin orbit state can be observed [53]. 4f state is positioned in a wide band gap of cerium oxide (*Figure 1*, *Figure 2*). It was observed that the position of Ce 4f-block band with respect to the Ce 1s core level is almost identical for different cerium compounds, implying thus a strong localization of the 4f level [54].

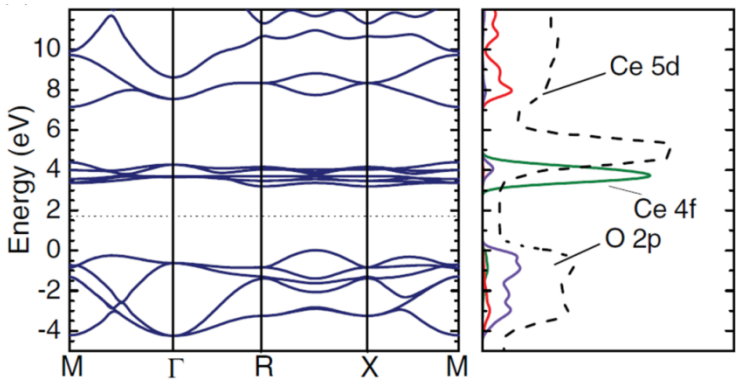

Figure 2. *Band structures and density of states (DOS) of CeO_2 as calculated from the HSE06 exchange-correlation functional. The dashed grey lines in the DOS plots depicts the experimentally measured DOS from reference [55] for comparison. The valence band maximum was chosen as the zero energy. The dotted line in the band structure plot depicts the Fermi energy. Adapted from reference [52].*

Gillen *et al*. have calculated the electronic structures of lanthanide oxides using hybrid density functionals HSE03, HSE06 (Hartree-Fock exchange) and screened exchange (sX-LDA). CeO_2 was modeled by the three atom primitive cell of the cubic fluorite structure (space group $Fm\bar{3}m$). *Figure 2* presents results of the calculated band structures for the hybrid functional HSE06. In their research, depending on the functional applied, the evaluated *2p-4f* band gap is reported to range between 1.5 – 4.2 eV (experimentally determined to be around 3.00 eV) [54, 56] while the *2p-5d/6s* band gap varies from 6.2 to 7.2 eV (experimentally determined in the range of 5.5–8 eV) [52, 55].

2.2. Material properties and defects of ceria

CeO_2 has the cubic fluorite crystal structure with the space group $Fm\bar{3}m$ over the whole temperature range from room temperature up to the melting point [57]. The fluorite structure consists of a face-centered cubic (f.c.c.) unit cell of Ce^{4+} cations with O^{2-} anions occupying the octahedral interstitial sites, each O^{2-} is coordinated to four Ce^{4+} as shown in *Figure 3*. It can also be described as a superposition of the f.c.c. lattice of cations (Ce^{4+}) with the lattice constant *a*, and a simple cubic lattice of anions (O^{2-}) with lattice constant *a*/2.31. Each cerium cation is coordinated by eight adjacent oxygen anions, while each oxygen anion is coordinated by four adjacent cerium cations. The cation sublattice is a superstable frame because of the ionic bonding [58]. Due to Ce(IV)–O(II) charge transfer, the color of CeO_2 is pale yellow, while for nonstoichiometric $CeO_{2-\delta}$ ($0<d<0.5$), it varies from blue to almost black [18, 57]. The experimentally determined lattice parameter of ceria is 5.411 Å [59].

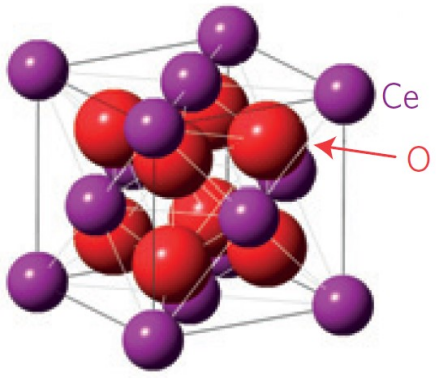

Figure 3. *The crystal structure of ceria. Reprinted from reference [51].*

Chemical and electronic properties of ceria are mainly dominated by the defects, such as dislocations and oxygen ion vacancies, the latter are believed to play a significant role in reactivity of the ceria surface for the catalytic oxidation of carbon monoxide [60, 61]. Because of their redox capability, cerium oxides are excellent oxygen buffers. With alterations in the cerium

oxidation state, CeO_2 forms oxygen vacancies (OV) or defects in the lattice structure by the loss of oxygen. The dynamic valence and defect structure of CeO_2 is capable of changing spontaneously or in response to physical parameters, such as oxygen partial pressure, temperature and doping with other ions, as well as surface stresses or applied electrical field [49, 62]. The capability of rapidly forming oxygen vacancy defects provides ceria with a high oxygen storage capacity (OSC) [63].

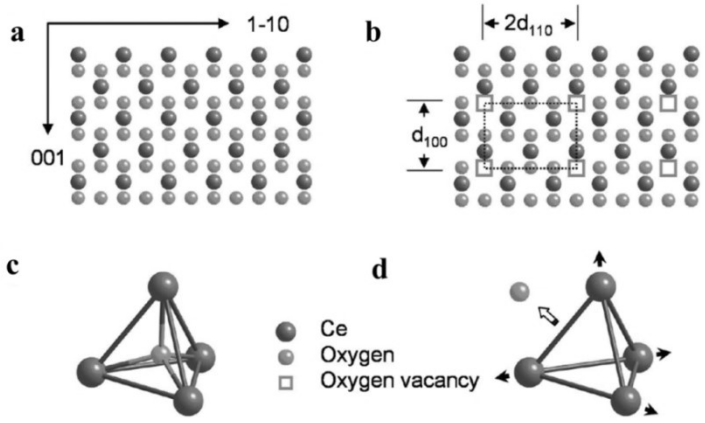

Figure 4. *(a) Model of CeO_2 in a perfect fluorite structure (projection along the ⟨110⟩ direction). (b) Model showing formation of oxygen vacancies. The rectangles indicate the vacancy superlattices. (c) Cerium oxide could be viewed as tetrahedrons with cations at the vertexes and oxygen anions at the centers. (d) Cerium oxide with an oxygen vacancy. The arrowhead indicates the displacement direction of the oxygen anion. Reprinted from reference [49].*

The structural model for the process of forming ordered oxygen vacancies is presented in *Figure 4*. A perfect fluorite structure is shown in *Figure 4* (a) while the rectangle in *Figure 4* (b) represents the unit cell of the CeO_2 sesquioxide resulting from ordered oxygen vacancies. Since oxygen has an oxidation state of -II in the stoichiometric CeO_2, when the vacancy is created, two electrons are left. Charge compensation occurs through the formation of polarons: the left-behind electrons are localized on trivalent cerium cations. High density of oxygen vacancy defects is believed to be responsible for the increase in ceria Ce^{3+} fraction. Cerium oxide could be viewed as tetrahedrons,

as in *Figure 4* (c). In cerium oxide with an oxygen vacancy, CeO_2 film cations are believed to repel each other along the direction indicated in *Figure 4*(d) because of the Coulomb interactions [49]. The increasing distance between cations forms a pathway for the further migration of oxygen anions.

It is assumed that oxygen vacancies participate in many chemical reactions catalyzed by metal oxides. Groups of exposed Ce^{3+} ions on CeO_2 are potentially preferred surface sites for catalysis and photocatalysis as vacancies are known to bind basic adsorbates more strongly and assist in their dissociation than normal oxide sites [64].Because of oxygen vacancy defects, ceria has the oxygen storage capacity, that is, it can act as an oxygen buffer to store oxygen under oxygen-rich environment and release oxygen under oxygen-lean environment [65].

2.3. Nano-size effects in ceria

Nanostructured CeO_2 materials demonstrate extraordinary properties with respect to the bulk material. It is well known that reducing the size of CeO_2 to the nanometer scale enhances the chemical activity as well as redox and transport properties remarkably. Properties of the material can change drastically with the particle size decreasing to the nanosize region [53, 66, 67]. For instance, catalytic activity of Au supported on CeO_2 NPs was reported to be by two orders of magnitude higher if compared to Au deposited on a regular bulk cerium oxide support [66]. Vayssilov *et al*. noticed that the size of CeO_2 nanoparticles plays a critical role in catalytic activity of supported Pt NPs [68].

The increased catalytic activity could be related to the larger surface to volume ratio present in nanostructures. In the case of ceria, however, this effect is of more complex origin. It was revealed by Guzman *et al*. that nanocrystalline CeO_2 is responsible for the supply of reactive oxygen [67], implying thus the importance of oxygen vacancies to the catalytic reactions. Indeed it is stated by the generally advocated mechanism that particle miniaturization resulting in an increase of the surface to bulk ratio increases

significantly nonstoichiometric $CeO_{2-\delta}$ owing to surface oxygen vacancies. It is assumed that oxygen vacancy formation energy (E_f) in ceria crystallites of a particular size becomes lower than that in extended structures [69]. Defects tend to form close to the surface charge layer which is much easier accessible in the nanostructure than in the extended structures. Due to this and enlarged density of interfaces in nanocrystalline solids [18], remarkably increased levels of non-stoichiometry and electronic carrier generation are likely to occur [70]. Electrons left behind by oxygen vacancy formation are responsible for Ce^{4+} reduction to Ce^{3+} ions, leading to a higher level of catalytically active Ce^{3+} ions at the surface that are also responsible for the increased chemical activity of nanoceria if compared to bulk ceria [71]. It was observed that the content of Ce^{3+} and oxygen vacancies decreases with growth and oxidation of the nanoparticles (with grains of 10 – 20 nm) during annealing in an O_2 rich atmosphere [72].

Chapter 3. Plasmonic nanoparticles and surface plasmon resonance

NPs of some noble metals, such as silver (Ag) and gold (Au), are known to exhibit extraordinary colors, which have been found to depend on both the particle size and shape. The light absorption property, demonstrated by gold NPs, has been applied to adorn some of the most splendid stained glass windows of medieval churches for centuries [73]. These magnificent colors are the result of the localized surface plasmon resonance (LSPR) effect of the noble metal NPs [10].

In general, plasmonic metal nanostructures can be differentiated based on the plasmonic mode supported: localized surface plasmon resonance or propagating surface plasmon polaritons (PSPs), also called propagating surface plasmons [74]. Both LSPR and PSP strongly depend on the refractive index of the surrounding medium, which is the basis of plasmonic sensors.

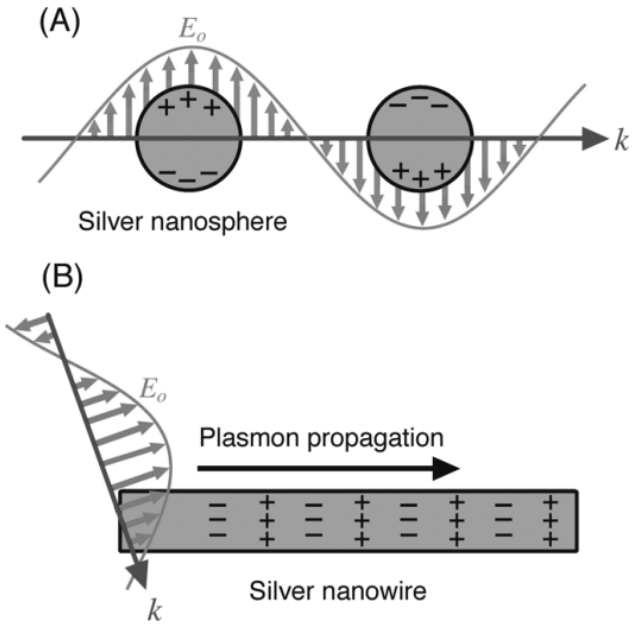

Figure 5. *Two types of plasmonic nanostructures as excited by the electric field (E_o) of incident light with wavevector (k). (A) The nanostructure is smaller than the wavelength of light: free electrons collectively oscillate in resonance with the light (LSPR). (B) One dimension of the nanowire is larger than the wavelength of light: a propagating surface plasmon (PSP) can travel along the surface of the metal nanostructure. Reprinted from reference [75].*

LSPR occurs when the dimensions of a metallic nanostructure are much smaller than the wavelength of the incident light since it is an essential condition to experience a uniform E_o if excited by light. Hence, LSPR is generally observed in metal nanoparticles or nanostructured metal surfaces. In contrast to PSP, LSPR is known to concentrate the incident electromagnetic (EM) field around the nanostructure [76].

PSPs are supported by structures that have at least one dimension approaching the excitation wavelength and is generally attributed to the oscillations of free electrons in thin metal film. In this case, the E_o is not uniform across the structure, it propagates back and forth between the ends of the thin film. Reflection from the ends of the structure, which can change the phase and resonant length, must also be considered. Propagation lengths can be in the tens of micrometers (for nanowires), and, by controlling the geometrical parameters of the structure, the PSP waves can be manipulated [77, 78].

3.1. Localized surface plasmon resonance

According to Mie's theory, the localized surface plasmon resonance is the resonant photon-induced coherent oscillation of charges at the metal–dielectric interface established when the photon frequency matches the natural frequency of the metal surface electrons oscillating against the restoring force of their positive nuclei [10, 79]. In other words, LSPR is made up of collective oscillations of free electrons in metal NPs caused by the electromagnetic field of incident light and it is the main reason why metallic nanoparticles absorb visible and infrared light in particular regions [80]. LSPR is only exhibited by nano-sized particles and is not observed within bulk metals or clusters that are smaller than 2 nm as well as within single atoms [81, 82]. If the nanoparticle dimensions are smaller than the wavelength of light, the electron density will have uniform displacement across the particle surface and strong restoring force from the positive ionic core background.

The principle of LSPR can be briefly described as follows: after irradiation of the small metallic NP with a light which wavelength exceeds the NP size, the electron density decreases on one side of the NP and increases on the other side, causing redistributions of the charge density. Electric field inside and outside the metal NP is created by this distributed charge density with a direction opposite to that of the electric field of the light. One should not forget the Coulombic restoring force, which is caused by the oscillations in the NPs. The resonance between the oscillations and the incident light is known as the LSPR [82].

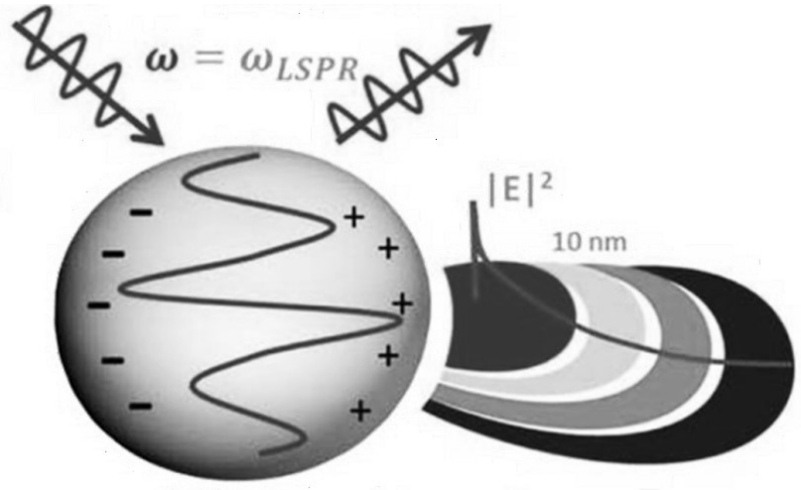

Figure 6. *Localized surface plasmon resonance exists when the metal nanoparticle is smaller than the incident wavelength, making the electron oscillations in phase. The collective oscillations lead to a large absorption and scattering cross section, as well as an amplified local EM field. Adapted from reference [76].*

The coherent oscillation of electrons in space and time leads to the confinement of photon energy to the surface of nanostructured materials for much longer time scales than photons would spend in the same control volume traveling at the speed of light. Hence, a large build up of photon intensity (strong electric fields) and a high concentration of energetic electrons at nanostructured surfaces is a result of LSPR excitation [83, 84].

The ability of a metal nanoparticle to support surface plasmon (SP) is dependent on its dielectric function, ε, which reflects the typical interaction between its electrons and light. The dielectric function consists of a real part (ε_r) and an imaginary part (ε_i), both of which vary with excitation wavelength (λ). The simplest way to describe LSPR can be found in Mie theory for calculating the extinction (absorption + scattering) cross section of a metal nanosphere [85]:

$$C_{ext} = \frac{24\pi^2 R^3 \varepsilon_m^{3/2}}{\lambda}\left[\frac{\varepsilon_i}{(\varepsilon_r + 2\varepsilon_m)^2 + \varepsilon_i^2}\right] \qquad \textbf{(1)}$$

where C_{ext} is the extinction cross section, R is the radius, and ε_m is the relative dielectric constant of the medium surrounding the nanosphere. The latter equation indicates that the interaction between light and a metal nanoparticle depends strongly on its dielectric properties (ε_r and ε_i).

Since most parameters, such as the environment and excitation wavelength, are usually fixed, material properties of the plasmonic structures play an essential role. When the denominator of the bracketed expression in eq 1 approaches zero, so called resonance condition would be reached with C_{ext} becoming extremely large and the optical absorption and scattering at this particular frequency becoming exceedingly strong. In order to achieve this, ε_r must be close to $-2\varepsilon_m$, which is impossible for standard nonmetals and dielectric materials, which ε_r values varies between 1 and 50 [86]. It is also shown by the equation 1 that ε_i should be close to zero to support a strong resonance [87]. To assume, large ε_i values are responsible for a weaker plasmon and it is impossible to form LSP or PSP sufficiently strong for plasmonic applications without a negative ε_r value.

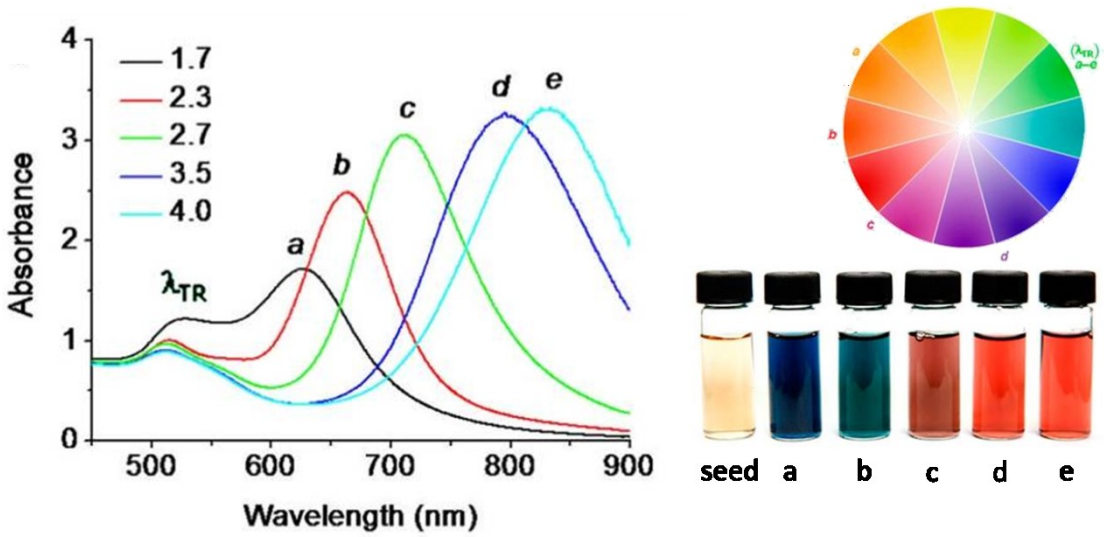

Figure 7. *Optical absorption spectra, optical images of gold nanorods with different aspect ratios and a color wheel, with reference to longitudinal resonance wavelength (λ_{LR}) and transverse resonance (λ_{TR}) for gold NRs labeled a–e. Adapted from reference [88].*

Not only is the LSPR band position sensitive to the changes in dielectric environment, it also depends on the shape and size of the nanoparticles [24]. The larger particles are, the lower repulsion for electrons at the opposite surfaces is established, and the more red-shifted LSPR band will be observed as can be seen from *Figure 7* [88, 89]. Nanoparticles of other shapes than spheres exhibit multiple resonant peaks due to the multipolar resonances in different directions [90]. For instance, the reduced symmetry of anisotropic gold nanorods results in longitudinal resonance (LR) and transverse resonance (TR). While the latter is not highly affected by the size of NPs, the first depends exceptionally on the aspect ratio (*Figure 7*) [91].

3.2. Silver nanoparticles for plasmonic applications

Silver is probably the most important material in plasmonics as it offers several advantages over other metals known to support SPR in the visible (VIS) and near-infrared (NIR) regions (Au, Cu, Li, and Al) [75]. As discussed in section 3.1., the extinction cross section depends strongly on the dielectric properties of the material and strong LSPR can only be supported by materials with the ε_i close to zero. ε_i and ε_r for Ag, Au, and Si are plotted in *Figure 8*. ε_i of silver is close to zero in a wide spectrum range.

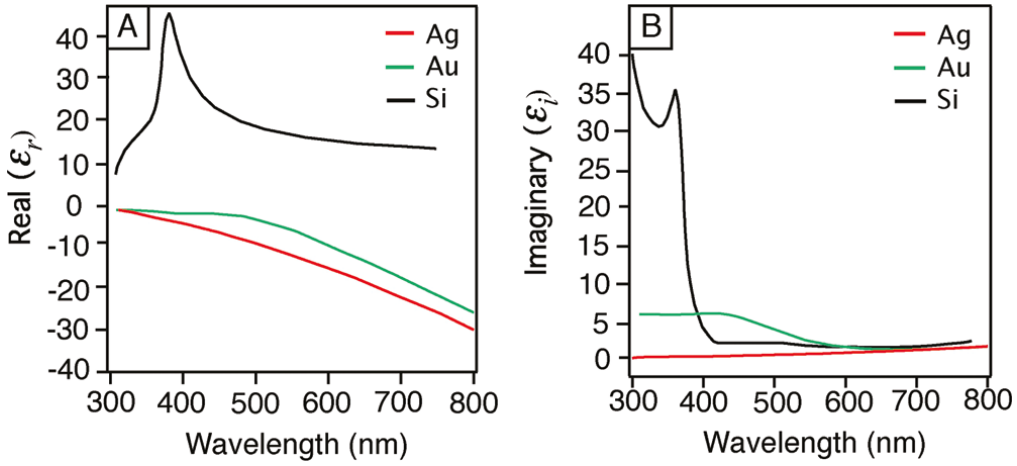

Figure 8. *Plot of the (A) real, ε_r, and (B) imaginary, ε_i, components of the dielectric function of Ag, Au, and Si as a function of wavelength. Reprinted from reference [75].*

The SP strength can be described using the quality factor (Q) [92]:

$$Q = \frac{w(d\varepsilon_r / dw)}{2(\varepsilon_i)^2} \qquad \textbf{(2)}$$

The SP strength is directly proportional to Q, small quality factor values indicate a lossy or weak SP with a small C_{ext}. For most of the plasmonic applications, Q should exceed ~10. It is obvious from *Figure 9*, presenting quality factors for some metals, that silver can support a strong SPR at the desired resonance wavelength due to its largest quality factor across most of the spectrum (from 300 to 1200 nm). Gold and copper are suitable for

plasmonic applications at longer wavelengths (above 600 nm) only. Aluminum, in contrast, has a high quality factor in UV region, where other metals generally have low *Q* values.

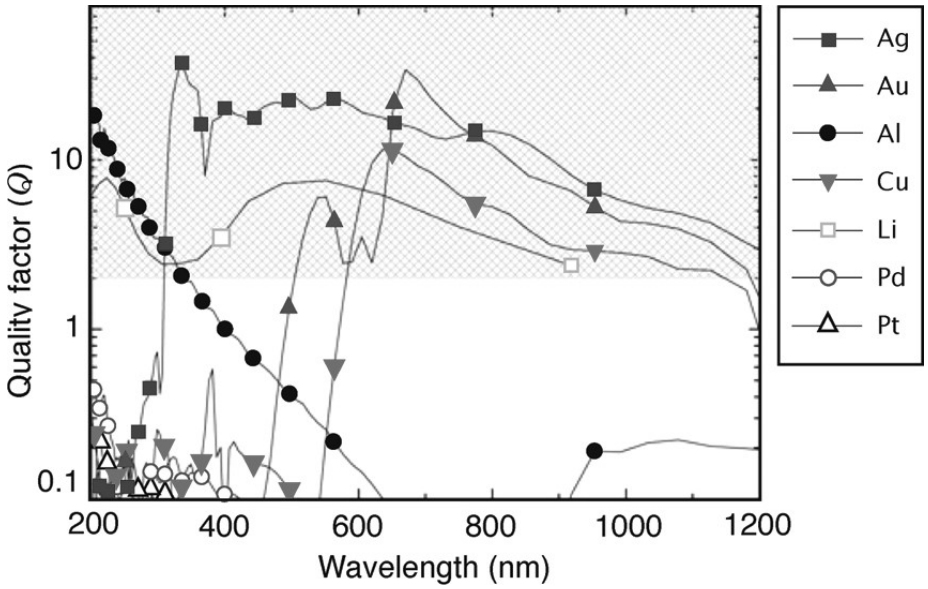

Figure 9. *Quality factor (Q) of the LSPR for a metal/air interface. A higher Q denotes less damping and a stronger plasmon resonance. The shaded area represents the region of interest for many plasmonic applications. Reprinted from reference [92].*

It is obvious from *Figure 9* that Li might generate high intensity LSPR in broad spectral region and thus it could be an attractive plasmonic material in theory. In practice, however, all of the properties must be taken into account and lithium could not be used for plasmonic applications due to its high reactivity. The use of copper is limited because of its higher tendency to be oxidized [75].

Chapter 4. Photochemical processes: from light-induced synthesis to photocatalysis

Light, although often being ignored, is a ubiquitous component in almost every chemical synthesis. It still remains an exotic tool for the control of particle shape, size and composition although, if compared to the conventional chemical approaches, light-mediated synthesis provides the advantages of a uniform distribution of the reducing agent in the entire solution, easy modulation of the power density, and tuning of the wavelength to maximize the absorption by chemical species present in the solution [93]. On the other hand, the utilization of solar energy for catalytic chemical transformations on surfaces has been considered as an environmentally friendly potential alternative to traditional thermally driven heterogeneous catalysis for decades [2, 4, 94].

4.1. Photochemical approach to the synthesis of semiconducting nanoparticles

Motivated by both the potential applications and formation of the desired properties, the development of efficient size-controlled semiconducting nanostructures synthesis methods is of great interest nowadays. A vast number of papers related to the topic of synthesis and properties of such nanoparticles have been published in the past decade. Different chemical procedures such as sol-gel [95, 96], solvothermal [97], electrochemical [98], hydrothermal [99, 100], sonochemical [101-103] and supercritical solvent methods [104, 105] have been employed to prepare ceria nanoparticles (NPs), to mention just a few. However, most of the techniques proposed are rather complex, energy consuming, and expensive synthetic strategies for nanoscale particle generation, requiring either the use of organic solvents (sol-gel, solvothermal, sonochemical processes) or/and expensive and sophisticated equipment (hydrothermal, electrochemical, supercritical solvent methods). Thus, precise

and uniform control of the particle size still remains a key challenge for the synthesis of ceria nanoparticles in aqueous solution.

In the case of the photochemical synthesis, the character of light is the main parameter, controlling the photochemical reactions. Taking into consideration the tight correlation between energy and wavelength of light, as well as its tunable intensity, it is clear that photochemical synthesis provides a unique synthetic tool that cannot be achieved by typical reducing agents and possess spatial and temporal control of the process [106]. Moreover, photochemical methods demonstrate good reproducibility and occur at room temperature in a closed vessel limiting the possibilities to introduce impurities [107]. Examples of some photoreactors are presented in *Figure 10*.

Light-mediated synthesis has proven to be an effective route for the preparation of a wide variety of nanomaterials with a precise control of the particle size [108-111]. Similar to the thermal methods, photochemistry also depends on the generation of reducing species during decomposition of carefully selected compounds. In a perfect system, these molecules do not demonstrate the reducing character unless they are photoexcited. The presence of the reducing moiety in the ground state would limit the spatial and temporal control of the process.

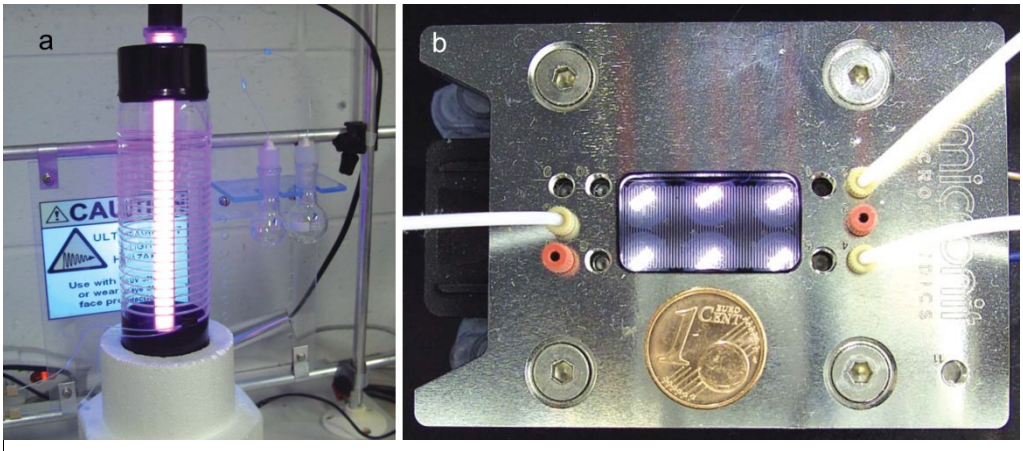

Figure 10. *Examples of photoreactors: (a) Dual microcapillary tower and (b) Micronit microchip with 6 \ 365 nm LED array. Adapted from reference [112].*

Organic compounds, photodecomposing into ketyl and α-amino radicals, are almost extensively used as photochemical initiators for nanoparticle synthesis. The efficiency of such compounds depends basically on the reduction potential of the photogenerated radical. The α-amino radical has for instance a reduction potential of -1.47 V (vs. NHE) and is therefore a stronger reductant than the ketyl radical with the reduction potential of -0.578 V (vs. NHE) [113]. It is obvious that with organic materials being applied as photoactive compounds, the use of organic solvents is also unavoidable.

Even though organic synthesis is rather expensive and environmentally unfriendly route to the formation of nanoparticles, only scarce studies are focusing on inorganic photochemistry, especially in the case of semiconducting nanomaterials. In the past decade, radiation technique has been employed to prepare nanoscale powder crystalline zinc oxide with high chemical purity from aqueous solutions, using high energy gamma or accelerated electrons irradiation [114, 115]. Direct preparation of zinc oxide from aqueous solutions containing zinc nitrate and propan-2-ol, or zinc formate and hydrogen peroxide at ambient temperature using lower energy UV radiation was reported by Gbur *et al*. [116].

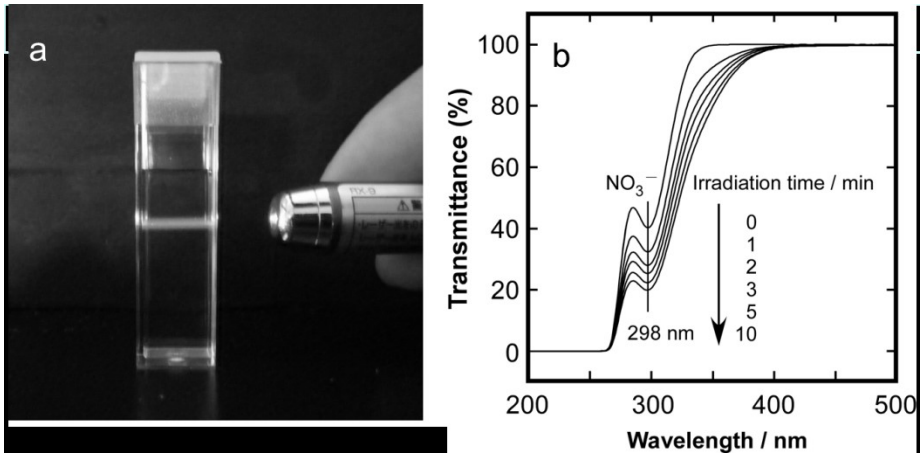

Figure 11. *(a) Photograph of 10 mM $Ce(NO_3)_3$ solution under UV light irradiation for 2 h, and (b) UV/VIS transmittance spectra of aqueous 10 mM $Ce(NO_3)_3$ solution during photochemical reaction. Adapted from reference [117].*

Photochemical technique for preparation of ceria nanocrystals in a simple aqueous solution with no additives nor heating required was reported by Kamada *et al.* [117]. The image of the irradiated cerium nitrate solution is shown in *Figure 11* a, while *Figure 11* b presents UV-VIS transmittance spectra of the irradiated solution. Formation of CeO_2 NPs could not be negligible as the absorption peak typical for ceria appears below 400 nm. The authors suggested that the irradiation of $Ce(NO_3)_3$ solution with UV light caused photochemical reduction of NO_3^- to form NO_2^-, accompanied by hydroxyl radicals (·OH) as an intermediate species. The latter were believed to oxidize Ce^{3+} to Ce^{4+} forming $Ce(OH)_2^{2+}$, which was then transformed into CeO_2 via dehydration of intermediate $Ce(OH)_4$. Although it is difficult to imagine more environmentally benign green process, the proposed mechanism for ceria NPs formation can be characterized by an extremely low production yield, implying thus that the relevance of an appropriate photoactive compound for a photochemical synthesis could not be neglected.

A unique inorganic synthesis pathway is suggested in the present study. It is known that unstable inorganic azides can be excited when heated or irradiated by radiation producing positive holes, and conduction band electrons, followed by formation of N_2 (an exothermic step). Generation of electrons after being exposed to light was seen as a feature that could lead to potential applications in photochemical synthesis. Explosive character of some azides is not to be forgotten, however. During the exothermic reaction of N_2 formation, depending on the azide used, particular amount of heat is liberated. This could lead to the explosion in the case of less stable, thus easier excitable compounds ($Pb(N_3)_2$, AgN_3, CuN_3), the explosive character increasing with the increasing ionization potential of the metal forming azide [118]. Regarding this, sodium azide (NaN_3) was seen as a promising candidate for a light induced synthesis of nanomaterials. NaN_3 is not explosive except when heated near its decomposition temperature (300 °C) or reacted with metals [119]. The latter fact brings also the main limitation to the entire synthesis process: the proposed synthesis route is not applicable for the preparation of metal

nanoparticles, such as silver or copper. Moreover, contact between the reaction solution containing azide and either of those metals with high ionization potential is to be completely avoided. Despite the aforesaid safety issues, some important advantages are provided by this photoactive compound: high solubility in water and harmless, environmentally friendly side products (N_2 gas and Na^+ ions).

4.2. Photochemical synthesis of metal nanoparticles

Any molecule that can reduce the metal precursor into the zero valent state could be applied as the reducing agent in metal nanoparticle synthesis. Aminoboranes, borohydrides, ascorbic and citric acids, alcohols, polyols, sugars or hydrogen peroxide are the most generally used reducing agents in a chemical synthesis [93], playing an essential role in the formation and growth of the nanoparticles in a typical process. Anyway, energy input may also be required as an external stimulus to induce the redox process by activating molecules in the mixture to act as a reducing agent. Take the citrate-assisted formation of gold colloids for example, the transformation of citrate ions into dicarboxyacetone is induced by heating. Not only are the stabilizing molecules used for their primary purpose, but also they serve as the reducing agent that undergoes oxidation to produce the metal nanoparticles in this case. Similar pathways are common in many synthetic strategies with light or other electromagnetic radiation being often quite suitable stimuli to induce chemical changes in the system, required for the particle formation.

Similarly to the photochemical synthesis of semiconductor nanoparticles, organic compounds are the most commonly used sensitizers in the case of metal NPs synthesis. Scheme for Au nanorods synthesis using ketyl radicals is presented in *Figure 12*. Following the UV irradiation, ketyl radicals are forming that subsequently initiate reactions to form NRs in the dark. Under applied synthesis conditions, ketyl radicals probably functioned as reducing agents for the reactions of $AuBr_2^-$ to Au^0. Au^0 atoms would serve as the nuclei

for the anisotropic growth of gold nanocrystals with the aid of hexadecyltrimethylammonium bromide (CTAB), AgBr clusters, and $AuBr_2^-$. It should be noted that the growth reactions proceeded in the dark as reported by Nishioka *et al.* [120].

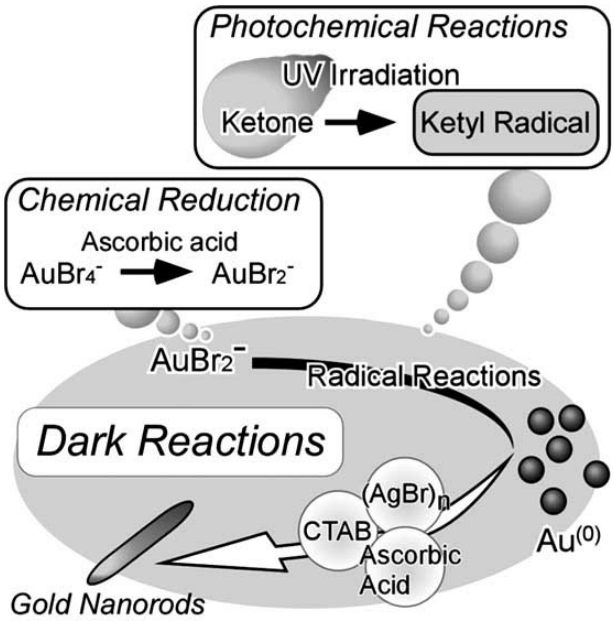

Figure 12. *Schematic illustration for the photochemical synthesis of anisotropic Au nanoparticles in micellar solution. Reprinted from reference [120].*

Radiation of different wavelength can be employed for the synthesis of nanostructures. In this thesis, however, we will only focus on UV-induced photochemical processes. It is widely reported that direct formation of nanoparticles from transition metal complexes is likely to occur upon UV illumination due to the weak photostability of the latter compounds. As far back as late 80s, such photochemical synthesis of Au and Ag nanoparticles from $MeCl_4$ complexes was reported by Yonezawa *et al*. During the irradiation of the Au precursor solution with 253.7 nm light, photolysis of the complex occurred and atomic Au^0 was produced, coagulating subsequently into a colloidal gold [121]. Silver NPs could also be formed with nothing more but a silver complex being added to the reaction solution. Excited Ag^+ from $AgClO_4$

can oxidize H_2O in this case, which results then in the formation of silver atoms followed by agglomeration to produce colloidal silver [121].

Larger control over the size and shape of the nanoparticles could be provided by the addition of ligand molecules, such as polymers [122]. The presence of polyvinylpyrrolidone, for instance, is reported to affect the diameter of the final nanoparticles as well as the rate of metal photoreduction. Decreased particle size was observed by Huang *et al*. when the higher amount of PVP was used, the latter condition was responsible for the increased rate of the photochemical process as well. It was assumed that PVP could be directly involved in the photochemical process as it contains carbonyl groups that absorb UV light and the excited species were expected to reduce Ag^+ to Ag^0 [123].

However, interaction between metal nanoparticles and polymers is not the most desirable effect, especially when the particles obtained are expected to find applications in catalysis/photocatalysis. Organic stabilizers, employed in the colloidal synthesis, would be able to block a number of active sites of catalytic materials due to the strong interaction with the metal surface and to the sterical hinders, thus leading to the loss of catalytic activity to a great extent [81, 124, 125]. In addition, organic ligands are expected to exhibit susceptibility to chemical oxidation on the surface they protect, and exposure to UV radiation should accelerate this process [126, 127]. Conversely, the opposite effect could be provided by semiconductor nanomaterials: semiconductor-metal nanoheterostructures are reported to demonstrate improved catalytic/photocatalytic properties with regard to the metal nanoparticles or semiconductor nanoparticles only [25, 107, 128, 129].

There are several approaches for the preparation of plasmonic NPs, supported on the semiconductor nanostructures. One of the most popular routes would be a two-step method that involves the initial synthesis of noble metal nanoparticles, which are further combined to a suitable support [130, 131]. Co-impregnation and co-precipitation are probably the second most commonly applied techniques for the preparation of supported nanoparticles [132].

However, aggregation and a difficult size control of the noble metal particles are the main problems attributed to these methods.

The use of semiconductor nanoparticles provides the possibility to apply completely different route to the formation of noble metal NPs. It was observed by many researchers that irradiating semiconductor nanoparticles (TiO_2, ZnO, CdS, etc.) in the presence of metal (Ag, Au, Cu, Pb or Cd) ions can result in reduction of the metal cations and that this process is accompanied by formation of nanosized metal-semiconductor structures [107, 133-136]. Take the photocatalytic approach to the synthesis of Ag-TiO_2 nanocomposites suggested by Cozzoli *et al*. for example, TiO_2 nanorods are acting both as the reducing agent and stabilizers in this case. A suggested mechanism for the colloidal stabilization of silver nanoparticles regards TiO_2 nanorods as inorganic stabilizers, acting in the same manner as conventional surfactant molecules (*Figure 13*, (1)-3)). Ag nanoparticles of different size-morphology can be obtained depending on the irradiation time, due to light-induced photo fragmentation and ripening processes [134].

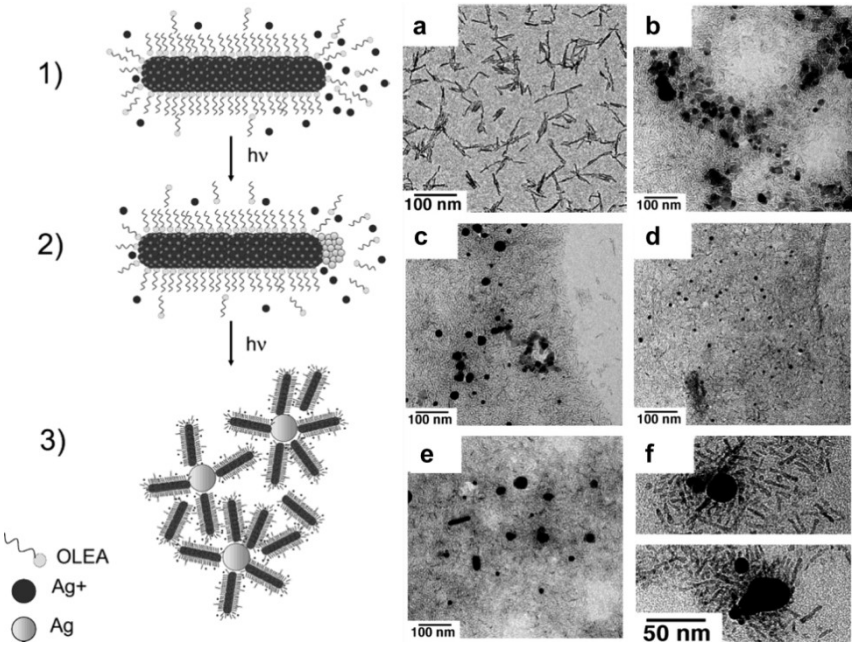

Figure 13. *Mechanism for the colloidal stabilization of Ag nanoparticles by means of TiO_2 nanorods (1)-3)) and TEM overview of (a) OLEA-capped TiO_2 nanorods; (b-e) photocatalytically prepared Ag-TiO_2 nanorod nanocomposites extracted from the same reaction batch at different irradiation times. Adapted from reference [134].*

Light-assisted synthesis, if comparing to standard chemical approaches, (i.e. precipitation or solvothermal methods), provides advantages of a uniform distribution of the reducing agent in the entire solution, rather mild reaction conditions, and high reproducibility [93]. Whereas organic solvents or photoactive compounds are usually essential components of photochemical synthesis [137, 138], the use of inorganic semiconducting nanostructures as photoactive compounds provides a possibility to carry out the process in aqueous solution. This is a huge advantage considering that organic compounds, employed in colloidal synthesis, would be able to block a number of active sites of catalytic materials due to the strong interaction with the metal surface and to the sterical hinders, thus leading to the loss of catalytic activity to a great extent.

Ceria is known for its structural stability up to 650 ºC, the ability to absorb UV radiation, and, most interesting, the oxygen storage activity [18-20]. Because of the latter property, CeO_2 modifies the catalytic performance of the elements in contact by either providing to or withdrawing oxygen from them [22]. This can result in improved catalytic performance of the material in contact. For instance, it was observed that Pt supported on ceria tends to form Pt–O–Ce bond in the interface region between Pt particles and ceria. The existence of oxidized Pt is assumed to accelerate methanol decomposition by withdrawing the electron from the methoxy group to Pt and thus weakening the C–H bond [139]. Different behavior of ceria was reported in the silver-ceria system. It is found that ceria accelerates desorption of the lattice oxygen of Ag_2O, facilitating silver conversion to metallic state. Such Ag-CeO_2 catalyst demonstrated high catalytic activity in the process of carbon monoxide oxidation [22].

Despite demonstrating these unique and outstanding properties, ceria nanoparticles have not been extensively studied by the means of supported metal nanoparticles photochemical synthesis yet. Neither is CeO_2 as frequently applied for photocatalysis as other wide band gap semiconductors, such as TiO_2 and ZnO, although being reported to be less toxic than the latter

compounds [14, 17]. A photochemical approach to the formation of supported silver catalysts on ceria was briefly presented by Scirè *et al*., albeit more stress was put on the Ag-TiO_2 system in the latter study. Moreover, both TiO_2 and CeO_2 were only studied as metal NPs supports, not taking into consideration their reductive properties under UV light [130].

The second part of our work focuses thus on preparation of Ag-CeO_2 nanoheterostructures *via* photochemical inorganic synthesis, where previously photochemically synthesized ceria nanoparticles are applied both as a photoactive compound, and as a support for silver nanoparticles. Even though the very concept of a wide band-gap semiconductor mediated synthesis is not completely novel, it has not been performed with ceria yet as far as we know. The proposed photochemical approach enables the production of silver-semiconductor heterostructures without employing organic stabilizers and additives, thus resulting in formation of nanoparticles with "clean", highly reactive metal surface.

4.3. Metal/semiconductor composite photocatalysts

In most of the cases, semiconductors are utilized for photocatalysis as a photoactive material that absorbs photons to create active electrons and holes, which would subsequently initiate reduction and/or oxidation of chemical species absorbed on the semiconductor surface. The wavelength range of the light absorbed by a semiconductor is determined by the optical band gap of it, excitation is only feasible if the energy of the photons of the incident light is larger than that of the band gap of the semiconductor.

However, despite being useful for a wide range of applications such as wastewater treatment, air purification or water splitting, large scale applications of n-type semiconductors in the environmental and energy industries are still rare [140]. Two major difficulties that are limiting practical applications are the low photocatalytic efficiency and the lack of satisfactory visible-light-responsive photocatalytic materials [23, 141, 142]. The former is

mainly caused by the recombination of excited electrons and holes while large band gaps of n-type semiconductors are responsible for their limited visible light absorption. One could think that low-bandgap photocatalysts like CdS and Fe_2O_3 could be applied instead, but the short-time photoactivity of the latter compounds makes it out of the question.

One of the possible attempts to overcome the problem could be incorporation of plasmonic metal nanostructures into semiconductors [24-26, 143]. Two distinct features are characteristic for plasmonic photocatalysis: localized surface plasmon resonance and a Schottky junction, each of them is capable to benefit photocatalysis in a different way.

The concept of LSPR was already discussed in *Section 3.1*. The oscillation of the metal's free electrons brings actually more than one significant benefits to the photocatalysis. First, it can extend the absorption range to the visible light region if plasmonic materials of suitable size and shape are chosen [86], the visible light response could be then rendered to the large-bandgap photocatalysts. Second, the UV absorption of the large-bandgap materials could also be enhanced by the LSPR [25]. Lastly, an intensive local electric field is created by the LSPR, which favors the photocatalytic reactions by powering the excitation of more electrons and holes [144], heating up the surrounding environment which in turn increases the redox reaction rate and the mass transfer [145] and polarizing the nonpolar molecules for better adsorption [146].

Several plausible LSPR induced charge transfer mechanisms are reported by many authors, one of the most viable pathways being direct hot electron transfer (DET) [8, 147, 148]. According to DET, hot electrons with energies higher than the energy of Schottky barrier are transferred into the conduction band of the semiconductor during the LSPR decay processes [10, 149]. As DET depends on the Fermi level of the plasmonic metal and alignment of the band levels of the semiconductor, electrons can be transferred from the metal into the semiconductor at energies below the band gap if the electronic energy levels match [7].

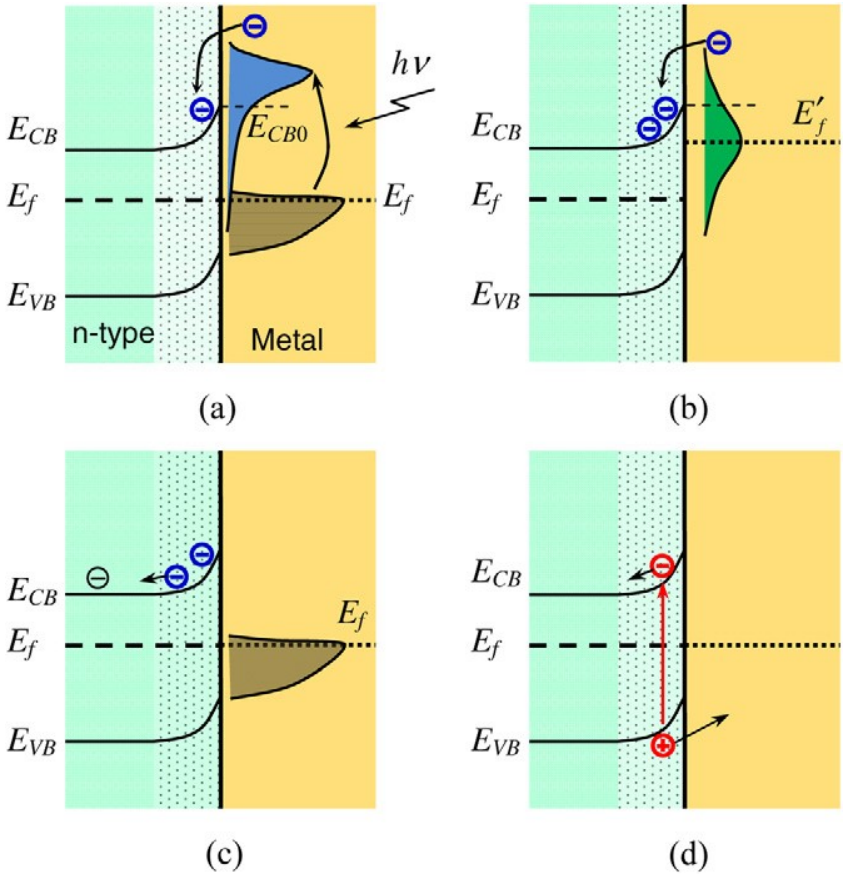

Figure 14. *LSPR induced charge transfer between metal and n-type semiconductor. (a) Excitation of the electrons to a high energy state upon absorbing the photons; (b) redistribution of electron energy forming a Fermi–Dirac distribution at a high-temperature Fermi level; (c) electrons go back to the standard distribution in the metal nanoparticle, and in the semiconductor electrons and holes are separated. (d) In the semiconductor, the electron collision excites electrons to the conduction band. Reprinted from reference [90].*

The LSPR induced scenario for n-type semiconductor is illustrated in *Figure 14*, under the assumption that there is a direct contact between the metal nanoparticle and semiconductor. The process is in principle analogous to dye sensitization, where dye molecule anchored to a semiconductor absorbs light and transfers energetic charge carriers to the semiconductor [150]. Upon resonance with incoming photons, many electrons in the metal nanoparticle gain energy higher than that of E_{CB} of the neighboring semiconductor *Figure 14* (a) and thus the direct transfer of electrons from metal to the conduction band of the semiconductor occurs. In the metal particle, electron relaxation causes redistribution of electron energy, resulting in a formation of a Fermi–

Dirac distribution at a high-temperature Fermi level as shown in Figure *14* (b). Electrons with high energy (the tail part of the electron distribution with energy $>E_f$ are still being fed) into the conduction band. Subsequently, following the full dissipation of surface plasmon energy, electrons go back to the standard distribution in the metal particle. In a meanwhile, electrons and holes flow to different regions of the semiconductor (*Figure 14* (c)) [90].

It was also demonstrated that the photocatalytic properties of semiconductor nanostructures were still enhanced after adding an insulating interlayer between the metal and the semiconductor, thus preventing the DET. It was suggested that radiative energy transfer from the metal SPR to the semiconductor can take place through near-field electromagnetic and resonant photon-scattering mechanisms [146, 151, 152].

The near-field electromagnetic mechanism is based on the interaction of the semiconductor with the SPR-induced electric fields localized around the metallic nanostructure. Photo-excited plasmonic nanostructures are characterized by strong electric fields with the highest intensity at the surface of the nanostructure which is decreasing exponentially with the increasing distance from the surface within ~20–30 nm and linearly further away. However, significant fields are present even a few nanometers away from the nanostructure, and semiconductor brought into the proximity of a photo-excited plasmonic nanostructure encounters these intense fields. As a result, the rate of electron–hole formation in some regions of the semiconductor increases by a few orders of magnitude. The SPR-induced electron–hole pair formation is the most intense in the parts of the semiconductor in a vicinity of plasmonic nanostructure, closest to the semiconductor/liquid interface (see *Figure 14* (d)). In this way, charge carriers are readily separated from each other under the influence of the surface potential. Moreover, they have a shorter distance to migrate to reach the semiconductor/liquid interface, where photocatalytic transformations can be performed. The selective generation of charge carriers close to the semiconductor/liquid interface rather than in the

bulk of the semiconductor enhances thus the probability of photoreaction relative to the probability of charge-carrier recombination [7].

In addition to the dominant role playing near-field electromagnetic mechanism, the metal SPR is accompanied by an efficient scattering of resonant photons by large plasmonic nanostructures [24]. The plasmonic nanostructure acts as a nanomirror in this case: some resonant photons that are not absorbed by the semiconductor initially could be scattered by the nanostructure, effectively giving those photons many passes through the system. This process increases the average photon path length in plasmonic nanostructures and semiconductor composites, resulting in an increased rate of electron–hole pair formation in the semiconductor [7].

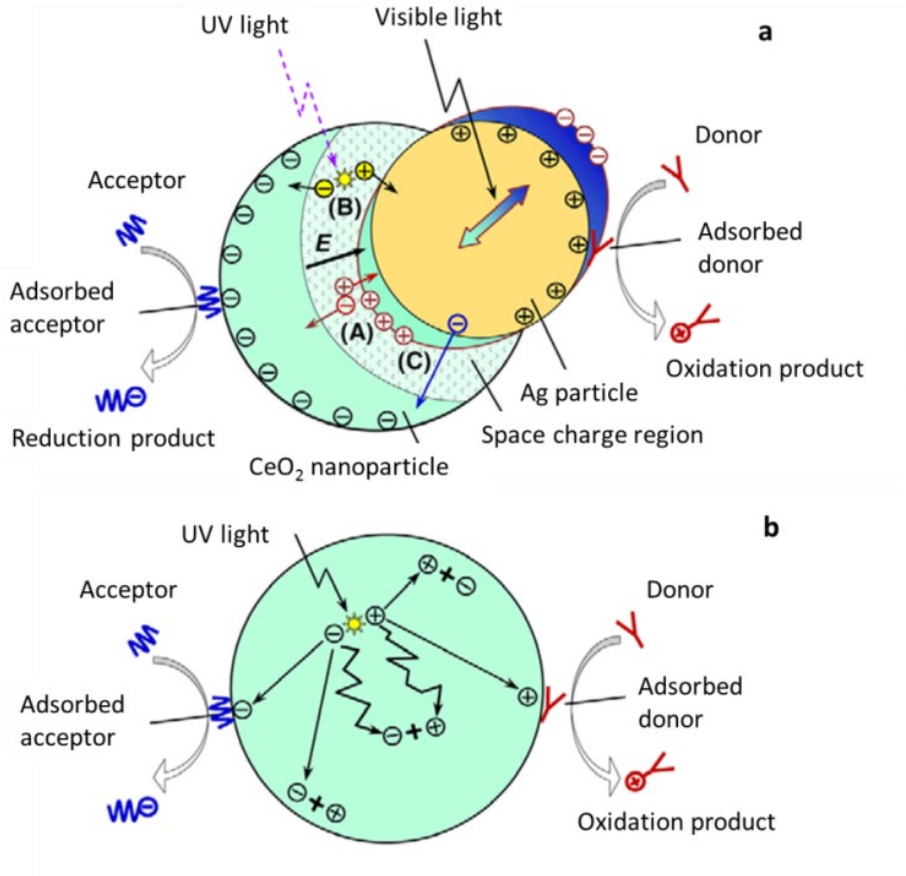

Figure 15. *Schematic representation of the major mechanisms in plasmonic photocatalysis (a) as compared to the common photocatalysis (b). The Scheme is adapted from reference [90].*

A brief look to the major photocatalysis processes is presented in *Figure 15*, where plasmonic photocatalysis (a) is compared to conventional heterogeneous photocatalysis (b). Ag-CeO_2 system is used as a model for plasmonic photocatalysts in (a) while common photocatalysts (b) are represented by CeO_2 nanoparticles. In the Ag-CeO_2 system, Ag and ceria can absorb light separately and contribute to photocatalysis synergetically. Upon the absorption of visible light by Ag NPs, collective oscillation of the electrons arising due to LSPR excites electrons and holes in the semiconductor. In addition, if there is a direct contact between metal and semiconductor and if the LSPR excited electrons in Ag have sufficient energy to overcome the space-charge region, they are fed directly into the conduction band of CeO_2. Moreover, charge separation is improved if compared to the conventional photocatalysis where electrons and holes, excited in the volume of the semiconducting nanoparticle, migrate to the surface by diffusion and thus have plenty of chances to recombine. In the case of plasmonic photocatalysis, the Schottky junction is created after the contact between noble metal and semiconductor is established. [153]. Electrons tend to move from ceria side to Ag creating a positively charged region. The built-up internal electrical field (indicated by E in *Figure 15* (a)) prevents further movement of the carriers in the equilibrium state. If the exciton is generated in or near the space-charge region (depicted as (B) in *Figure 15* (a)), the electron is forced to move to the silver side while the hole tends to move to CeO_2 side. As a result, recombination of charge carriers is prevented, separated electrons and holes can be then captured by the acceptors and donors in the solution and initiate further redox reactions [153].

Chapter 5. Experimental Section

5.1. Materials

In this study, cerium(III) chloride heptahydrate, $CeCl_3 \cdot 7H_2O$ (99.9%; Acros Organics) and cerium(III) nitrate hexahydrate, $Ce(NO_3)_3 \cdot 6H_2O$ (99.99%; Sigma-Aldrich) were used as starting materials for CeO_2 NPs synthesis. Synthesis of ceria nanoparticles was carried out without using any surfactant or by using polyvinylpyrrolidone (M.W. 8000, Acros Organics) as a molecule capping agent. Sodium azide (NaN_3, 99.95%)* was obtained from Sigma-Aldrich. Sodium hydroxide NaOH (99.8%) for control samples was obtained from Reachem Slovakia.

For the synthesis of Ag-CeO_2 nanoheterostructures, silver nitrate ($AgNO_3$, 99%, Sigma-Aldrich) was applied as a silver precursor while ethanol (LiChrosolv, Sigma-Aldrich) was used as a radical scavenger.

Samples were prepared for ICP-OES analysis by dissolving them in the mixture of sulfuric acid (H_2SO_4, 96%) and hydrogen peroxide (H_2O_2, 35% Chempur).

The photocatalytic activity of the synthesized nanostructures was checked on decomposition of tributyltin chloride (TBT) (96% Sigma-Aldrich). For GC-MS analysis, samples were prepared by derivatization and dispersive liquid-liquid microextraction procedure. Sodium tetraethylborate ($NaBEt_4$ 97% Sigma-Aldrich) was used as derivatization agent, methanol (99.9% Sigma-Aldrich) as a disperser solvent and 40 μL of carbon tetrachloride (CCl_4 99.5% Sigma-Aldrich) as an extraction solvent.

*CAUTION. Although sodium azide is a valuable substance in photochemical synthesis, it is nonetheless a toxic, reactive and energetic material and appropriate safety precautions should be taken into consideration. Care should be taken whenever working with metal azides which are often thermally unstable and shock sensitive. Reactions should be performed on small scales in high-pressure vessels with safety release valves. Proper

protection and extreme caution should be used when working with undecomposed metal azide intermediates. Solid metal azides may detonate upon rapid heating or vigorous grinding and potentially by friction from spatula scraping.

5.2. Photochemical Two-Step Synthesis

Synthesis of both ceria nanoparticles and CeO_2-Ag nanoheterostructures were performed using a 40 W low pressure mercury discharge lamp NIQ 40/18 – 45000024 (Heraeus – Amersil, Germany), emitting a spectrum with lines at 185, 254, 313, 365, 405, 436, 546 and 579 nm. The photocatalytic reactor is shown in *Figure 16* and *Figure 17*. Also, color changes of the reaction solution over irradiation time might be observed in the aforesaid Figures.

5.3. Preparation of the CeO_2 nanostructures

Cerium chloride or cerium nitrate have been applied as cerium precursors in this work. Synthesis of ceria nanoparticles was carried out without using any surfactant or by using polyvinylpyrrolidone (PVP). In the case of polymer-free synthesis, 2.70 g (7.3 mmol) of $CeCl_3 \cdot 7H_2O$ or 3.13 g (7.2 mmol) of $Ce(NO_3)_3 \cdot 6H_2O$ was dissolved in 50 mL of deionized (DI) water. After stirring the solution for 10 minutes, 0.47 g (7.2 mmol) of sodium azide NaN_3 was added to the solution, which was then diluted up to 250 mL. Subsequently, the homogeneous solution was transferred into a 250 mL volume home-made glass reactor and stirred vigorously for 30 minutes before the irradiation has started. The nitrogen gas was flushed through the solution before and during the irradiation.

For the surfactant-assisted synthesis, 2 – 10 g PVP was dissolved in deionized water under vigorous stirring before adding the cerium source and sodium azide to the solution. The later steps remain unchanged.

The chosen photoactive compound can be excited by radiation, shorter than 270 nm (see *Figure 18*). Therefore, a 40 W low pressure mercury

discharge lamp NIQ 40/18, emitting lines at 185, 254 nm was used. The lamp embedded in a quartz tube was immersed into the solution filled into a glass reactor equipped with a thermometer. The irradiation period was varied from 30 to 300 min. The temperature of the reaction solution was raising with the increasing irradiation time: it was 20 ± 2 ºC before the reaction and varied between 40 and 70 ± 5 ºC after the reaction was over, the latter parameter depending on the exposure to UV time.

The pH value of the initial solution was 6.6 ± 0.08 and it showed a trend to decrease with the increasing irradiation time, thus, the solution becoming more acidic: after irradiating the solution for 30 min, the pH value was 6.21 ± 0.05, and it reached 5.90 ± 0.06 after 90 min of irradiation.

After the irradiation was terminated, the finely dispersed solid phase was separated via centrifugation for 60 min at 7000 rpm (Eppendorf 5804), particles were washed with deionized water twice and dried at 60 °C overnight. Some of the as-prepared samples were further annealed in air at different temperatures between 100 and 900 °C for 5 h using a chamber furnace.

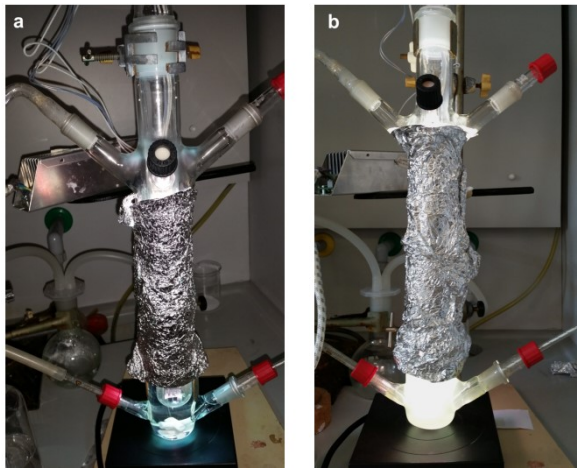

Figure 16. *Synthesis of CeO_2 nanoparticles in aqueous solution under UV irradiation: (a) – 0 min, (b) – 30 min.*

5.3.1. Control samples

In order to check the relevance of sodium azide in the photochemical synthesis, three experiments were carried out.

A. As it was reported by Kamada *et al*. [117] that irradiation of pure aqueous $Ce(NO_3)_3$ solutions results in formation of ceria nanoparticles, irradiation of the aqueous solution of $Ce(NO_3)_3$ without any additives was carried out in our study as well. The procedure was kept identical to the previously reported except for the composition of the solution.

B. The impact of polymer was investigated by introducing PVP to the pure aqueous solution of $Ce(NO_3)_3$ and further irradiating the solution as reported before.

C. Reaction with NaOH was carried out in order to check the significance of the photochemical synthesis and to better understand the mechanism of nanoparticle formation under UV irradiation. Therefore, 3.13 g of $Ce(NO_3)_3 \cdot 6H_2O$ (7.2 mmol) was dissolved in 200 mL deionized water and stirred vigorously under the constant stream of nitrogen gas for 30 minutes. Subsequently, 0.1 M NaOH solution was added dropwise to the reactor until the pH value of about 8.5 was reached and the dispersed solid phase was formed which was later washed and centrifuged in order to separate it from the solution.

Also, an attempt was made to prove that the photochemical process rather than the radiation induced heating of the solution is responsible for formation of the nanostructures. To this end, aqueous solution of CeO_2 precursor and sodium azide was poured into a glass reactor, stirred vigorously and smoothly heated up to 70 ºC.

5.3.2. Optimized synthesis procedure for further modification with silver NPs

1.5 g of $Ce(NO_3)_3 \cdot 6H_2O$ (3.5 mmol) was dissolved in 50 mL of deionized water. After stirring the solution for 10 minutes, 0.23 g of sodium azide (3.6 mmol) was added to the solution, which was then diluted up to 250 mL. Subsequently, the homogeneous solution was transferred into a 250 mL volume home-made glass reactor and stirred in the dark vigorously for 30

minutes before the irradiation has started. The nitrogen gas was flushed through the solution at this stage as well as during the reaction. After irradiating the reaction mixture for 300 min, the finely dispersed solid phase was centrifuged for 60 min at 7000 rpm (Eppendorf 5804), the particles obtained were washed with deionized water twice and dried at 60 °C overnight.

5.3.3. Neutralization of the remaining sodium azide in the supernatant

Even though the amount of sodium azide used in the reaction is rather small and should be completely decomposed while irradiating the solution, even a small amount of sodium azide must never be flushed down the drain as it could cause serious accidents if the azide reacts with lead or copper in the drain lines to produce an explosive compound. Moreover, NaN_3 is known to be acutely toxic to aquatic life with long lasting effects. Therefore, to make sure that no sodium azide would reach the environment, the below described procedure for decomposition of azide by oxidizing it with HNO_2 was carried out after every synthesis as suggested by Betterton [154]. An aqueous supernatant (decanted from the synthesized nanoparticles after centrifugation) containing no more than 5% sodium azide was put into a three-necked flask equipped with a stirrer and a dropping funnel. Approximately 7 mL of 20% aqueous solution of sodium nitrite per gram of sodium azide was added with stirring. A 20% aqueous solution of sulfuric acid was then added gradually until the reaction mixture is acidic to litmus paper. The order of addition is essential. Poisonous, volatile hydrazoic acid (HN_3) will evolve if the acid is added before the nitrite. When the evolution of nitrogen oxides ceases, the acidic solution was tested with starch iodide paper. The neutralization procedure is over when the starch iodide paper turns blue, thus indicating that the excess nitrite is present, and the decomposition is complete.

5.4. Preparation of the CeO_2-Ag nanoheterostructures

5.4.1. Control samples

Control samples were prepared by irradiating aqueous and ethanol containing (20% v/v) solutions of $AgNO_3$. Concentration of silver salt was the same as in the ceria-mediated synthesis. Control samples without irradiation of the solutions were also prepared: A – by stirring the solution in the dark and B – by heating the solution up to 80 °C. However, no evidence of silver nanoparticle formation was observed in neither of the two cases.

5.4.2. Pure aqueous solution

CeO_2 nanoparticles, synthesized according to the procedure described in section 5.3.3, were further dispersed in an aqueous solution of $AgNO_3$, which was then diluted up to 250 mL and sonicated for 15 min. The final solution contained 4.8 mmol/L ceria nanoparticles and 0.0039 – 3.5 mmol/L $AgNO_3$. After continuously stirring the dispersion for 30 minutes in the dark under the steady stream of nitrogen, the exposure to UV light was initiated. Irradiation time varied from 30 to 150 min, nitrogen gas was flushed through the reactor constantly. Details of the synthesis conditions are presented in Table 1.

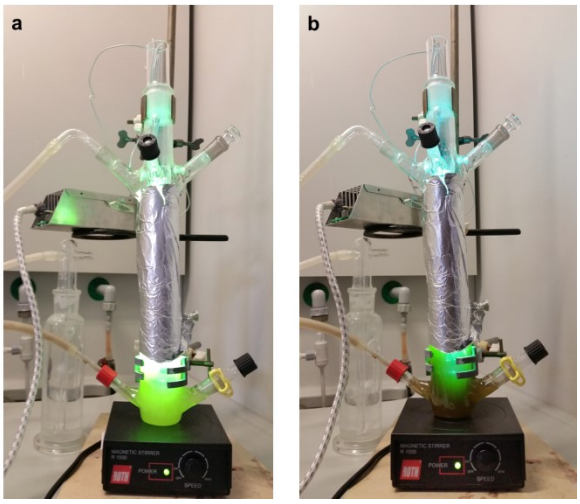

Figure 17. *Synthesis of Ag-CeO_2 nanoheterostructures in aqueous solution under UV irradiation: (a) – W35020, (b) – W35150.*

5.4.3. Ethanol containing solution

Silver nitrate was dissolved in around 50 mL of deionized water and stirred for 10 min before CeO_2 nanoparticles were introduced to the system. The colloidal solution was then diluted up to 180 mL with DI water. Finally, 80 ml of ethanol was added and the solution was sonicated for 15 min. The final solution contained 4.8 mmol/L ceria nanoparticles and 0.0035 – 0.1 mmol/L $AgNO_3$. Identically to the previously presented procedure, the as-prepared dispersion was continuously stirred for 30 minutes in the dark under the steady stream of nitrogen. Irradiation time varied from 30 to 150 min, nitrogen gas was flushed through the reactor constantly. Details of the synthesis conditions are presented in Table 1.

Table 1. Synthesis conditions of the Ag-CeO_2 samples.

Sample	$AgNO_3$ concentration (mmol/L)	Solvent	Irradiation time (min)
W20010	2.0	H_2O	10
W20030	2.0	H_2O	30
W20090	2.0	H_2O	90
W20150	2.0	H_2O	150
W26030	2.6	H_2O	30
W26090	2.6	H_2O	90
W26150	2.6	H_2O	150
W35010	3.5	H_2O	10
W35020	3.5	H_2O	20
W35030	3.5	H_2O	30
W35060	3.5	H_2O	60
W35090	3.5	H_2O	90
W35120	3.5	H_2O	120
W35150	3.5	H_2O	150
E0035002	0.035	20% v/v C_2H_5OH in H_2O	2
E0035005	0.035	20% v/v C_2H_5OH in H_2O	5
E0035020	0.035	20% v/v C_2H_5OH in H_2O	20
E0035030	0.035	20% v/v C_2H_5OH in H_2O	30
E0035150	0.035	20% v/v C_2H_5OH in H_2O	150
E15030	1.5	20% v/v C_2H_5OH in H_2O	30

5.5. Characterization of the products obtained

Absorption of the nanocomposites suspensions was investigated using a 100 UV−VIS Lambda 35 (Perkin Elmer) spectrophotometer, with a 1 cm path length quartz cell. The UV−VIS absorption spectra were collected over a wavelength range of 250−700 nm right after the synthesis. Suitable blanks and controls were measured as well.

During the XRD data collection, 2θ was changed from 10° to 80° (step width 0.02° and integration time 0.5 s). The measurement was carried out using Ni-filtered Cu Kα radiation on a Rigaku MiniFlex II diffractometer working in Bragg–Brentano (θ /2θ) focusing geometry.

Raman spectra were recorded with a WITec Confocal Raman Microscope (WITec alpha300 R, Ulm, Germany), using a frequency doubled YAG:Nd laser (532 nm) for sample excitation.

EDX analysis was performed with Hitachi TM-3000 containing a silicon drift detector and energy resolution of 154 eV (Cu-Kα). Accelerating voltage was set to 15 kV.

For ICP-OES analysis, Ag-CeO_2 samples were prepared according to the following procedure: 5 mL of HNO_3 was poured onto 0.02 g of each sample, the color of the nanoparticles was thus changing from dark brown to yellow as a result of dissolved silver. Subsequently, 2 mL H_2O_2 was added in order to reduce Ce^{4+} to Ce^{3+}, solid particles turned orange which implies formation of the trivalent cerium. Shortly after this, all the precipitate has dissolved forming a transparent solution which was then heated in order to get rid of the peroxide remaining as well as to reduce volume of the acid. Finally, the solution was diluted to appropriate volume with deionized water. Perkin Elmer Optima 7000 DV 7000 DV ICP-OES system was used for the determination of silver and cerium content in the as-prepared samples.

XPS measurements are carried out in order to obtain information about the elemental chemical states and surface composition of Ag-CeO_2 samples on the upgraded Vacuum Generator (VG) ESCALAB MKII spectrometer fitted

with a new XR4 twin anode. The non-monochromatised Mg Kα X-ray source was operated at hν = 1253.6 eV with 300 W power (20 mA/15 kV) and the pressure in the analysis chamber was lower than $5 \cdot 10^{-7}$ Pa during the spectral acquisition. The spectra were acquired with an electron analyzer pass energy of 20 eV for narrow scans and resolution of 0.05 eV and with a pass energy of 100 eV for survey spectra. All spectra were recorded at a 90° take-off angle and calibrated from the hydrocarbon contamination using the C1s peak at 284.6 eV. The spectra calibration, processing and fitting routines were performed using Avantage software (version 5.962) provided by Thermo VG Scientific. Core level peaks of Ce3d, Ag3d and O1s were analyzed using a nonlinear Shirley-type background and the calculation of the elemental composition was performed on the basis of Scofield's relative sensitivity factors.

The morphology of nanoheterostructures was observed by transmission electron microscopy (JEOL JEM-2100F), equipped with a Schottky-type field emission gun and a Gatan Ultrascan 1000 camera. The microscope was operated at 200 kV and ambient temperature. The TEM specimens were prepared by diluting fresh samples of the reaction solution with water and sonicating for 5 min. Afterwards, a drop of the dilute suspension was placed on a carbon-coated copper grid and allowed to dry by evaporation at ambient temperature. The bright field (BF-) and high angle annular dark field scanning transmission electron microscopy (HAADF-STEM) images were recorded simultaneously using a JEOL ADF ring detector and a Gatan BF detector with a camera length of 8 cm. Gatan Digital Micrograph software was used for both recording and processing of all TEM images.

The chromatographic analysis was performed on a Perkin Elmer Clarus 580 series gas chromatograph coupled to a Perkin Elmer Clarus 560 S mass spectrometer (Perkin Elmer, Shelton, USA). The GC system was equipped with Elite-5MS capillary column (30 m × 0.25 mm id, 0.25 μm film thickness) coated with methylpolysiloxane (5% phenyl). Helium was employed as a carrier gas with a constant flow of 1 mL min^{-1}. The injector temperature was

held at 250 °C. Injection was performed in pulsed splitless mode (pulsed to 4 mL min^{-1} until 1.5 min, split (50:1) open at 1.55 min). The oven temperature was programmed as follows: 80 °C for 3 min, from 80 to 210 °C at 25 °C min^{-1}, from 210 to 250 °C at 40 °C min^{-1} and held at 250 °C for 3 min. The capillary column was connected to the ion source of the mass spectrometer by means of the transfer line maintained at 280 °C**.** The electron ionization ion source conditions were: electron energy 70 eV and temperature 180 °C. GC-MS in full scan mode was used for the optimization of the dispersive liquid-liquid microextraction (DLLME) method. The analyses were carried out with a filament multiplier delay of 5 min. and the acquisition was performed in the range of m/z 50–500. Selected ion monitoring (SIM) mode was used for the quantitative analysis. The quantification ions (m/z values) were 235, 263 and 291.

5.6. Photocatalytic activity experiments

Photocatalytic activity of Ag-CeO_2 nanoheterostructures and ceria nanoparticles was assessed by the photo-degradation of TBT under visible light. A stock solution of 1000 mg/L Tributyltin chloride (TBT) (96% Sigma-Aldrich) was prepared in methanol, 12 mg/L working solutions in deionized water were freshly prepared from the stock solution prior to undertaking the reaction. The photocatalytic degradation was carried out in 250 mL beaker containing 200 mL working solution and 0.10 g of catalyst at room temperature (25–30 °C), using the LED lamp with the maximum at 390 nm and an output of 10 W. After adding 0.1 g of CeO_2/Ag-CeO_2 sample to the aqueous 12 mg/L TBT solution, the pollutant-photocatalyst system was further sonicated for 15 min. Subsequently, the dispersion was stirred in the darkness for 30 min in order to establish adsorption/desorption equilibrium between the pollutant and the surface of the catalyst under room air equilibrated conditions. Finally, the irradiation has started and solutions were irradiated for 30 h in total. Every 24 h, 10 ml of samples were collected, centrifuged for 60 min at

7000 rpm (Eppendorf 5804) and filtered through a Fisherbrand Syringe filters with a hydrophilic PTFE membrane (pore diameter 0.45 µm). Subsequently, samples were prepared for GC-MS analysis by derivatization and dispersive liquid-liquid microextraction procedure. 4 mL of tributyltin aqueous solution and 100 µL of 2% of derivatization reagent (sodium tetraethylborate ($NaBEt_4$ 97% Sigma-Aldrich)) were placed to a 10 mL centrifuge tube with a conic bottom. The solution was left for 10 min for derivatization of tributyltin. Then, 800 µL of the mixture containing 760 µL of methanol (99.9% Sigma-Aldrich) as a disperser solvent and 40 µL of carbon tetrachloride (CCl_4 99.5% Sigma-Aldrich) as an extraction solvent was rapidly injected to the solution using 1 mL syringe. A cloudy solution formed was centrifuged for 3 min at 5000 rpm (Boeco S-8 centrifuge). CCl_4 phase with the analyte was sedimented at the bottom of the tube. 1 µL of the extraction phase was injected into GC-MS.

Chapter 6. Photochemical synthesis of ceria nanoparticles

As mentioned in chapter 4, ceria is a unique photoactive material, which can serve both for catalytic/photocatalytic applications and as a metal nanoparticle support. Although there are many ways to produce CeO_2 nanoparticles, most of them require the use of organic solvents and capping agents, even if photochemical synthesis is applied. In this research work, CeO_2 nanoparticles have been prepared in aqueous solution via a photochemical route using sodium azide (NaN_3) as a photo-active compound. The synthesis trials were carried out without using a surfactant or by using different concentrations of polyvinylpyrrolidone (PVP) as a surface active agent. The overall process could be described as green synthesis of ceria as it employs the most widespread, environmentally friendly and biocompatible solvent, the only by-product formed being nitrogen. Main aspects of the synthesis together with a detailed analysis of the synthesis parameters impact on the particle properties are summarized in this chapter.

6.1. Mechanism of ceria nanoparticle formation using sodium azide as a photoactive material

Possible mechanisms of metal oxide formation under ionizing or UV radiation were proposed by many authors. It is suggested that the ionizing radiation induces total reduction of metal cations, followed by oxidation via reaction with oxygen present in water [114, 155]. Similar mechanism (partial or total photo-initiated reduction of metal ions under appropriate conditions followed by oxidation of metallic particles) is possible in UV irradiated system too [156].

We suggest a slightly different mechanism of CeO_2 formation, although it has not been fully revealed, yet. Inorganic photoactive material, used in the experiments, is sodium azide. It is obvious from the absorption spectra of NaN_3 (*Figure 18*a) that electromagnetic radiation with wavelength shorter than

270 nm is efficiently absorbed by this compound. Upon irradiation of crystals of inorganic azides with radiation of wavelength corresponding to a characteristic absorption band of the solid, the photochemical decomposition takes place according to equation [157].

$$2MN_3 \rightarrow 2M^+ + 3N_2 \uparrow + 2e^- \qquad \textbf{(3)}$$

The generated electrons participate in subsequent reaction, causing formation of hydroxide ions:

$$2H_2O + 2e^- \rightarrow H_2 \uparrow + 2OH^- \qquad \textbf{(4)}$$

One should also consider that oxidative (·OH) and reductive (·H) species are formed via direct V-UV photolysis of water [158, 159]. If Ce^{3+} ions are present in the solution, the following processes take place, resulting in the formation of cerium(IV) oxide:

$$Ce^{3+} + {}^{\bullet}OH \rightarrow Ce^{4+} + OH^- \qquad \textbf{(5)}$$

$$Ce^{4+} + 2OH^- \rightarrow CeO_2 \downarrow + 2H^+ \qquad \textbf{(6)}$$

It should not be forgotten that NO_3^- ion might also be a potential ·OH radical source under UV irradiation. Photolysis resulting in formation of $\cdot NO_2$ and hydroxyl radical can be described as [117]:

$$NO_3^- + H^+ + h\nu \rightarrow {}^{\bullet}NO_2 + {}^{\bullet}OH \qquad \textbf{(7)}$$

Nitrate ion absorbs light from 330 to 284 nm with the peak at around 298 nm [117]. The main spectral lines of the light source used by us are at 185 and 254 nm. However, the hydrogen amalgam lamp also emits a weak spectral line at 313 nm, which could be absorbed by the nitrate ion to a small extent.

Thus, some minor formation of ·OH radicals might originate from the photolysis of nitrate ion.

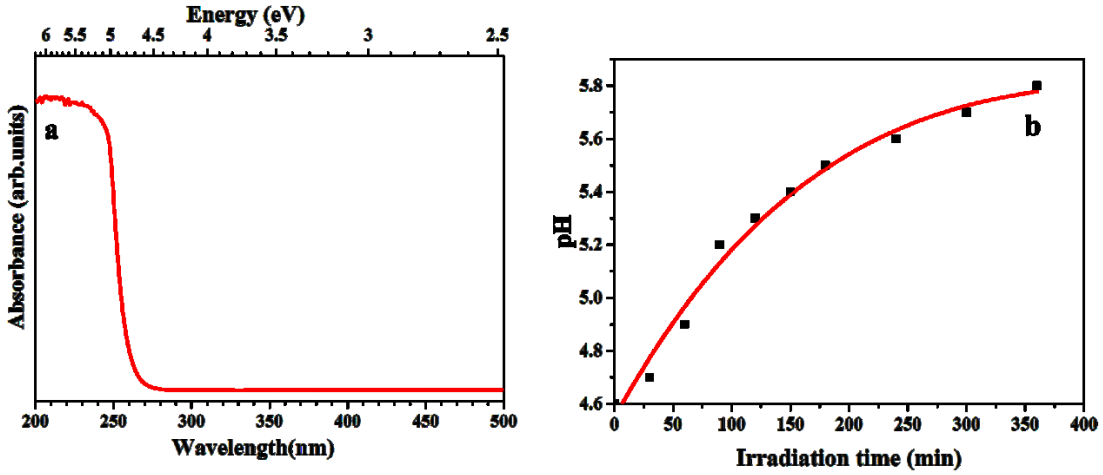

Figure 18. *Absorption spectrum of sodium azide aqueous solution at room temperature (a) and pH change of acidified sodium azide solution under UV irradiation (b).*

The proposed mechanism for CeO_2 formation is presented in *Figure 19* . In order to better understand the processes occurring in the system under UV irradiation, pH change with the increasing irradiation time of the acidified NaN_3 solution was observed. As can be derived from *Figure 18* (b), the pH is increasing slowly with increasing irradiation duration. Such a uniform and smooth production of OH^- ions in the reaction solution is expected to cause formation of small and monodisperse nanoparticles.

As azide is believed to be responsible for formation of OH^- ions, it brings significance of the photochemical synthesis into question as the use of sodium hydroxide or ammonia solutions for the synthesis of ceria nanoparticles seems to be an easier route. Following this idea, reaction with NaOH was carried out as presented in the experimental section (0.1 M NaOH was added dropwise to a cerium nitrate solution till the pH value of 8.5 was reached). The resulting solid particles were soluble in mineral acids (HNO_3, HCl) what indicates that $Ce(OH)_3$ is present in the final product as stated in Eq (7).

$$Ce^{3+} + 3OH^- \rightarrow Ce(OH)_3 \qquad \textbf{(8)}$$

In the case of photochemical synthesis with NaN_3, pH value of the initial solution was 6.6 ± 0.08 and it showed a trend to decrease with the increasing irradiation time, thus, the solution becoming more acidic: after irradiating the solution for 30 min, pH value was 6.21 ± 0.05, and it reached 5.90 ± 0.06 after 90 min of irradiation. Acidification of the solution arises due to the formation of H^+ ion as presented in Eq (6). Trying to dissolve the product obtained via photochemical synthesis with NaN_3 was not successful applying both HCl and HNO_3. Hence, this simple experiment has shown that the presence of $OH^{\cdot}$ radical, forming via direct photolysis of water, is essential for oxidation of Ce^{3+} to Ce^{4+} to occur. It is also necessary to state that, although CeO_2 nanoparticles can be obtained via precipitation method, photochemical technique gives one main advantage: a very slow and steady generation of OH^- ion (*Figure 18* (b)), which is not possible to achieve even when using the lowest addition rates in precipitation technique. Such a smooth and constant pH change should result in a formation of small monodisperse nanoparticles.

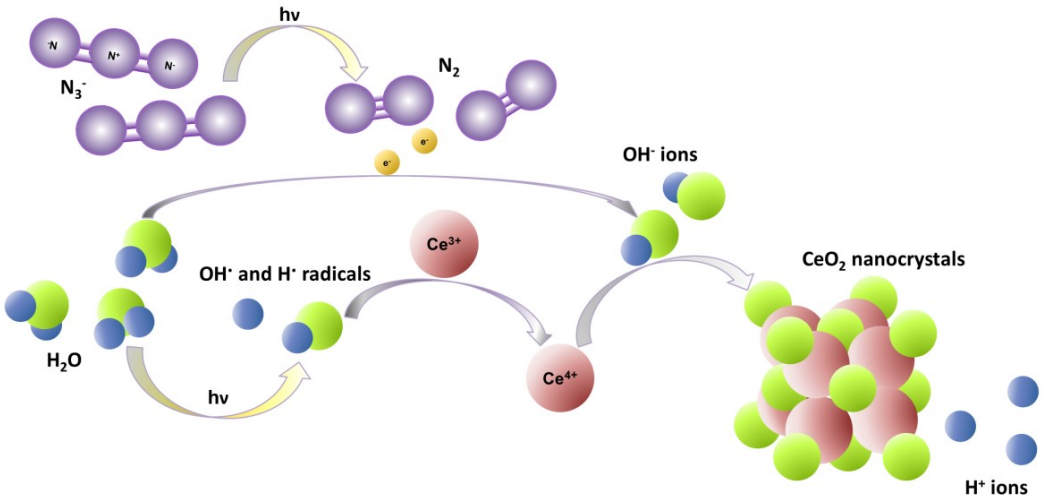

Figure 19. *Scheme of CeO_2 NPs formation under UV irradiation in the presence of sodium azide: electrons left behind after decomposition of azide reduce water to form OH^- ions, in a meanwhile photolysis of water results in the formation of hydroxyl radicals. The latter oxidise Ce^{3+} to Ce^{4+} which further reacts with hydroxide ion to form CeO_2. The minor impact of nitrate ions is not included in the Scheme.*

In order to verify whether it is really necessary to use azide for photochemical formation of CeO_2, an attempt was made to prepare CeO_2 nanoparticles by irradiating a solution containing only $Ce(NO_3)_3$ as reported by Kamada *et al* [117]. It is also important to note that polyvinylpyrrolidone is reported to act in two ways, i.e. as a molecule capping agent and as a sensitizer for photochemical processes. It was found by Giuffrida *et al* [156] that PVP was an efficient sensitizer of the copper photoreduction, although no sign of CeO_2 colloid was observed on irradiating a solution containing Ce precursor and PVP with 253.7 nm light as reported by Kapoor *et al* [160]. Therefore, the effect of PVP as a sensitizer for photochemical formation of CeO_2 nanoparticles was also checked by us. However, no signs of colloidal solution formation were observed neither while irradiating the aqueous solution of $Ce(NO_3)_3$ as suggested by Kamada *et al*. [117], nor while exposing the aqueous solution of $Ce(NO_3)_3$ or $CeCl_3$ and PVP to UV light. This leads to a conclusion that addition of sodium azide as a photoactive material is essential in the proposed photochemical synthesis of CeO_2 nanoparticles.

6.2. The phase purity and particle size determination: X-ray diffraction and Raman spectroscopy studies

The phase purity of the product obtained under various experimental conditions (introduced in the experimental section) was examined by recording and analyzing powder XRD patterns. The XRD patterns of CeO_2 samples before and after heat treatment (for 5 h, temperature ranges from 100 to 900 °C) are shown in

*Figure **20***. Broad peaks of CeO_2 nanocrystals attributed to the cubic fluorite structure ($Fm\bar{3}m$) (reference data: PDF-4+ (ICDD) 04-011-8929) are exhibited by the unheated sample, indicating that single phase CeO_2 containing nanoscale crystallites was successfully synthesized using this photochemical synthesis technique. No changes in the XRD patterns were observed depending on cerium source. The addition of PVP had no influence on phase formation

and had little impact on the particle size according to the XRD patterns. It is obvious though that increasing the annealing temperature leads to the growth of CeO_2 nanocrystallites (broadening of the CeO_2 peaks decreases with increased temperature). Moreover, the increasing crystallinity with increasing heat-treatment temperature was also observed due to increasing peak intensity in the XRD patterns.

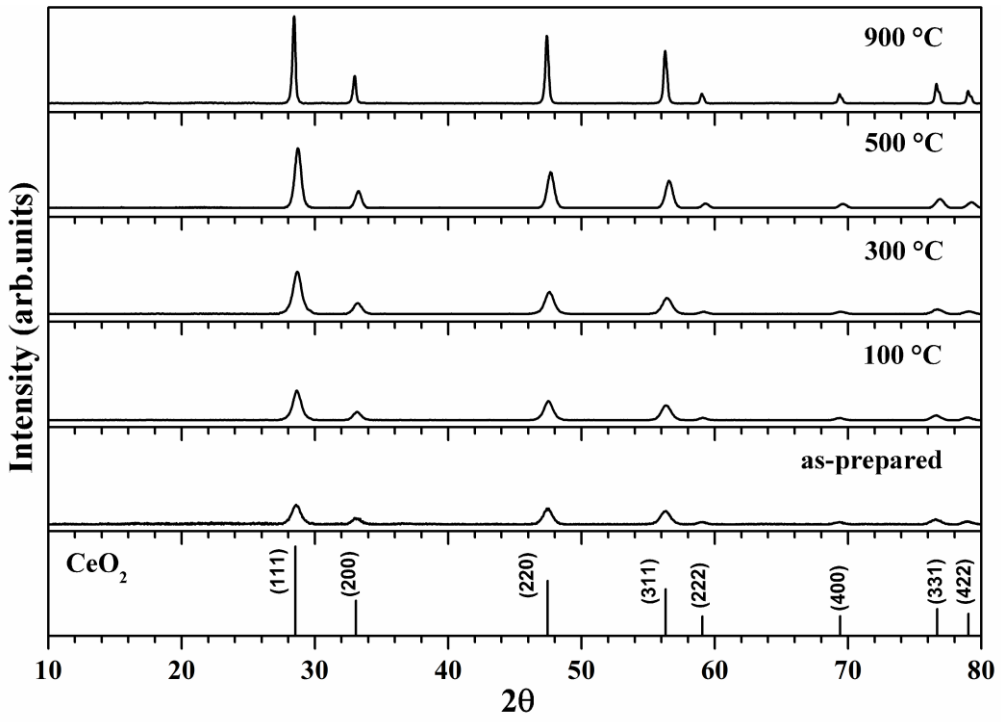

Figure 20. *XRD patterns of obtained CeO_2 nanoparticles.*

The average crystallite size was calculated for different samples from XRD peak broadening of (111) ($2\theta \approx 28.5°$) using Scherrer's equation [161]:

$$D = \frac{k\lambda}{\beta \cos\theta} \qquad \textbf{(9)}$$

Here λ is the wavelength of the X-ray radiation (λ = 0.154 nm), K is a constant taken as 0.89, θ is the diffraction angle and β is the full-width at half-maximum (FWHM) in radians.

Table 2. Crystallite size, lattice constant *a* according to XRD and Raman line broadening and band gap from absorption data.

Synthesis	Crystallite size, nm		Lattice parameter *a*, nm	Band gap, eV
	From XRD line broadening	From Raman line broadening (eq.10)		
irrad. for 30 min	6.6 ± 0.45	7.0 ± 0.3	0.5439 ± 0.0004	3.56
irrad. for 60 min	8.0 ± 0.2	8.3 ± 0.2	0.5433 ± 0.0004	3.52
irrad. for 90 min	8.95 ± 0.2	9.2 ± 0.3	0.5417 ± 0.0007	3.51
lower precursor conc., irrad. for 300 min	13.9 ± 0.9	14.2 ± 0.8	0.5388 ± 0.0005	3.49
1 mmol/L PVP, irrad. for 90 min	5.9 ± 0.1	6.7 ± 0.3	0.5432 ± 0.0007	3.45
2.5 mmol/L PVP, irrad. for 90 min	5.5 ± 0.3	6.1 ± 0.7	0.5439 ± 0.0009	3.49
5 mmol/L PVP, irrad. for 90 min	3.9 ± 0.6	4.1 ± 0.8	0.5487 ± 0.0035	3.57
irrad. for 90 min, calc. at 100 ºC for 5 h	10.3 ± 0.7	12.5 ± 0.3	0.5405 ± 0.0008	3.51
irrad. for 90 min,calc. at 300 ºC for 5 h	10.9 ± 0.3	13.6 ± 0.7	0.5395 ± 0.0009	3.50
irrad. for 90 min, calc. at 500 ºC for 5 h	14.3 ± 1.1	14.8 ± 0.5	0.5385 ± 0.0006	3.49
irrad. for 90 min, calc. at 700 ºC for 5 h	27.4 ± 2.2	16.8 ± 0.4	0.5368 ± 0.0009	3.31
irrad. for 90 min, calc. at 900 ºC for 5 h	53.8 ± 4.8	29.9 ± 2.1	0.5418 ± 0.0003	2.90

The calculated average crystallite sizes for the unheated samples prepared without any surfactant were slightly radiation exposure dependent (the shorter irradiation time, the smaller particles were formed) and varied from 6.5 to

9.0 nm (Table 2) when the irradiation time was prolonged from 30 to 90 min. Increasing irradiation time up to 300 min resulted in formation of remarkably larger particles (13.9 ± 0.9 nm) and a higher yield of the final product. Particularly small crystallites (3.9 – 4.5 nm) were formed using polyvinylpyrrolidone as a surfactant, higher amount of PVP in the primary solution determined the reduction of the crystallite size in the final product. Significant changes were observed by varying the heat-treatment temperature, as listed in Table 2. The effect of calcination temperature on crystallite size of CeO_2 is also presented in *Figure 21*.

It is obvious that the effect of sintering occurs in the material during the heat-treatment [162]. Table 2 and *Figure 21* clearly demonstrate that increase of the calcination temperature from 100 to 300 °C causes insignificant growth of CeO_2 nanoparticles.

However, a considerable effect of the temperature on crystal growth shows up after raising the calcination temperature to over 500 °C. An exponential dependency of CeO_2 crystallite size on the calcination temperature was observed, which is in good agreement with the results obtained by other researchers and indicates that crystallite growth is diffusion related [163].

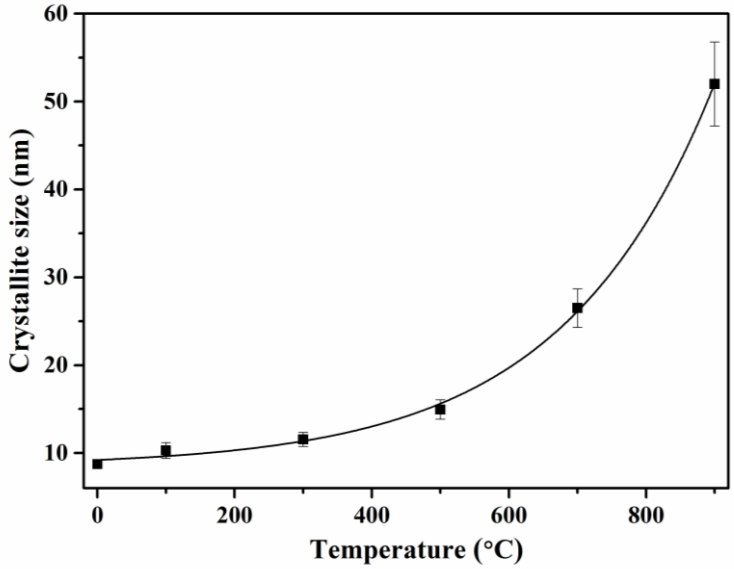

Figure 21. *The effect of the calcination temperature on crystallite size of CeO_2 nanoparticles (a line was just drawn to guide an eye).*

The values of the lattice parameter *a*, calculated from the XRD data, are presented in Table 2. The unit cell parameter values for CeO_2 nanostructures are larger if compared to those reported for the bulk cerium oxide (a = 0.5414 nm) in the standard data PDF-4+ (ICDD) 04-011-8929. Oxide nanoparticles exhibit a lattice expansion with the decreasing particle size when the particle size is less than 20 nm [164, 165]. It was also observed in our study that crystallite growth is responsible for the decreased value of the lattice parameter. However, it could not be applicable for the samples calcined at 900 °C, which consisted of larger than 20 nm nanoparticles. For these samples the lattice parameter *a* is close to the initial value of 0.5417 nm of the unheated samples. The increase of the lattice parameter could be related to the higher surface to volume ratio in the smaller particles, which results in a higher contribution from the surface layer [166]. However, it is also possible to attribute the lattice expansion with decreasing particle size to an increase in vacancy or impurity concentrations. During the defect formation in ceria through a reduction process, oxygen vacancies are created with charge compensation through two electrons, localized on trivalent cerium cations forming small polarons [167]. A larger fraction of the atoms with reduced coordination are present on the surface of CeO_2 particles as the particle size decreases what results in CeO_{2-x} structure formation. Hence, more polarons are present at the surface of smaller ceria NPs [168, 169]. Since the effective ionic radius of Ce^{3+} ion is about 14% larger than that of Ce^{4+} for the same coordination number, introduction of Ce^{3+} ions into the crystal lattice is likely responsible for the lattice distortion and increasing lattice parameter [167-170].

The Raman spectra confirm the formation of CeO_2 particles crystallizing in the cubic crystal system [171]. Raman spectra of synthesized CeO_2 nanoparticles are presented in *Figure 22*.

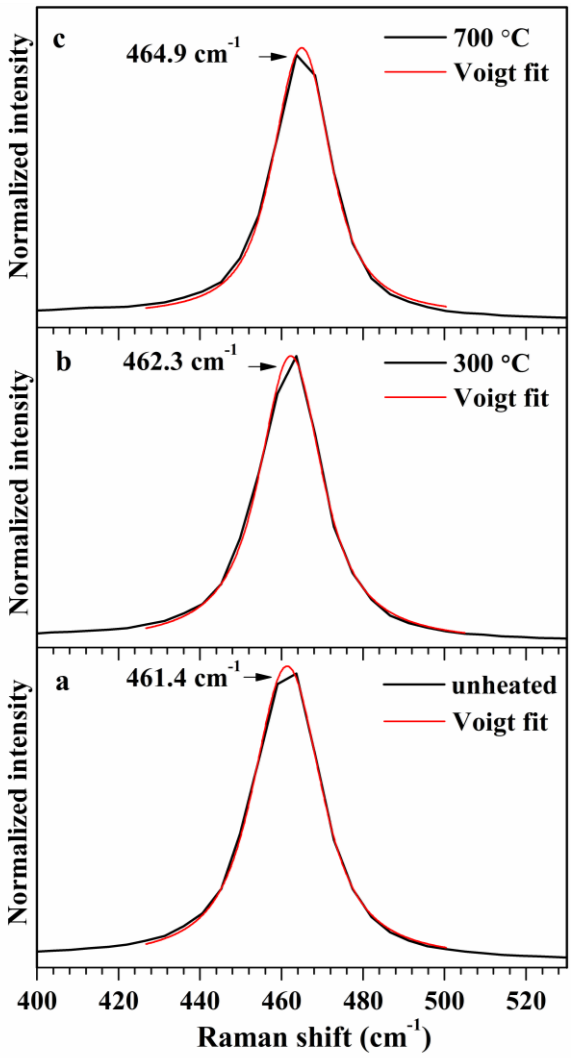

Figure 22. *Raman spectra of synthesized CeO_2 nanoparticles: unheated sample (a), sample annealed at 300 °C (b) and at 700 °C (c).*

The Raman-active mode in a single crystal ceria corresponds to the frequency of 466 cm^{-1}, referring to a symmetrical stretching mode of the Ce–O8 vibrational unit, which is very sensitive to any disorder in the oxygen sublattice resulting from grain size, doping and/or thermally induced non-stoichiometry [171]. Broadening of the Raman spectrum line, as well as increased line asymmetry and weak negative shift, are attributed to the reduction of the phonon lifetime in the nanocrystals. It reflects the influence of the microstructure of CeO_2 [168, 171]. The Raman spectra of synthesized CeO_2 nanoparticles exhibit single mode strong F2g peak in the range of 453.4 – 465.4 cm^{-1}. A more significant shift to the lower energy was

demonstrated by the unheated samples, especially those synthesized with PVP, while those calcined at higher temperatures, i.e. between 700 and 900 °C, exhibit Raman spectra similar to that of the single crystal CeO_2.

The particle size of the samples was estimated from the Raman line broadening using the following equation [171, 172]:

$$\Gamma = 10 + \frac{124.7}{D_r} \qquad \textbf{(10)}$$

Here Γ (cm^{-1}) is the FWHM of the Raman active mode peak and D_r is the particle size of a CeO_2 sample. The calculated particle sizes are slightly different if compared to those obtained from the XRD line broadening (Table 2). However, the trend remains the same, i.e. a longer irradiation period leads to the formation of slightly larger particles, whereas an increased calcination temperature is responsible for significant particle growth. Table 1 summarizes the results obtained from both Raman and XRD line broadening for different samples.

6.3. Annealing temperature impact on FTIR spectra

Fourier transform infrared spectroscopy has been usually employed as an additional probe to evidence the presence of OH groups. The FTIR spectra of as-synthesized and heat-treated samples in the range of 3600 to 450 cm^{-1} are presented in *Figure 23.* The broad band at 3000 – 3600 cm^{-1}, as well as the peak ca. 1620 cm^{-1}, are attributed to the O–H stretching mode and thus indicate the presence of adsorbed water [173]. The aforesaid bands and peaks become weaker upon raising the heat-treatment temperature and practically disappear after calcination at 700 °C. The remaining small peaks around 1600 cm^{-1} may be attributed to the moisture, adsorbed during the spectroscopic analysis. Therefore, it can be concluded that increasing the heat treatment temperature causes decomposition of hydroxyl groups.

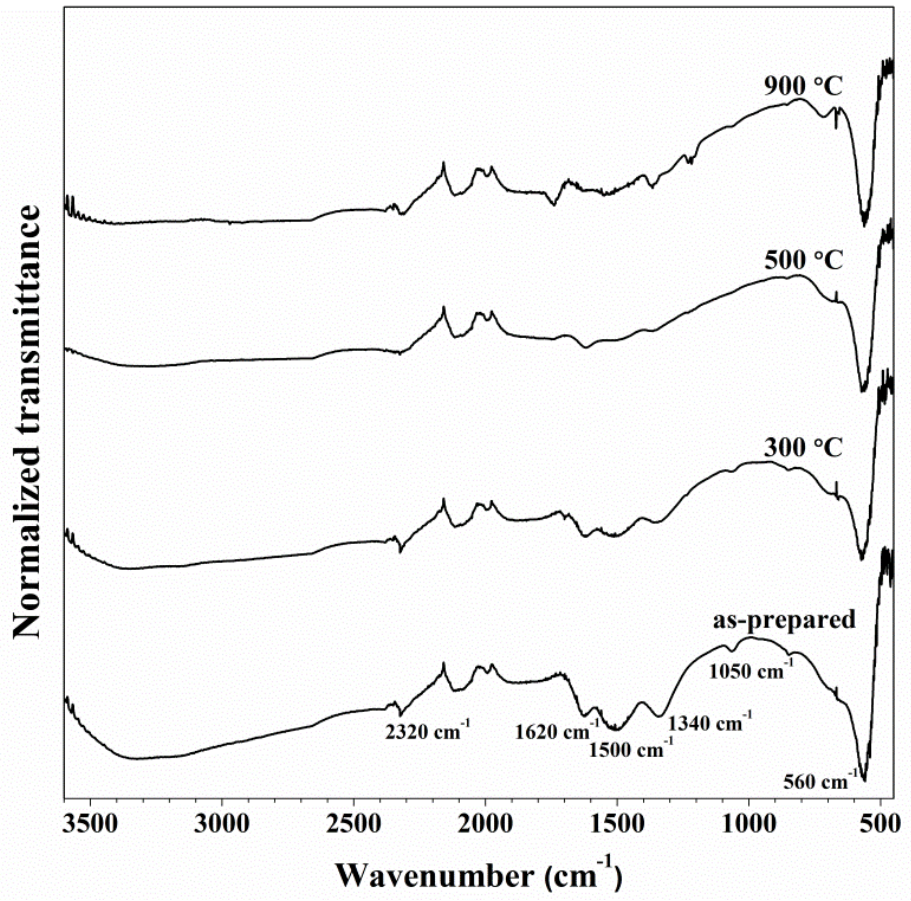

Figure 23. *FTIR spectra of CeO_2 nanoparticles annealed at different temperatures.*

The bands at 2320 and 1050 cm^{-1} have been attributed by other authors to the CO_2 asymmetric stretching vibration and C–O stretching vibration, respectively [174, 175]. The aforementioned bands represent CO_2, adsorbed on the metal cations [172] and the presence of "carbonate-like" species on the particle surface. Carbonate species vibrations are also reflected by the absorption bands, located at 1340 and 1500 cm^{-1} [173, 176]. These bands are clearly attenuated after the calcination, which indicates decomposition of carbonate species during the heat treatment and confirms the obtained TGA data. The band due to the stretching frequency of Ce–O can be observed at around 550 cm^{-1} (caused by the envelope of the phonon band of the metal oxide network) [177].

6.4. The effect of PVP

The morphology of CeO_2 samples was investigated by TEM as shown in *Figure 24* and *Figure 25*. TEM images revealed that synthesis without surfactants resulted in the formation of small, albeit highly agglomerated polyhedral particles with an average size of 15 ± 2 nm. The agglomeration of ceria nanoparticles is basically determined by the attraction of particles and repulsive forces. It can be modified by adjusting the concentration of the nanoparticles precursors [178], pH of the solution, addition of surfactants, and other experimental conditions.

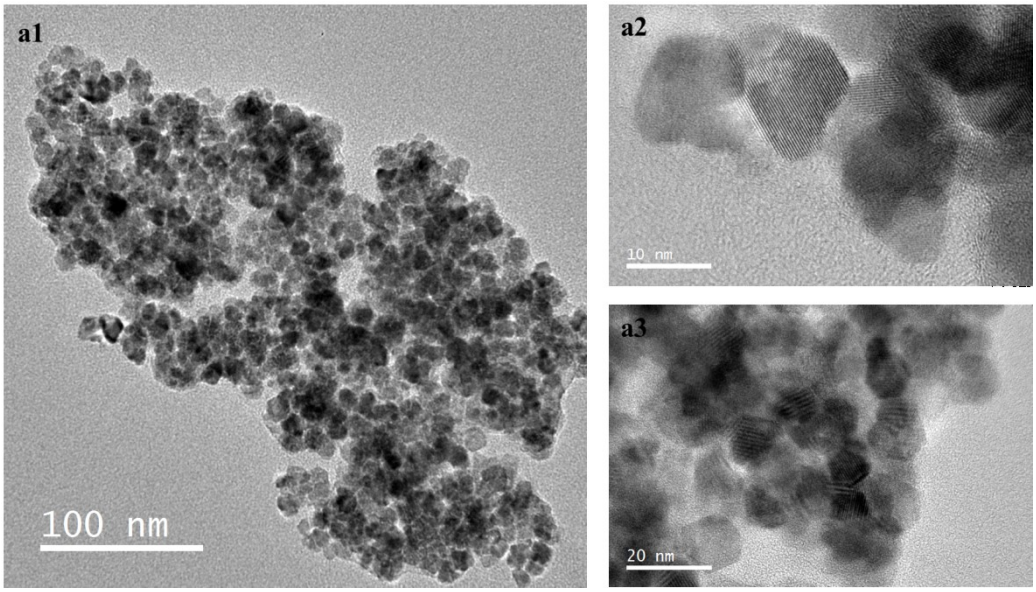

Figure 24. *TEM image of CeO_2 nanoparticles, prepared from the aqueous 0.03 mmol/L $Ce(NO_3)_3$ solution without PVP. Irradiation interval – 90 min.*

Since ceria nanoparticles contain oxygen vacancy sites as Lewis acidic sites, some hydroxyl ions from water are usually attracted to its surface resulting in slightly decreased pH value of an aqueous dispersion [179]. Attraction of surface hydroxyl groups between adjacent CeO_2 particles results in coalescence of the nuclei and thus formation of larger nanoparticles as well as increased agglomeration ratio [99], the latter phenomena becoming more significant with the increasing pH value. Regarding this, one could make an

assumption that agglomeration should decrease in rather acidic suspensions. Indeed, it is reported that quite stable dispersions of small CeO_2 nanocrystals could be obtained in solutions at a pH value below 2.5 [180]. In this case, some of the hydroxide ions at the surface of CeO_2 NPs are protonated, leading to formation of positively charged particles. Positive charges are compensated by nitrate anions in the electrical double layer (Stern and the diffuse layers) surrounding the particles [181, 182]. Increasing the pH causes relaxation of the bounded nitrate ions which are further replaced by the hydroxyl groups.

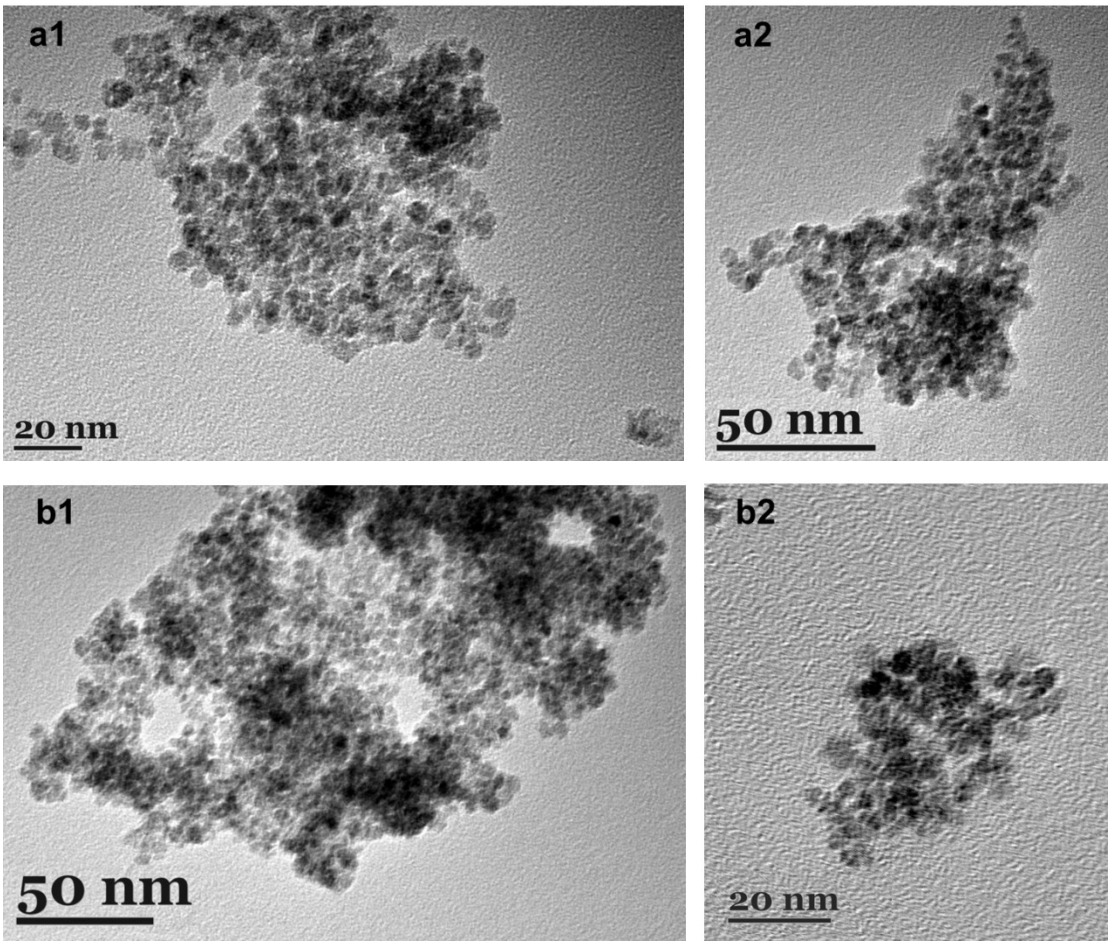

Figure 25. *TEM images of CeO_2 nanoparticles synthesized using PVP: (a1; a2) - 2.5 mmol/L PVP, irradiated for 90 min; (b1; b2) – 5 mmol/L PVP, irradiated for 90 min.*

The onset of aggregation could also be shifted to a higher pH by the addition of surfactants. In this case, nitrate ions would be substituted with the surfactant molecules and stronger steric forces between surfactants would

prevent the coagulation of nanocrystals. PVP, for instance, is expected to stabilize CeO_2 nanoparticles through the interaction between the hydroxyl groups/lactam groups of the polymer and surface hydroxyl groups of ceria [178], the agglomeration of CeO_2 nanocrystals could thus be adjusted by the attractive force (oriented aggregation by sharing a common crystallographic orientation) and repulsive force (steric hindrance effect from PVP or electrostatic repulsion from covalent bound nitrite ions).

It could be seen in *Figure 25* that adding PVP to a primary solution results in slightly decreased agglomeration as well as smaller particles with regard to the surfactant-free synthesis. Relatively high agglomeration is, however, naturally expected considering the ultra-small size of the particles. It turns out that a higher PVP concentration in the primary solution is responsible for the reduction in particle size: in other words, particles with an average size of 5.0 to 6.0 nm were formed if the PVP concentration in the primary solution was 2.5 mmol/L. Moreover, using a 5 mmol/L PVP solution caused formation of 3.5 – 4.8 nm particles. The TEM images confirm the obtained results from the powder X-ray diffraction analysis and Raman spectroscopy.

In order to better understand the interaction between ceria and PVP, TG analysis has been performed. The TG curves of those CeO_2 nanoparticles, synthesized either without any surfactant or synthesized by using different PVP concentration in the primary solution are presented in *Figure 26.*

The total weight loss of particles, synthesized without using surfactant (a), is not very high (8.4%), which indicates that the amount of adsorbed water and hydroxyl groups in the as-synthesized material is rather limited. The main weight loss can be observed up to 200 °C, which is attributed to the evaporation of adsorbed water and dehydration of the dried material (weight loss 4%). The minor weight loss above 200 °C is related to the losses of remaining CO_2 [183], which is in good agreement with FTIR data. No significant weight loss occurs when the temperature is raised above 600 °C, revealing that all volatile components leave the product before this temperature.

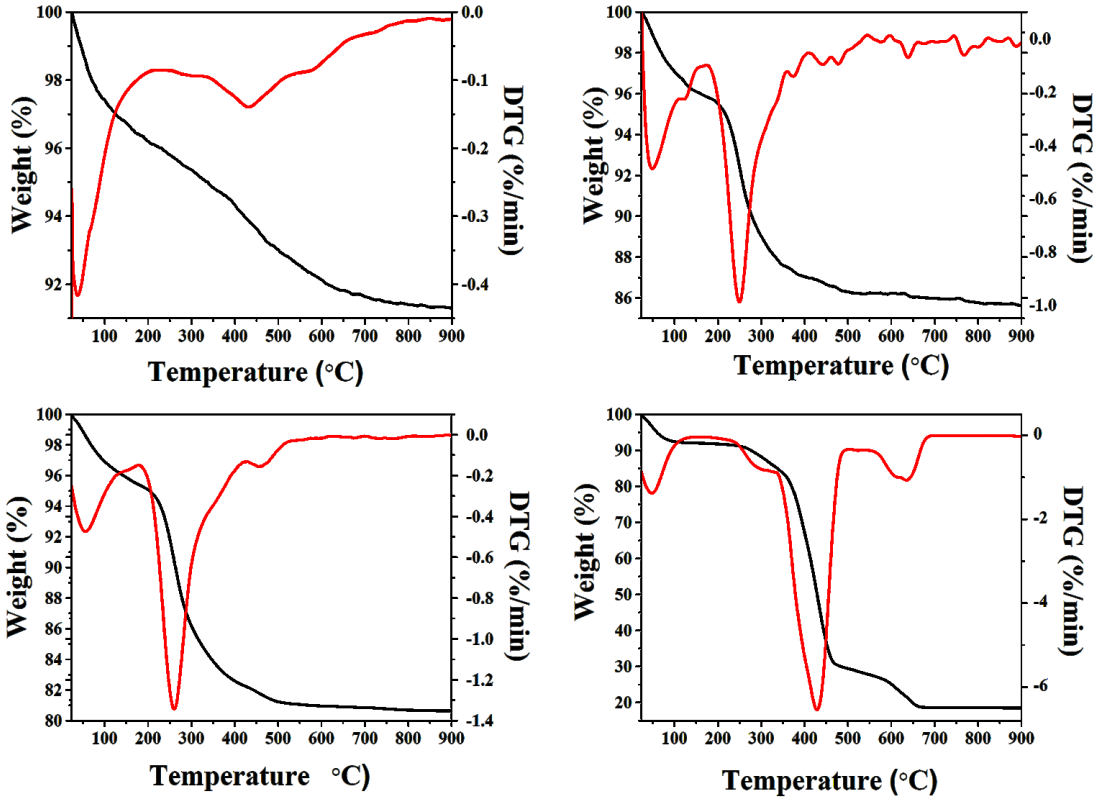

Figure 26. *TG-DTG curves of synthesized CeO_2 nanoparticles: (a) irradiated for 90 min, without PVP, (b) irradiated for 90 min using 1 mmol/L PVP, (c) irradiated for 90 min using 2.5 mmol/L PVP, (d) irradiated for 90 min using 5 mmol/L PVP.*

The TG curves obtained for the samples, prepared with polyvinylpyrrolidone as a surfactant, show different trends. The total weight loss (15%) of the sample prepared using 1 mmol/L solution of PVP (b) consists of three main steps from room temperature to 700 °C. The 5% weight loss up to 200 °C is related to the evaporation of residual water. The intense weight loss of 9% occurs in the temperature range of 200 – 500 °C due to the combustion of organic residues (PVP). Similar weight loss steps can be observed in the samples prepared with a higher amount of surfactant. The major weight loss in the range of 200 to 500 °C is larger in this case and reaches 13% if 2.5 mmol/L PVP is used for the synthesis (c) while the weight loss of 52% occurs when synthesis is carried out in a 5 mmol/L PVP solution (d).

It can be concluded that a relatively high percentage of residual PVP in the final product indicates a strong interaction between CeO_2 nanoparticles and

polyvinylpyrrolidone. The exact function of PVP is yet to be fully understood, but it is assumed that the strong selective interaction between the surface of CeO_2 nanoparticles and PVP through coordinative bonds with the O- and N-atoms of the pyrrolidone ring plays a major role in determining the product morphology.

6.5. Optical properties of CeO_2 samples

According to the literature, the band gap of bulk CeO_2 is around 3.00 eV [56]. It corresponds to a charge transfer between the fully occupied 2p (O^{2-}) orbitals and the empty 4f (Ce^{4+}) orbitals [170, 184]. The band gap value is reported to be different for nanomaterials with a particle size down to a few nanometers [185].

UV–VIS spectroscopy experiments were carried out by dispersing ceria particles in deionized water. *Figure 27* shows the UV–VIS absorption spectra of CeO_2 NPs synthesized under different conditions. In all cases, a strong absorption below 400 nm occurs with a well-defined absorption peak in the range of 295 – 340 nm (depending on the synthesis and calcination temperature). Increasing the calcination temperature causes red shift of the absorption maximum due to the formation of larger particles.

Fitting the absorption data to the direct allowed transition equation (7) and extrapolating linear portions of the curves towards absorption equal to zero (y = 0) enables to estimate the E_g value for the direct transition [172]:

$$\alpha h\nu = A(h\nu - E_g)^{\frac{1}{2}} \qquad \textbf{(11)}$$

Here α – optical absorption coefficient, $h\nu$ – photon energy, E_g – direct band gap, and A is a constant.

The plot of $(\alpha h\nu)^2$ is shown in the insets of *Figure 27*. The estimated optical band gaps for various CeO_2 samples are presented in Table 2.

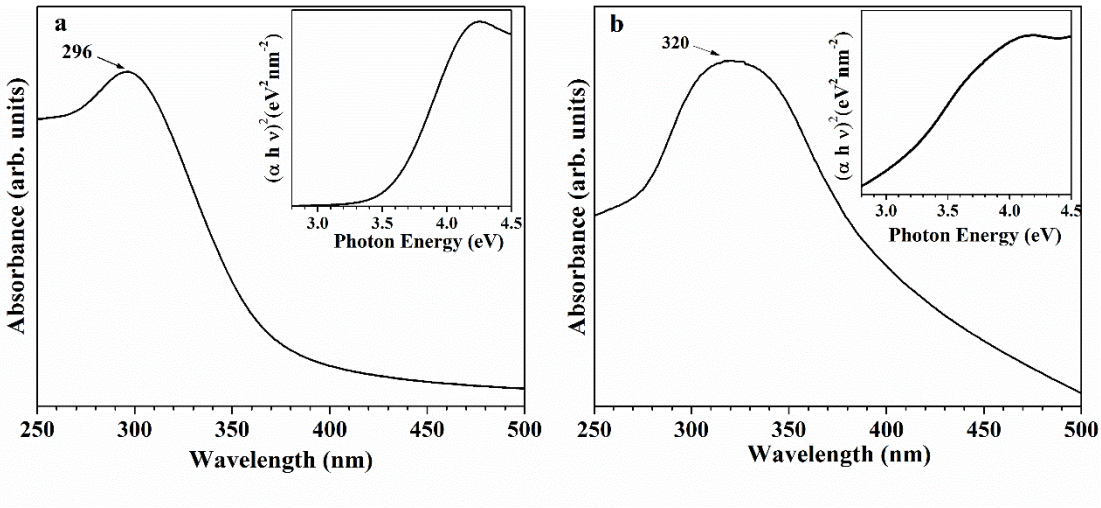

Figure 27. *Room temperature optical absorbance spectrum of the samples and the plot of $(\alpha h\nu)^2$ (the inset): (a) unheated CeO_2 sample, (b) CeO_2 sample annealed at 900 °C for 5 h.*

The increased optical band gap of CeO_2 nanoparticles can be explained twofold: (i) by quantum confinement effect for particle sizes down to less than a few nanometers and (ii) by electrostatic potential effect which is closely related to the oxygen vacancy concentration. Following the quantum confinement effect, the band gap increases with decreasing nanoparticles size. For spherical nanoparticles with an infinitely high potential energy outside the sphere, the band gap value can be determined from the following equation [166, 186]:

$$E_{g,eff} = E_g(\infty) + \frac{h\pi}{2R^2}\left(\frac{1}{m_e} + \frac{1}{m_h}\right) - \frac{1.8e^2}{\varepsilon R} \qquad \textbf{(12)}$$

Whereby E_g is the bulk band gap, R is the radius of the nanoscale particles, m_e and m_h are the effective masses of the electron and hole, respectively, h is the Planck constant, and ε is the relative dielectric constant of CeO_2.

The quantum size effect has been reported by many authors. A blue shift in the UV absorption spectra of optical band gap with decreasing of

nanoparticle diameter (d ~ 1.6 nm) was observed by Tsunekawa *et al*. [187]. Masui *et al*. [188] observed that the band gaps of 4.1 and 2.6 nm CeO_2 nanoparticles are 3.38 and 3.44 eV, respectively.

The electrostatic potential effect is related to the charge transition of the Ce ion. It is well known that Ce^{4+} ions coexist with Ce^{3+} ions. The latter can be attributed to the oxygen vacancies located at the surface of nanoparticles. The correlation between the blue shift of the optical band gap of the nanocrystalline CeO_2 films and a decrease in Ce^{3+} content was observed by Patsalas *et al*. [189]. According to Chen *et al*., [72] the content of Ce^{3+} and oxygen vacancies decreases with growth and oxidation of the nanoparticles (with grains of 10 – 20 nm) during annealing in an O_2 rich atmosphere. Hence, the blue shift of the band gap was mainly promoted by the valence and oxygen vacancies state change.

The quantum confinement effect would be an appropriate explanation for the increased band gap when particle size is less than 3 nm. In our case, this explanation could be ruled out since the size of the synthesized nanoparticles is in the range of 3.3 – 58.6 nm. Thus, we can conclude that the metal-to-metal charge transfer (MMCT) of Ce ions (Ce^{3+} – Ce^{4+}) plays possibly the major role in determining the band gap of the samples.

Chapter 7. Photochemical synthesis of Ag-CeO_2 nanostructures

Unlike other wide band gap semiconductors, TiO_2 and ZnO, photocatalytic properties of ceria have not been extensively studied. Nevertheless, lower toxicity and longer charge separation make ceria one of the potential substitutes for both of the aforementioned compounds not only in sunscreen cosmetics, but also in environmental processes. Therefore, following the idea of green photochemical synthesis, we developed a method for Ag-CeO_2 nanoheterostructures preparation with ceria nanoparticles serving both as a photoactive material and as a metal nanoparticle support. This chapter describes the development and optimization of the synthesis process together with a detailed characterization of the products obtained.

7.1. Designing CeO_2 synthesis process: obtaining a suitable precursor for Ag-CeO_2 nanoheterostructure formation

In order to successfully synthesize Ag-CeO_2 nanoheterostructures, the most appropriate starting materials should be chosen in the first place. Several different variations of ceria nanoparticles preparation via photochemical route, as well as the further applied heat-treatment, were presented in Chapter 5. However, taking into consideration different aspects of possible Ag nanoparticle formation, one particular attempt was chosen for ceria NPs preparation. First of all, the influence of ceria precursor was evaluated.

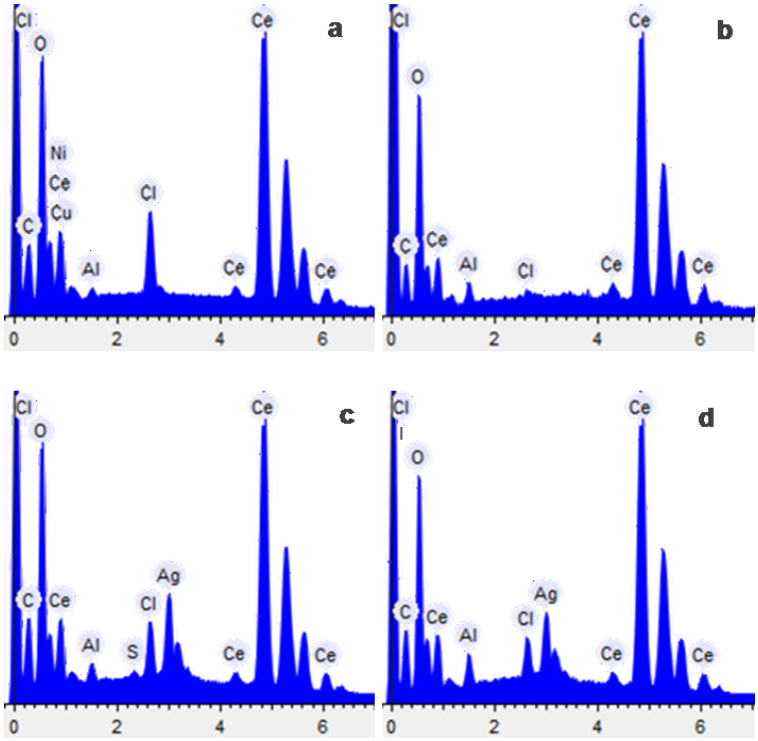

Figure 28. *EDX spectra of CeO_2 nanoparticles (a,b) and Ag-CeO_2 nanostructures (c,d), $CeCl_3 \cdot 7H_2O$ was used as CeO_2 precursor in all of the cases: a - CeO_2 NPs, washed with DI water once; b - CeO_2 NPs, washed with DI water six times; c - Ag-CeO_2 nanostructures, prepared using once washed CeO_2 NPs; d - Ag-CeO_2 nanostructures, synthesized using six times washed CeO_2 NPs. Al, Cu and Ni signals arise from the metallic sample holder while carbon tape is responsible for the carbon signal. The latter signals, however, are of no significance for the present study.*

Although both $Ce(NO_3)_3 \cdot 6H_2O$ and $CeCl_3 \cdot 7H_2O$ could be used as starting materials for CeO_2 formation with no significant differences in the final products being observed (Section 6.2), even a small amount of residual chloride would participate in a reaction with silver ion because of the low solubility product constant of AgCl ($K_{sp\ (AgCl)} = 1.77 \times 10^{-10}$ [33]). Unavoidable formation of some AgCl was observed in our study, even if CeO_2 particles were washed numerous times before the reaction with silver salt. Despite the extra small amount of the residual chlorine in the case of pre-washed CeO_2 nanoparticles (*Figure 28*, b), significant amount of AgCl was detected in Ag-CeO_2 system (*Figure 28*, d; *Figure 29*, b). Considering this, cerium nitrate was chosen as the cerium source.

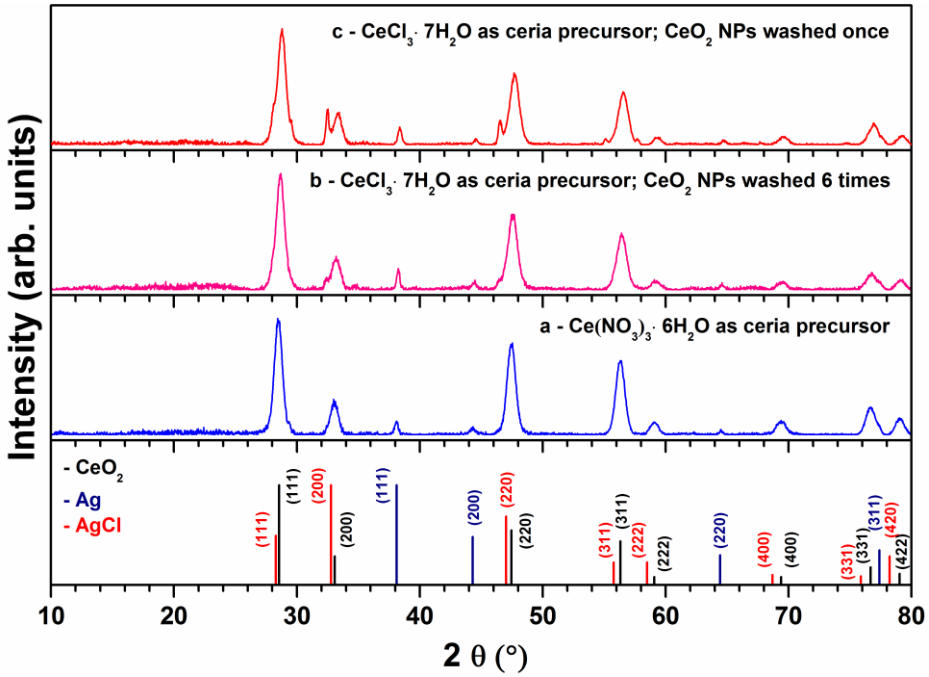

Figure 29. *XRD patterns of CeO_2-Ag nanocomposites: a - $Ce(NO_3)_3 \cdot 6H_2O$ used as a ceria precursor; b - $CeCl_3 \cdot 7H_2O$ used as a ceria precursor, the obtained CeO_2 nanoparticles washed 6 times before the reaction with silver salt; c - $CeCl_3 \cdot 7H_2O$ used as a ceria precursor, the obtained CeO_2 NPs washed once before the reaction with silver salt.*

The need of using surfactants for photochemical synthesis of CeO_2 nanoparticles is rather questionable in this case. Even though PVP was found to be capable of reducing the agglomeration ratio of ceria NPs slightly, the rate of this effect was not significant enough to obscure the potential loss of the photocatalytic properties of the nanoparticles. It is expected that the polymer would be able to block a number of active sites of catalytic materials due to the strong interaction between the metal surface and the sterical hinders, thus leading to the loss of catalytic activity to a great extent. The strong interaction between CeO_2 nanoparticles and polyvinylpyrrolidone, revealed by TG analysis, rather confirmed than refute the latter assumption [190]. Moreover, another PVP-related effect, the formation of extra small (3 – 5 nm) ceria nanoparticles, was not the most desired process as it was expected that silver will mainly form larger than 5 nm nanoparticles due to its high surface energy [191].

Other essential constituents of the synthesis conditions were the concentration of the CeO_2 precursor and the irradiation time. Twice lower $Ce(NO_3)_3 \cdot 6H_2O$ concentration than in the initial synthesis (14.4 mmol/L instead of 28.8 mmol/L) was used expecting to reduce the agglomeration. Irradiation time, in contrast, was prolonged to 300 min in order to obtain larger nanoparticles with a better yield.

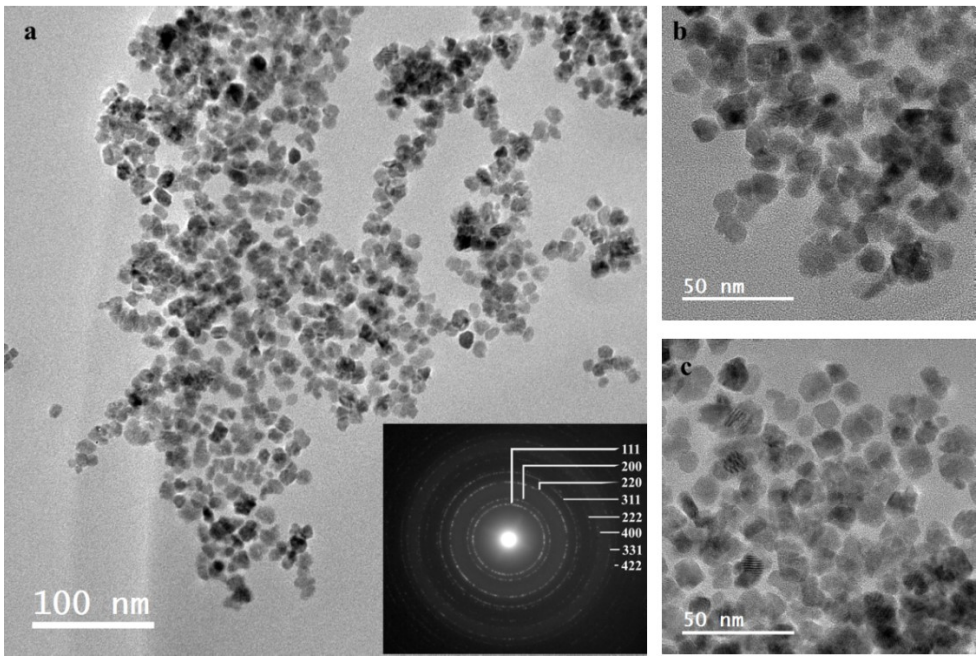

Figure 30. *TEM images (a, b c) and electron diffraction pattern (inset of a) of CeO_2 sample, prepared from the aqueous 0.015 mmol/l $Ce(NO_3)_3$ solution without PVP. Irradiation time – 300 min.*

Figure 30 presents the morphology of the CeO_2 sample, synthesized for 5 hours under UV irradiation. The related electron diffraction pattern (inset of *Figure 30 a)* shows reflection lines compatible with the cubic fluorite structure ($Fm\bar{3}m$) of CeO_2 (reference data: PDF-4+ (ICDD) 04-011-8929). It is clear that the average crystallite size, estimated from the Scherrer's equation (13.9 ± 0.9 nm), is in good agreement to the TEM data: average crystallite size was determined to be around 14 nm (*Figure 31*). Even though no surfactants were applied for the latter synthesis, the agglomeration ratio was significantly lower with respect to the CeO_2 nanoparticles prepared with a twice higher ceria precursor concentration and polyvinylpyrrolidone (*Figure 25*).

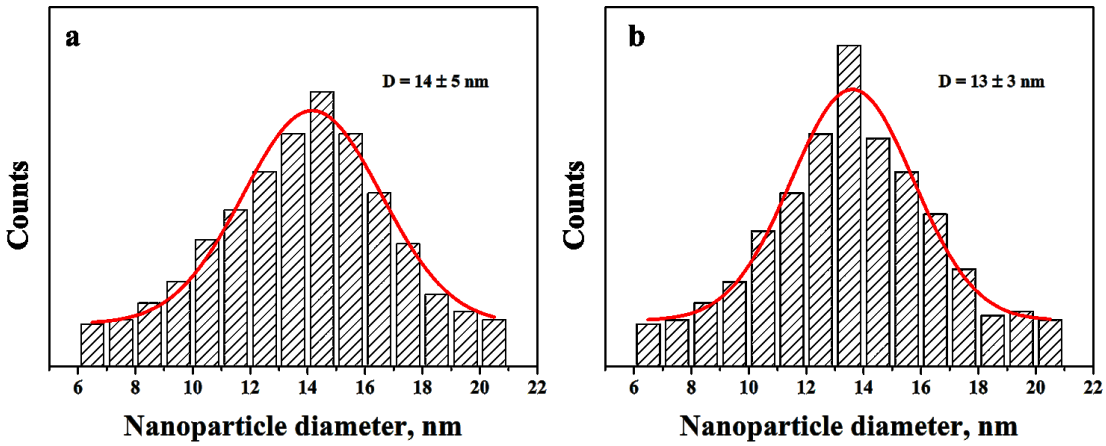

Figure 31. *Size distribution of CeO_2 samples: a – prepared from the aqueous 0.03 mmol/L $Ce(NO_3)_3$ solution without PVP. Irradiation time – 90 min, calcined at 500 ºC for 5 h; b –prepared from the aqueous 0.015 mmol/L $Ce(NO_3)_3$ solution without PVP. Irradiation time – 300 min. The particle size was estimated from TEM images using program ImageJ, at least 300 particles were measured for the size analysis.*

The possibility to apply heat-treated ceria NPs was considered as well. In fact, particles of similar size with an agreeable size distribution were obtained by both irradiating the solution for 5 h or by heating for 90 min irradiated particles at 500 ºC (*Figure 31*). Nevertheless, remarkably increased agglomeration was observed in the latter case, making this option out of the question. Thus finally, a decision was made to use CeO_2 NPs, synthesized without PVP for 5 h under the UV irradiation.

7.2. Formation of Ag-CeO_2 nanoheterostructures

Taking into consideration semiconducting properties of cerium oxide nanoparticles, the photochemical route was seen as a promising way to form noble metal-ceria nanoheterostructures *in situ* by reducing noble metal ions adsorbed on the surface of the semiconductor NPs. Unlike in the process presented by Scirè *et al.* [130], metal ions were not reduced prior to the combination with a suitable support. On the contrary, CeO_2 ability to generate conduction band electrons under exposure to UV light was expected to play a key role in the reduction of silver ions. Not only is the proposed synthesis

pathway a clean route to the formation of the nanoparticles with no potential damage to the environment, it also provides the possibility to create small uncoated nanostructures with a “clean” surface as no capping agents or organic photoactive compounds are involved in the process. From the application point of view, any residue of amines, polymers or organic solvents, which are usually required in a photochemical synthesis mixture, should affect the performance of the nanoparticles significantly [107, 192].

Thus, the obtained CeO_2 nanoparticles were applied for the photochemical synthesis of Ag-CeO_2 nanoheterostructures in the aqueous solution. Obvious color change of the aqueous suspensions was the primary evidence of the reaction: after irradiation by a Mercury lamp, the slightly yellowish suspension of CeO_2 nanoparticles and silver precursor became light yellow-greenish. The final color of the colloidal aqueous solution ranged from pale yellow to dark brown, as the irradiation time varied from 10 to 120 min, respectively, with the initial $AgNO_3$ content being 3.5 mmol/L (*Figure 32*, a1). Varying the initial $AgNO_3$ concentration influenced the color of the final product as well: paler suspensions were obtained using lower concentration of the silver precursor while those containing higher amount of silver salt were darker after the same irradiation time. Rapid and more intense color changes under UV light were exhibited by aqueous solutions containing ethanol (*Figure 32*, b1). It was previously observed that yellow or brownish color of colloidal silver nanoparticle solutions implies typically the formation of quasi-spherical silver nanoparticles while red, dark green or blue color is exhibited by solutions containing silver nanoplates and greenish-gray by silver nanorods colloidal solutions [75, 193-195].

Formation of the Ag-CeO_2 system was further observed by UV-VIS spectroscopy. Before irradiation, the typical steep absorption of ceria nanoparticles was observed below 350 nm, with a negligible tail in the visible region. Irradiation of deaerated CeO_2 suspensions in the presence of Ag^+ ions resulted in the rise of a strong band with the maximum at 391 – 422 nm in the absorption spectra of the solutions (*Figure 32*, a2; b2). Similar absorption bands

were reported for colloidal solutions of small (1–100 nm) metallic silver particles [196, 197]. The observed absorption band is obviously a result of the surface plasmon resonance, which occurs when the colloidal solutions of silver nanoparticles are exposed to an electric field or electromagnetic radiation. SPR can only be observed when the particle size decreases below the mean free path of the electron [81, 198]. Silver nanoparticles are reported to exhibit Surface Plasmon absorption Band (SPB) in the range of 400–870 nm, depending on their size and morphology [75, 81, 199, 200]. For spherical or nearly spherical Ag nanoparticles, the position of SPB is reported to be around 400 nm [75, 193, 195, 200], whereas a shift in the plasmon absorption band from 400 to 670 nm indicates the particle shape changing from a sphere to a cube [7]. SPR peak maxima of selected samples are presented in Table 3.

Surface Plasmon absorption Band was not observed when the reaction was performed in the presence of oxygen probably due to the intense formation of highly reactive secondary oxidants ($^{\bullet}HO_2$, H_2O_2) under UV irradiation [201]. Since electronic potential of the conduction band bottom of CeO_2 (~-0.685 V vs NHE at pH =7, depending on the bandgap of particular NPs) [21] is more negative than that of superoxide radical (E_0 ($O_2/^{\bullet}O_2^-$) = -0.33 V vs NHE at pH = 7) [202], it is expected that photogenerated electrons at the conduction band of CeO_2 would cause formation of $^{\bullet}O_2^-$.from O_2 that, in turn, would originate $^{\bullet}HO_2$, H_2O_2. Therefore, while performing the synthesis in deaerated solutions, formation of $^{\bullet}HO_2$ and H_2O_2 could be largely suppressed [134].

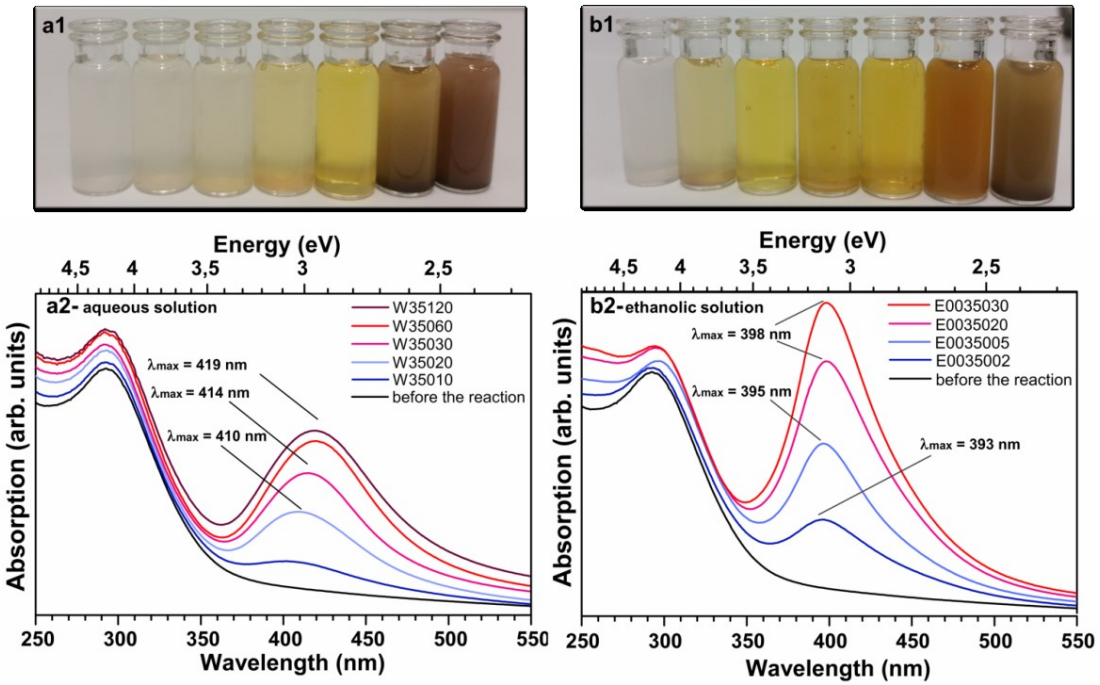

Figure 32. *Irradiation time-dependent final color of the colloidal solutions (a1, b1) and absorption spectra of the Ag-CeO_2- dispersions (a2, b2): (a) – 3.5 mmol/L $AgNO_3$, (b) – 0.035 mmol/L $AgNO_3$, 20% v/v EtOH solution. Irradiation time as follows: 0; 10; 20; 30; 60; 90; 120 min for a1 and 0; 2; 5; 30; 60; 90; 120 min for b1 (from left to right).*

In the case of pure aqueous solution, the lowest sufficient $AgNO_3$ concentration for the reaction to occur was found to be 2.0 mmol/L. Small rise of SPB band was detected after 10 min of irradiation (sample W2010) in this case, while prolonged irradiation time was responsible for increased intensity of the aforesaid band as well as a significant red shift, indicating growth of the metallic nanoparticles. Furthermore, extremely broadened SPR with a significantly decreased intensity and λ_{max} shifted from 400.3 ± 1.7 nm to 421.5 ± 0.5 nm was exhibited after 90 min of exposure to UV light while further irradiation caused subsequent decrement of SPR band intensity followed by a total attenuation of the peak after 150 min of irradiation for the sample W20150 (*Figure 33*). We assumed that this is the evidence of oxidative processes and the formation of oxide layers (Ag_2O) on the particle surface [203, 204] induced by a long exposure to UV light.

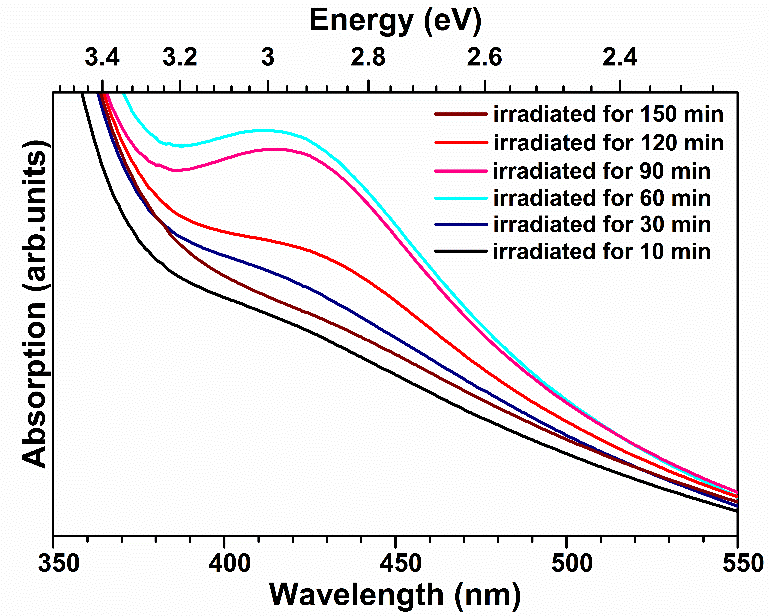

Figure 33. *Irradiation time-dependent absorption spectra of the aqueous Ag-CeO_2 dispersion; c($AgNO_3$) = 2.0 mmol/L.*

A major challenge of using light for the synthesis is undoubtedly the complexity and often unpredictability of the chemical transitions that could be possibly induced in a reaction solution by irradiation. It is well established that light induces a number of redox processes in the medium to produce active species that later reduce metal ions.

The suggested mechanism of silver nanoparticle formation in the presence of ceria is briefly presented in *Figure 34*. Following the absorption of light, valence electrons in O 2p band are excited and jump to the higher energy level. The excited electrons in ceria conduction band should be capable of reducing silver ion to form metallic silver particles.

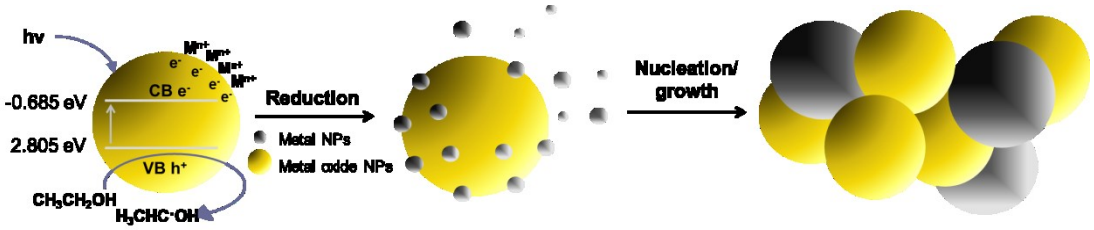

Figure 34. *Photochemical route to the formation of metal-semiconductor nanoheterostructures. CB – conduction band; VB – valence band; M – Ag, e^- – photoexcited electrons; h^+ – photoexcited holes.*

The main spectrum lines of the mercury discharge lamp, which was used as a light source, are 180 (~6.9 eV) and 254 nm (~4.9 eV) (Section 5.2). Considering this, one might think that many electrons should gain enough energy to overcome the 2*p-5d/6s* gap of ceria (~6.0 eV) and to create unbound electron-hole pairs by entering the empty 5d orbital (see Section 2.1.). However, it should not be forgotten that high energy Vacuum UV-light (VUV, λ <200 nm) is to a great extent absorbed by the solvent (water, ethanol) [205]. Thus, even though some electrons could gain enough energy to enter the empty 5d orbital, electronic transition between the valence band and Ce 4f block ($O2p^6 \rightarrow Ce4f^0$) rather than $O2p^6 \rightarrow Ce\ 5d/6s^0$ transition should be the dominant process in our case.

Regarding this, the conduction band and valence band potentials of a semiconductor were determined according to the Equations [206]:

$$E_{CB}^{0} = -\chi + \frac{1}{2}E_g \qquad \textbf{(13)}$$

$$E_{VB}^{0} = -\chi - E_g \qquad \textbf{(14)}$$

where E^0_{CB} and E^0_{VB} are conduction band and valence band potentials, respectively; χ is the absolute electronegativity of the semiconductor (5.56 eV for CeO_2) [207]. E_g is the band gap energy of CeO_2 (14 nm CeO_2 nanoparticles with E_g = 3.49 eV were applied for the synthesis as indicated in Table 2).

For conversion between the absolute potential level *E* and the NHE level *E*(NHE), the following formula was applied [90]:

$$E(NHE) = -4.5 - E \qquad \textbf{(15)}$$

-4.5 is the absolute hydrogen electrode potential (-4.5 eV vs AVS for 0 eV vs NHE).

According to our calculations, strongly oxidative (E^0_{VB} = +2.805 eV vs NHE) valence band hole (VB h^+) and moderately reductive (E^0_{CB} = -0.685 eV vs NHE) conduction band electrons (CB e^-) are forming.

Electron-hole pairs are separated and transferred to the surface of the semiconductor, CeO_2 in this case. CeO_2 CB e^-, which do not recombine with VB h^+, are capable of reducing silver ions [200]. A fast charge recombination of VB h^+ and CB e^- would annihilate the charge-separated state leading to an energy waste without the possibility of providing electrons for Ag^+ reduction. It was revealed, however, by Corma *et al.* that the temporal profile of the charge separation of ceria is much longer-lived than that of TiO_2 under the same conditions [208], and titanium dioxide has been successfully applied for a similar photochemical synthesis of Me-TiO_2 nanocomposites already [9].

Nevertheless, even taking into consideration the relatively long lifetime of charge separation, the valence band holes, originating from photoexcitation of CeO_2 nanoparticles, are not to be forgotten. Some conduction band electrons will unavoidably experience recombination with them, resulting in a significant reduction of the overall reduction efficiency. One should also take into consideration that, following the absorption of high energy radiation, photolysis of water is bound to occur in the system. As a result, $^{\bullet}OH$ radicals are forming [209]. Some hydroxyl radicals can also be supplied by surface -OH groups from ceria NPs or generated by VB h^+. It is known that hydroxyl radicals are actually quite strong oxidizing agents with E^0 ($HO^{\bullet}/H_2O$) = +2.8 V vs NHE [210]. Hence, it could be inferred that a competition between two processes takes place in the presented system: reduction of silver ion by free electrons generated in ceria and oxidation of silver by $^{\bullet}OH$.

The latter process should be significantly suppressed by introducing $^{\bullet}HO$ radical scavengers, such as primary or secondary alcohols, into the reaction solution before irradiation, leading to the significantly increased reaction yield and formation of smaller silver nanostructures.

For instance, ethanol is capable of scavenging •OH radicals and photogenerated holes, converting them into secondary radicals [134]:

$$HO^{\bullet} + CH_3CH_2OH \rightarrow H_2O + H_3CHC^{\bullet}OH \qquad \textbf{(16)}$$

$$h^{+}_{VB} + CH_3CH_2OH \rightarrow H^{+} + H_3CHC^{\bullet}OH \qquad \textbf{(17)}$$

Alcohols with α-hydrogens are known to easily form α-hydroxyalkyl radicals upon α-H atom abstraction. Hence, reductive reactions can be strongly enhanced in deaerated ethanol containing solutions with respect to the pure aqueous media. Furthermore, $H_3CHC^{\bullet}OH$ radicals are capable of further injecting electrons into the CeO_2 conduction band or reduce Ag^+ ions, as E^0 for the C_2H_5OH / $H_3CHC^{\bullet}OH$ couple is -0.94 V vs NHE [211]. Hence, overall enhancement of the reduction process is expected to be a result of both efficient radical/hole scavenging and the additional silver ion reduction by the emerging $H_3CHC^{\bullet}OH$ radicals. Taking into consideration this double effect of ethanol, the overall silver ion reduction process could be described as:

$$Ag^{+} + e^{-}_{CB} \rightarrow Ag^{0} \qquad \textbf{(18)}$$

$$Ag^{+} + CH_3HC^{\bullet}OH \rightarrow Ag^{0} + CH_3CHO + H^{+} \qquad \textbf{(19)}$$

Following this idea, ethyl alcohol was added to the reaction solution before the irradiation. Indeed, using alcohol as a radical scavenger caused faster formation of Ag NPs with the lower amount of silver being required. The reaction occurred even when the maximum $AgNO_3$ concentration of 3.5 mmol/L was reduced 100 times: down to 0.035 mmol/L. *Figure 32* a2, b2 demonstrates SPB changes of samples containing 3.5 mmol/L in water and 0.035 mmol/L $AgNO_3$ in 20% v/v ethanol solution over the irradiation time, respectively. Significant rise in SPB was observed after 2 min of irradiation in the ethanol containing solution (sample E0035002), while a weak red-shifted SPB showed up only after 10 min of irradiation in the pure aqueous media

(sample W35010). Furthermore, rather low increase in magnitude with the increasing irradiation time was exhibited by the latter sample with respect to the radical scavenger containing solution. While increased irradiation time demonstrated a high impact on the size of silver nanoparticles in the aqueous media with the peak maximum being shifted from 400.7 ± 1.9 nm to 413.5 ± 3.6 nm after 30 min of exposure to UV light (Table 3), significantly weaker bathochromic shift of 5 ± 1 nm was observed in the ethanol containing solution. All this implies that smaller silver NPs with a narrower size distribution should be formed while using ethanol, the process being way more efficient if compared to that carried out in the pure aqueous media.

It should be mentioned that silver nanoparticles could be photochemically produced to a small extent directly from silver precursor solutions containing ethanol, with no photoactive compound required [212]. In our study, signs of silver nanoparticle formation in the control samples containing only $AgNO_3$ in 20% v/v ethanolic solution (*Section 5.4.1.*) were also observed. However, only traces of surface plasmon resonance band were demonstrated by the sample containing 0.035 mmol/L $AgNO_3$ while a sharp and well-defined SPB was the characteristic of the solution with the same silver precursor concentration in the presence of ceria (*Figure 32* b2). There are no doubts hence that photocatalytic reduction process involving the UV excited CeO_2 nanoparticles plays a key role in the silver ion reduction.

7.3. Characterization of the Ag-CeO_2 nanoheterostructures and optimizing of the synthesis conditions

Presence of pure metallic silver in the samples synthesized without radical scavengers and containing larger amount of Ag was confirmed by XRD analysis (see *Figure 35*). The intense diffraction peaks of CeO_2 at $2\theta = 28.6$, 33.1, 47.5, 56.3, 59.1, 69.4, 76.7, 79.1 and 88.4° are attributed to the (111), (200), (220), (311), (222), (400), (331), (420) and (422) planes of the fluorite structure of CeO_2 (PDF-4+ (ICDD) 04-011-8929), respectively. Three

additional diffraction peaks at 2θ = 38.07, 44.15 and 64.4°, attributed to (111), (200) and (220) Bragg's reflections of the face-centered cubic structure of Ag ($Fm\bar{3}m$) (reference data: PDF-4+ (ICDD) 01-087-0719), were clearly exhibited by samples with a higher silver concentration.

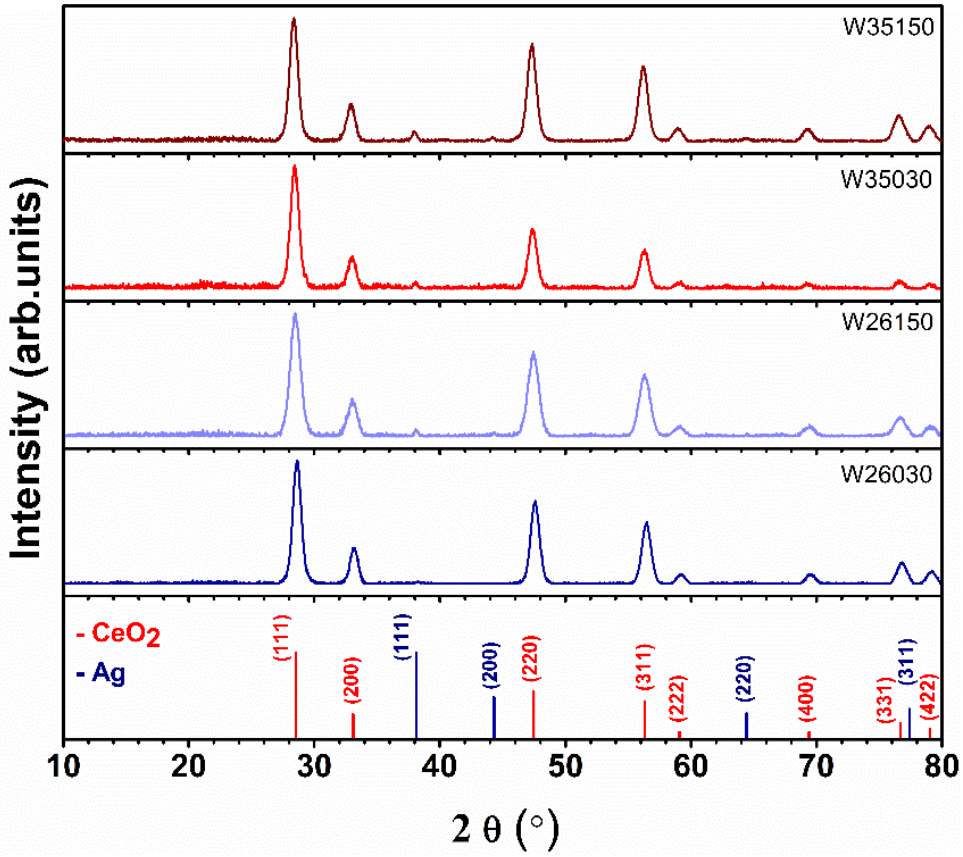

Figure 35. *XRD patterns of Ag-CeO_2 nanoheterostructures, synthesized in pure aqueous solutions. The XRD background occurring due to the used glass sample holder was subtracted from the measured XRD patterns.*

Sharper peaks at 2θ = 38.07, 44.15 and 64.4° were observed in the samples with prolonged irradiation time, implying the presence of relatively large silver nanoparticles, which was further confirmed by TEM analysis (*Figure 38*). Lowering $AgNO_3$ concentration caused a significant decrement of the silver peaks in the XRD pattern. Only a small trace of the peak at 38.07° can be observed in the XRD pattern when $AgNO_3$ concentration varies from 2.2 to 2.5 mmol/L while no evidence of metallic silver was observed in XRD patterns for $AgNO_3$ concentration below 2.0 mmol/L in the case of synthesis in

aqueous solution even if the irradiation time was prolonged up to 150 min. Low silver loading should result in formation of highly dispersed small Ag nanoparticles not capable of exhibiting an XRD peak. Although the samples synthesized using ethanol contained relatively high amount of silver, only traces of silver XRD peaks were exhibited by the latter nanostructures. We assume that in this case, no well-defined XRD peaks are observed probably due to the lack of large silver particles.

Although some tentative assessment of silver content in the samples could be done from its absorption spectra, more accurate determination of silver concentration is essential not only for the clearer general view, but also for determination of the reaction efficiency. Hence, surface composition of Ag-CeO_2 samples was evaluated using X-ray photoelectron spectroscopy (XPS). More precise information was acquired by measuring silver and cerium concentrations with the inductively coupled plasma optical emission spectrometer (ICP-OES). The sum of Ag and Ce amount was assumed as 100%. Determined Ag content varied from 0.40 ± 0.01 to 12.19 ± 0.07 at% in the final product (Table 3). It is clear that silver content depends significantly on the concentration of $AgNO_3$ and irradiation time: higher amount of silver precursor and longer irradiation time led to higher metallic Ag loading. The same trends were observed for the samples prepared with radical scavenger, yet ICP-OES results undoubtedly confirm the remarkably increased reaction efficiency after introduction of ethanol to the system: the amount of silver in the final product did not decrease by using significantly lower initial silver salt concentration in the presence of ethanol. On the contrary, almost twice higher silver loading was detected in the ethanolic samples with regard to the ones prepared under similar conditions but with a two order of magnitude higher $AgNO_3$ concentration and no radical scavenger (Table 3).

Table 3. Silver content, SPB position (λ_{max}) and Ag nanoparticle size in various Ag-CeO_2 samples.

Sample	Composition		SPB	Ag NPs size
	from XPS Ag (at-%)	from ICP-OES Ag (at-%)	λ_{max} (nm)	From TEM (nm)
W20030	0.81± 0.10	0.40 ± 0.01	415.6 ± 0.6	-
W20090		0.69 ± 0.01	421.5 ± 0.5	
W20150	1.94 ± 0.15	1.90 ± 0.16	attenuated	-
W26030	1.51 ± 0.35	2.07 ± 0.03	412.8 ± 1.3	17 ± 5 [a]
W26090		4.96 ± 0.28	418.9 ± 0.9	
W26150	3.91	6.00 ± 0.05	420.0 ± 0.5	20 ± 7 [a]
W35030	3.13 ± 0.24	3.19 ± 0.12	413.3 ± 1.5	22 ± 6 [a]
W35090		4.33 ± 0.02	417.0 ± 2.1	
W353150	-	6.78 ± 0.03	419.0 ± 0.8	22 ± 7 [a]
E0035030	4.43 ± 0.26	6.27 ± 0.02	394.2 ± 1.5	15 ± 5
E0035150	-	12.19 ± 0.07	416.2 ± 2.3	-

[a] *Additional large fraction of particularly small (around 3 nm) silver nanoparticles was also observed, but was not included to the calculations of the average particle size.*

Moreover, supernatants were analyzed for silver as well. Large amount of residual silver found in the supernatants of the samples synthesized without using radical scavenger indicated that only small part of Ag^+ ions are reduced to form metallic silver in this case. In contrast, reaction in the presence of ethanol was more efficient with almost no residual silver being left in the supernatant after 150 min of irradiation.

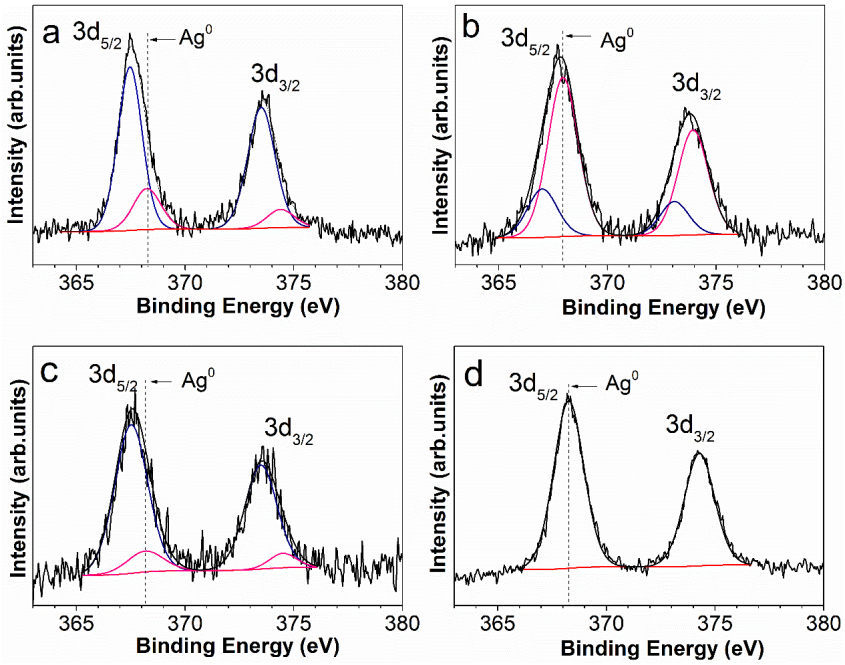

Figure 36. *Ag 3d XPS spectra of the Ag-CeO_2 nanoheterostructures: (a)– W20030; (b) – W26030; (c) – W26150 and (d) – E0035030.*

Figure 36 shows Ag 3d XPS spectra, in which silver displayed two peaks of Ag $3d_{5/2}$ and Ag $3d_{3/2}$ at around 368.0 and 374.0 eV, respectively. Ag $3d_{5/2}$ peak is reported to center at around 368.2 eV for metallic silver (from 367.9 to 368.4 eV), negative shift is attributed to the ionic Ag-O bonds with the peak centered around 367.8 eV (from 367.6 to 368.1 eV) for oxidized form of silver (Ag^+) [213-216].

As expected, lower amount of silver precursor and no radical scavenger being used resulted in a significantly oxidized final product: large peak referring to the oxidized silver at 367.7 eV was detected in the silver 3d signal together with a weak Ag^0 peak at 368.2 eV when 2.0 mmol/L $AgNO_3$ containing solution was irradiated for 30 min. Slightly higher amount of silver precursor (2.6 mmol/L) and the same irradiation time resulted in the decreased amount of oxidized silver (*Figure 36*, b). However, prolonged irradiation is responsible for the strong oxidation processes occurring in this Ag-CeO_2 system as well. Sample, containing 2.6 mmol/L $AgNO_3$ and irradiated for 150 min demonstrates intense Ag $3d_{5/2}$ peak at 367.4 eV (*Figure 36*, c). In contrast, synthesis in the ethanol containing solution resulted in formation of

pure metallic silver: peak at 368.3 eV (*Figure 36*, d) can be clearly attributed to Ag^0. XPS results are in good agreement with the data derived from UV-VIS absorption measurements and confirm that oxidative processes are occurring in the material under UV irradiation when the process is carried out in the aqueous solution.

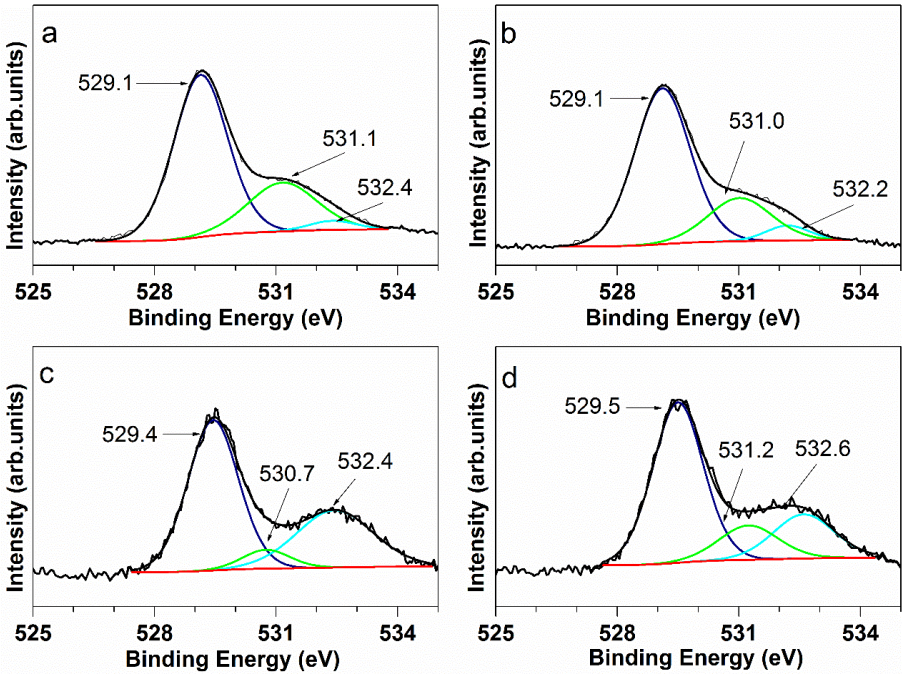

Figure 37. *O1s XPS of the Ag-CeO_2 nanoheterostructures: (a) – W20030; (b) – W26030; (c) – W26150 and (d) – E0035030.*

Unfortunately, it was nearly impossible to interpret Os1 spectra (*Figure 37*) adequately because of several significant overlaps. The peak centered at 529.1 – 529.5 eV could be ascribed both to the lattice oxygen of CeO_2 [217] and Ag_2O [218], making it particularly difficult to confirm data revealed by Ag 3d spectra. A broad asymmetric peak at higher binding energy centered at around 531 eV might also contain contributions from several different oxygen-containing species: surface carbonates (~530.8 eV), non-stoichiometric oxide phases (~530.5), chemisorbed and dissolved oxygen species (~532.0 eV), hydroxyl species (~531.7 eV) and chemisorbed H_2O (~533.0 eV) [218]. Thus, O 1s spectra neither confirmed nor denied the before raised assumption that nanoheterostructures irradiated for long time contain some oxidized silver.

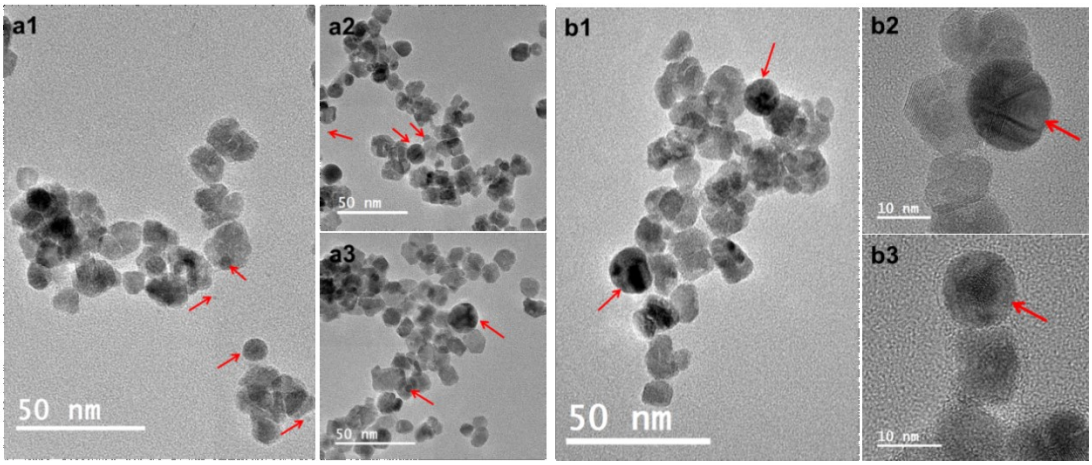

Figure 38. *TEM images of Ag-CeO_2 samples: (a) – W35030; (b) – E0035030. Some Ag NPs are indicated with the red arrows.*

Figure 38 and *Figure 39* show TEM images of fresh Ag-CeO_2 samples obtained under different synthesis conditions. It is obvious that after Ag loading both size and shape of CeO_2 crystallites remains unchanged, as shown in *Figure 30*. In addition to polyhedral ceria NPs, a significant fraction of spherical particles of different sizes was observed in the samples potentially containing silver. It should be pointed out that the low contrast and the overlap in the particle size of the two materials make it difficult to detect all Ag nanoparticles and aggregates. However, spherical shape and twinning defects, not exhibited by ceria sample and therefore attributed to Ag, facilitated the task to distinguish the two materials. Irreversible and energetically favorable twinning of Ag nanoparticles at small sizes has been previously reported in the literature [219, 220]. It is worth to note that twinned silver nanoparticles rather than the single-crystal NPs were formed in our experiment. It is reported that such defect-containing nanoparticles contain high energy sites for atomic addition and thus demonstrate relatively higher reactivity if compared to the single-crystal nanoparticles [219, 221].

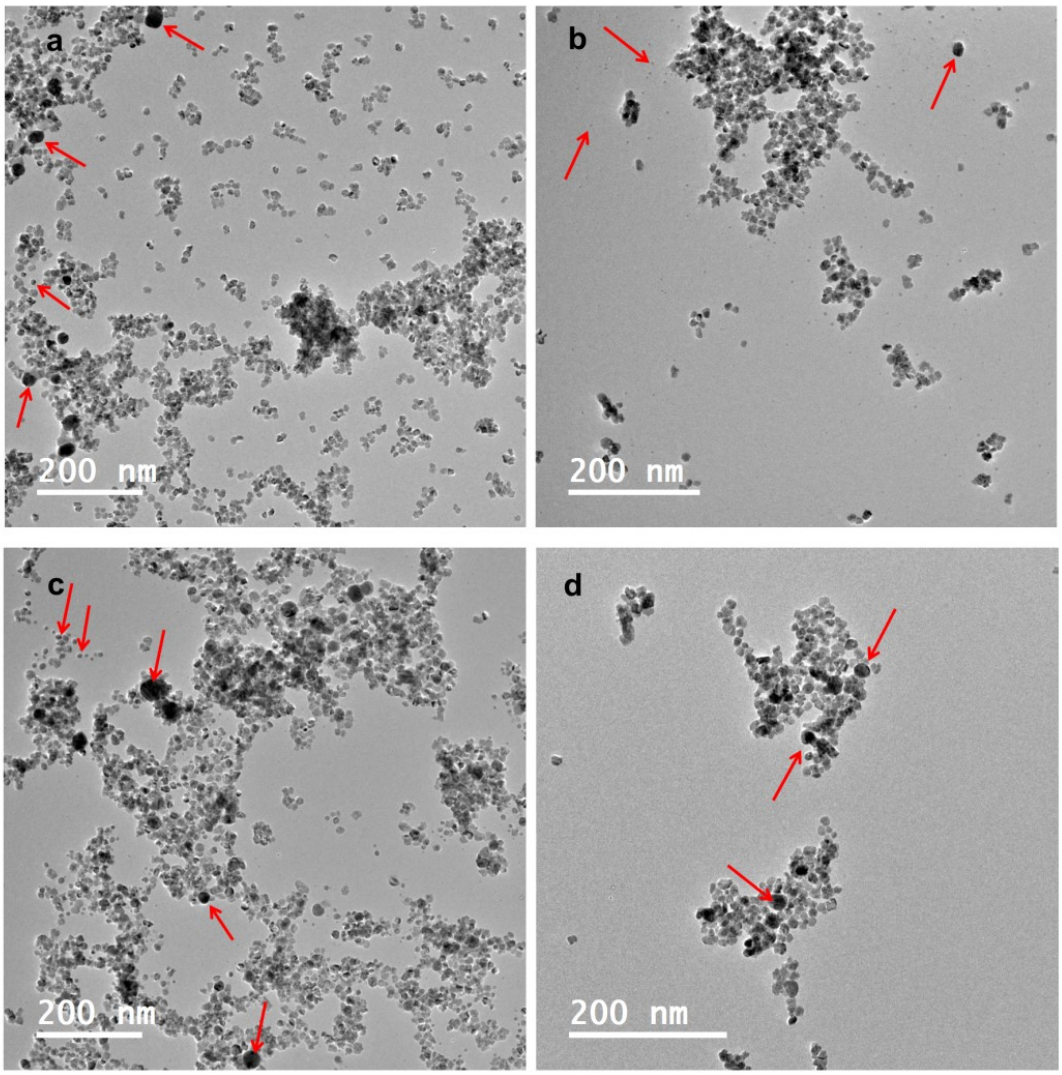

Figure 39. *TEM images of samples prepared under different synthesis conditions: a – W35030; b – W35060; c – E15030; d – E0035030. Some Ag NPs are indicated with the red arrows.*

Scanning transmission electron microscopy was applied in order to better distinguish silver NPs from ceria ones. Some representative STEM images are presented in *Figure 41*. The atomic number of Ce is 58 while for Ag it is 47. However, since CeO_2 nanoparticles are being imaged rather than pure Ce, the average atomic number of ceria is in fact lower than the one for Ag. Thus, the strong bright contrast in HAADF-STEM (so called Z-contrast) images is attributed to Ag.

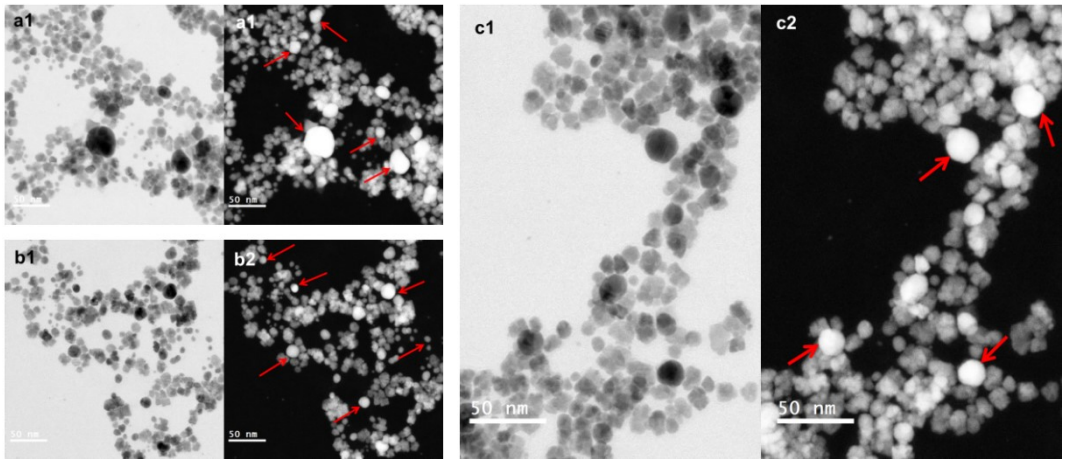

Figure 40. *BF- (a1, b1, c1) and HAADF-STEM (a2, b2, c2) images of the samples W35030. Some Ag NPs are indicated with the red arrows.*

In general, TEM images of Ag-CeO_2 samples revealed that some separate silver nanoparticles were formed after UV irradiation rather than the expected Ag-CeO_2 nanocomposites in most of the cases: even though large amount of silver nanoparticles was found to be deposited on ceria, some individual Ag NPs were spread all over the copper grid as can be seen in *Figure 39* (a) – (c) and *Figure 40*. In the case of ethanol containing solution and particularly low silver salt concentration, however, no individual silver NPs were observed (*Figure 38*, (b1)–(b3), *Figure 39* (c) and *Figure 41*), implying a stronger interaction between metal and semiconductor nanoparticles.

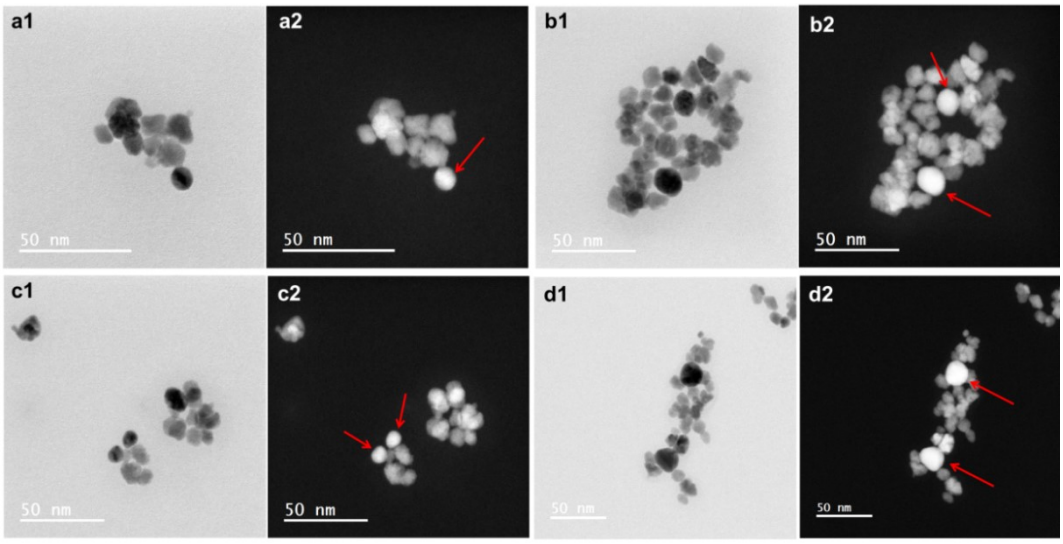

Figure 41. *BF- (a1, b1, c1 & d1) and HAADF-STEM (a2, b2, c2 & d2) images of the sample E0035030. Some Ag NPs are indicated with the red arrows.*

The synthesis with 3.5 mmol/L $AgNO_3$ without $HO^{\cdot}$ radical scavenger resulted in formation of rather large (around 22.0 nm) silver nanoparticles with a wider size distribution (*Figure 38* a1–a3, *Figure 39*a–b). Significant amount of particularly small (1.0–5.0 nm) nanoparticles was also observed in this case. This is possibly due to the high amount of silver present in the solution, suggesting also that the process is rather inhomogeneous. Some particles are only starting to form while other crystallites experience nucleation and growth. Prolonged irradiation time did not solve the problem (*Figure 39*, b). Instead, some particularly large crystals were formed after relatively long irradiation (60–150 min) together with smaller ones, and particles with the size of several nanometers were still present. This also explains the presence of quite sharp silver peaks in the XRD patterns of the samples with longer exposure time to UV light.

Reducing the amount of silver precursor and suppressing oxidation processes occurring in the system under UV irradiation was seen as a possible pathway to resolve such problems as insufficient efficiency of the reaction and inhomogeneity of the final products. As mentioned earlier, adding ethanol as a radical scavenger to the reaction solution increased the efficiency of the process significantly. Irradiation of 1.5 mmol/L $AgNO_3$ ethanolic solution resulted in formation of a high silver loading content in the final product with a wide particle size distribution (*Figure 39*, c). Further decrease in the initial silver salt concentration caused formation of more uniform silver nanoparticles with a size comparable to that of ceria nanoparticles (around 15 nm) as shown in *Figure 38*, *Figure 39*, d; and *Figure 41*. Moreover, there were no signs of particularly small Ag NPs, nor were observed large silver nanoparticles, formed separately from ceria, which were present in the samples with higher silver concentration.

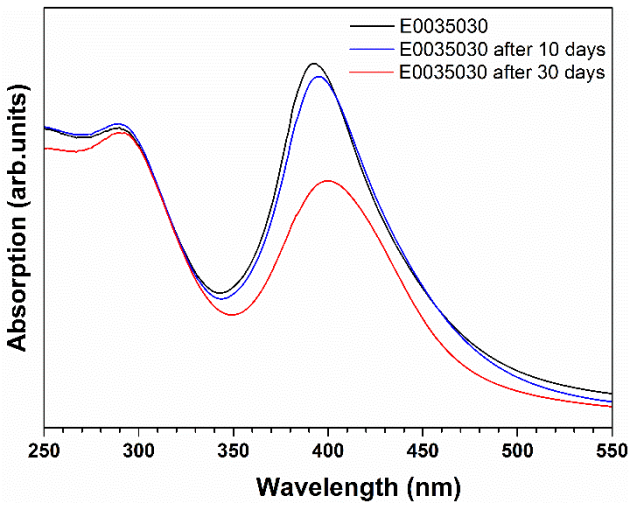

Figure 42. *Absorption spectra of freshly prepared and kept for some time in the dark Ag-CeO_2 nanoheterostructures.*

Stability of the Ag-CeO_2 nanoheterostructures was checked using UV-VIS

Figure 42). The colloidal solution of E0035030 was still stable after keeping it in the dark for 10 days: only a small bathochromic shift together with a minor intensity loss of the SPR band peak was observed in the absorption spectra in this case. Even though the colloidal solution seemed to remain unchanged after 30 days, its absorption spectra revealed that the intensity of the SPR peak was broadened and significantly decreased, a red shift of around 7 nm was also detected. This indicates that agglomeration of silver nanoparticles is unavoidable to some extent. The as-prepared silver nanoparticles are not as stable as those stabilized with citrate for example [222, 223], but the stability is still quite high considering that no stabilizing agents were used in our case.

Chapter 8. Photocatalytic properties of CeO_2 NPs and Ag-CeO_2 nanoheterostructures

Nanomaterials prepared in this study were expected to find applications in photocatalysis. It was assumed that silver would improve both UV-driven and visible-light driven photocatalysis. Therefore, photocatalytic activity tests on tributyltin degradation under visible light and UV light were performed. It was decided to study decomposition of TBT as butyltin compounds are among the most toxic anthropogenic pollutants introduced into the environment and, despite being prohibited to use in anti-fouling paints since 2008, are still found in the marine environment to a great extent [224]. In addition, more reliable results were obtained by using GC-MS for determination of butyltin species if compared to traditionally applied UV-VIS spectroscopy for determination of organic dyes (methylene blue, methyl orange, etc.) [140, 225].

8.1. Photocatalytic activity under VIS light irradiation

Investigation of photocatalytic TBT degradation by CeO_2 nanoparticles and Ag-CeO_2 nanoheterostructures was performed under artificial visible light ($\lambda = 390$ nm) irradiation. The photocatalytic efficiency was determined by calculating the relative concentration (C/C_0), where C_0 is the initial concentration of TBT and C is the concentration at the sampling time. The adsorption equilibrium has been reached after stirring the solution for 30 min in the dark, and about 5% of TBT was adsorbed onto the surface of the photocatalyst within this time. The adsorption percentage of the pollutant onto the photocatalyst refers to the ratio of the difference between the initial concentration of TBT (C_0) and its concentration at adsorption/desorption equilibrium point (C_{30} min) to the initial concentration of TBT in the solution. Thus, the concentration of TBT in bulk solution at this point was applied as the initial value for the further evaluation of the photodegradation processes.

Photocatalytic TBT degradation under visible light irradiation is presented in *Figure 43*.

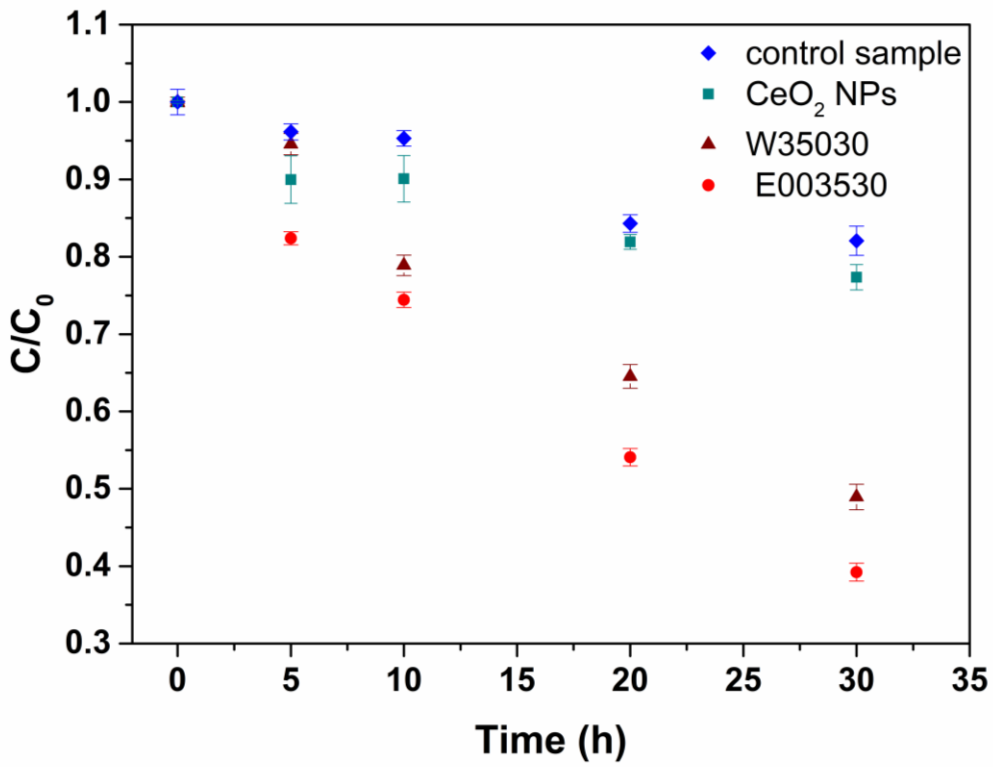

Figure 43. *Photodegradation of TBT under visible light (λ = 390 nm) irradiation at room temperature in air without adding any photocatalyst (a) and using different nanostructures: (b) – CeO_2 nanoparticles; (c) – W35030; (d) – E0035030.*

The photodegradation of tributyltin was rather slow mainly due to the low output of the light source used. However, it is clear that irradiation of the TBT working solution in the absence of photocatalyst leads to a minor decrease in TBT concentration (*Figure 43*, (a)), occurring probably due to the oxidation processes in the presence of oxygen. Irradiation of the aqueous tributyltin solution containing ceria nanoparticles gave actually quite similar results (*Figure 43*, (b)), suggesting that CeO_2 was inactive to TBT photocatalytic degradation under visible light irradiation. It is not a surprising result considering that the low energy visible light photons should not be capable of exciting CeO_2 valence electrons to its conduction band. Ag-CeO_2 nanoheterostructures, in contrast, demonstrated enhanced photocatalytic activity: more than 50% of the pollutant was degraded after 30 h exposure to

visible light when Ag-CeO_2 nanoheterostructures were applied as photocatalysts. Nanoheterostructures synthesized in ethanol containing solution showed higher activity with respect to those synthesized in pure aqueous media probably due to a higher amount of silver, thus more intense absorption at around 400 nm. TBT degradation products, DBT and MBT species, were also detected in the reaction solutions after irradiation, the concentration of the latter compounds was gradually increasing with the increasing irradiation time.

The SPR-induced charge transfer mechanism is not clearly understood yet, although direct electron transfer (DET) mechanism for the SPR-induced charge transfer has been suggested by many authors and is generally believed to be the most reliable [8, 147, 148]. According to this mechanism, direct contact between metal-semiconductor surfaces is essential. It is only possible for electrons or holes to be transferred from the metal into the semiconductor at energies below the band gap if the electronic energy levels match as DET depends strongly on the alignment of the band levels of the semiconductor and Fermi level of the plasmonic metal [24]. Before the contact with silver NPs, the conduction band of CeO_2 NPs is E^0_{CB} = -0.69 eV and the work function of Ag is around 4.7 eV [90]. After the contact between semiconductor and silver is established, the electrons and holes flow and build up a new equilibrium state, in which semiconductor Fermi level and metal work function are equilibrated as can be seen from *Figure 14*. In order to inject the electrons to the conduction band of ceria, the photon energy does not need to match the bandgap of the semiconductor. It should only satisfy this condition [90]: $h\nu \geq E_{CB0} - E_F$

No matter what the actual position of the Fermi level after the contact is, the gap of the conduction-band top and the Fermi level remains as (−4.5 + 0.69) + 4.7 = 0.89 eV (here: -4.5 is the absolute hydrogen electrode potential, -0.69 is the conduction band potential and 4.7 is the work function of Ag). In our case, the plasmon absorption energy is around 3 eV (~400 nm). Thus, many electrons should have sufficient energy to flow to the CB of ceria.

The feasibility of this mechanism could only be brought into question by the fact that it is still unrevealed whether ceria and silver are in a direct contact. However, there is a possibility that Ag-CeO_2 nanocomposites are forming while using a particularly low silver precursor concentration and ethanol since all of the Ag NPs detected in the as-prepared samples were found to be in the vicinity of ceria agglomerates.

Yet, DET is not the only mechanism proposed. It was demonstrated lately in several experiments that the photocatalytic properties of semiconductor nanostructures were still enhanced after adding an insulating interlayer between the metal and the semiconductor, thus preventing the DET. Hence, it was proposed that the SPR-mediated local electromagnetic field (LEMF) is radiatively contributing to the local generation of electron−hole pairs in the semiconductor [146, 151, 152]. Moreover, a resonant energy transfer (RET) process was introduced by Cushing *et al*. as one more possible option for the electromagnetic field mediated plasmonic energy transfer. In the plasmon-induced RET process, electron−hole pairs in the semiconductor would be excited directly in a non-radiative way through the relaxation of the localized surface plasmon dipole [24]. Most likely, combination of several charge transfer mechanisms occurs in our system. In any case, it is obvious that photocatalytic activity of CeO_2 is remarkably enhanced in the presence of silver under visible light irradiation. The results obtained confirm that silver nanoparticles extend the absorption of CeO_2 to the visible light region.

8.2. Photocatalytic activity under UV light irradiation

The UV light driven photocatalytic activity of the synthesized structures was checked upon degradation of TBT as well. To this end, three UV lamps with a total output of 5 W were applied as irradiation source. Except for the different light source used, the process was identical to the photocatalytic activity test described in Section 8.1. Similarly, the relative concentration (C/C_0) was applied to describe the photocatalytic efficiency and TBT concentration at adsorption/desorption equilibrium point (C_{30} min) was used as the initial TBT value. The results are presented in *Figure 44*.

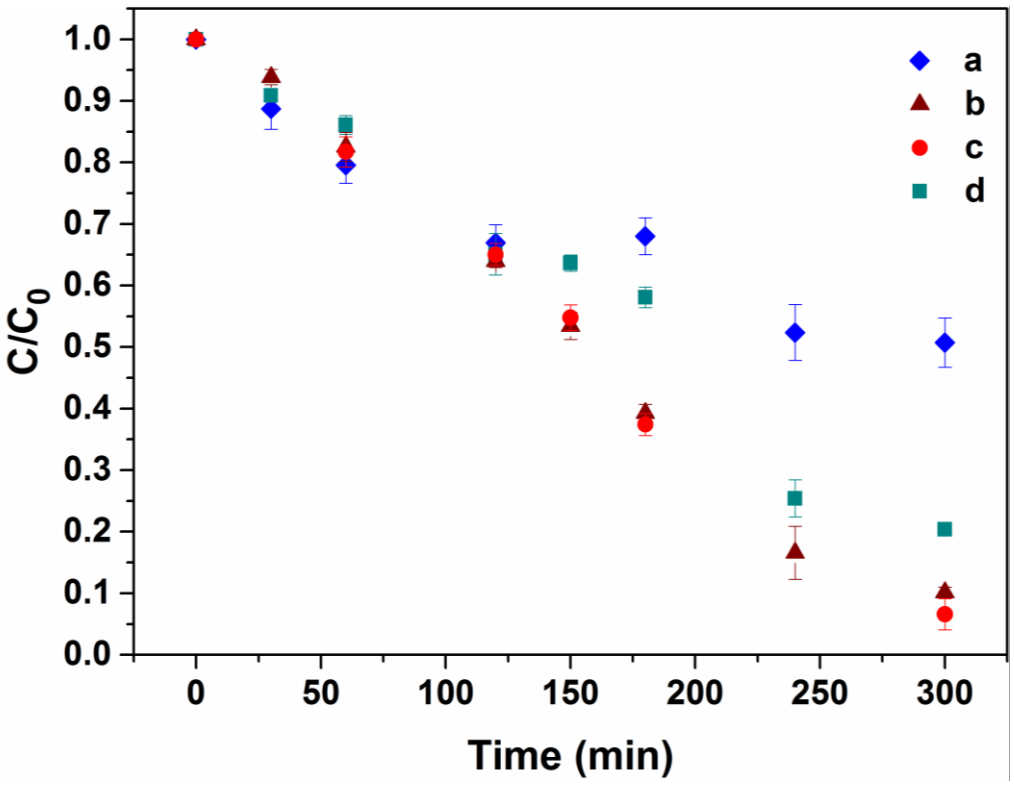

Figure 44. *Photodegradation of TBT under UV light (λ = 254 nm) irradiation at room temperature in air without adding any photocatalyst (a) and using different nanostructures: (b) – CeO_2 nanoparticles; (c) – W35030; (d) – E0035030.*

Effectiveness of UV irradiation for TBT removal was observed as early as in 1987 by Duhamel *et al.* [226], and it is well-known that photooxidation together with bioremediation are the main processes responsible for TBT

dealkylation in the natural environment [227]. Considering that, it is needless to say that the rate of TBT decomposition is significantly higher in the case of UV induced process if compared to that mediated by visible light. Even if no nanostructures were introduced to the system, TBT degradation reached almost 50% after 5 h of exposure to UV light (*Figure 44*, a). The process was even more efficient if ceria NPs were applied as photocatalyst: around 80% of the pollutant was decomposed after 5 h of irradiation in this case (*Figure 44*, b).

It is reported that plasmonic nanoparticles should enhance UV absorption of the large-bandgap materials and therefore improve not only the visible light, but also UV driven photocatalytic activity [90]. Ag nanoparticles which are in contact with ceria should also favor the photocatalytic activity by suppressing the electron–hole recombination as mentioned in Section 4.3. Indeed, evidences of improved photocatalytic activity of Ag-CeO_2 nanoheterostructures with regard to pure ceria NPs were observed in our study. The improvement in photocatalytic activity was not as high as in visible light driven photocatalysis, however: samples containing silver exhibited almost 10% higher photocatalytic activity than ceria NPs (*Figure 44*, c-d).

It would be difficult to compare the photocatalytic activity results with those obtained in the previous studies as many factors might influence the photocatalytic performance and experiments are carried out under different conditions by every group. Moreover, even though tributyltin is considered as one of the most dangerous pollutants ever released [228] and is still detected to a great extent in the aquatic environment [224], the amount of studies on photocatalytic degradation of TBT is rather limited [229, 230]. In our photocatalytic activity experiments, irradiation sources of particularly low output were used and, taking this into account, the results seem promising, to say the least.

Chapter 9. Conclusions

1) CeO_2 nanoparticles with a uniform size distribution were prepared via inorganic photochemical approach employing sodium azide as a photoactive material.
2) Radiation exposure, surfactant concentration and post-synthetic heat-treatment temperature were the main factors affecting formation and final properties of ceria nanoparticles obtained. Synthesis attempts performed without any surfactants resulted in agglomerated particles with a crystallite size ranging from 6.4 to 9.2 nm, while adding PVP to the primary solution decreased the agglomeration ratio and caused formation of slightly smaller particles (3.3–7.0 nm). Calcination of the synthesized nanoparticles was responsible for the phenomenon of sintering occurring in the material.
3) The as-prepared ceria nanoparticles were applied as a photoactive material for the photochemical synthesis of Ag-CeO_2 nanoheterostructures. Following irradiation of CeO_2 colloids in the presence of Ag^+ cations, reduction of the latter occurred to form metallic silver and Ag-CeO_2 nanoheterostructures were formed. No organic solvents or additives were applied in order to obtain particles with an uncoated, thus more reactive surface.
4) It was observed that the silver nanoparticle formation process is not efficient in pure aqueous solutions due to intensive oxidation processes. The efficiency was significantly improved by introducing ethanol as a radical/hole scavenging agent to the reaction solution. The desired monodisperse particle size distribution of silver nanoparticles was achieved under optimized synthesis conditions (0.035 mmol/L $AgNO_3$, irradiated for 30 min in ethanol (20% v/v.) solution).
5) Silver nanoparticle size, shape and oxidation state depend on concentration of the silver precursor, irradiation time and the presence of radical/hole scavenger. Rather uniform non-oxidized Ag nanoparticles with the size comparable to that of ceria NPs were

obtained using particularly low silver precursor concentration (0.035 mmol/L $AgNO_3$) in the ethanol solution. Increasing silver salt concentration resulted in a wider particle size distribution. Synthesis in pure aqueous solution was responsible for the formation of polydisperse Ag nanoparticles with the irradiation time dependent oxidation ratio: the longer the exposure to UV light was, the higher fraction of the final product was oxidized.

6) CeO_2 nanostructures were determined to be inactive under VIS light, but demonstrated some UV-light driven photocatalytic activity. However, Ag-CeO_2 nanoheterostructures showed significantly enhanced photocatalytic activity both under visible and UV-light irradiation if compared to pure ceria NPs.

Chapter 10. List of publications and conference participation

10.1. Publications included in the thesis

10.1.1. Journal articles

1. **E. Raudonyte-Svirbutaviciene**, L. Mikoliunaite, A. Drabavicius, R. Juskenas, S. Sakirzanovas, T. Jüstel, A. Katelnikovas. "Photochemical synthesis of CeO_2 nanoscale particles using sodium azide as a photoactive material: effects of the annealing temperature and polyvinylpyrrolidone addition". RSC Advances **6** (2016) 107065
2. **E. Raudonyte-Svirbutaviciene**, A. Neagu, V. Vickackaite, V. Jasulaitiene, A. Zarkov, C.W. Tai, A. Katelnikovas. "Two-step photochemical inorganic approach to the synthesis of Ag-CeO_2 nanoheterostructures and their photocatalytic activity on tributyltin degradation". Journal of Photochemistry and Photobiology A: Chemistry **351** (2018) 29

10.1.2. Attended Conferences

1. **E. Raudonytė – Svirbutavičienė**, T. Jüstel, A. Katelnikovas. "Photochemical synthesis of CeO_2 nanoparticles". *41th National Lithuanian Physics Conference*. Vilnius, Lithuania, June 17 – 19 (2015) 216
2. **E. Raudonytė-Svirbutavičienė**, A. Katelnikovas. Photochemical Synthesis of CeO_2-Ag Nanocomposites. *17th International Conference-School Advanced Materials and Technologies.* Palanga, Lithuania, August 27 – 31 (2015)
3. **E. Raudonytė-Svirbutavičienė**, T. Jüstel, A. Katelnikovas. "Photochemical synthesis of CeO_2 nanoparticles". *Nano-chemistry and nanomaterials*. 2nd *International Conference of Chemists* Vilnius, Lithuania, October 22–25 (2015) 45

4. **E. Raudonytė-Svirbutavičienė**, A. Drabavičius, A. Katelnikovas. "Photochemical approach to the inorganic synthesis of semiconductor nanoparticles." *Chemistry and chemical technology. International conference of Lithuanian Society of Chemistry*. Vilnius, Lithuania, April 28-29 (2016) 144
5. **E. Raudonytė-Svirbutavičienė**, A. Drabavičius, A. Katelnikovas. "Photochemical approach to the inorganic synthesis of PVP coated semiconductor nanoparticles". *Functional hybrid materials: structure elucidation from molecular to macroscopic level. A workshop/conference and training school.* Stockholm, Sweden, May 25 – 27 (2016) 37
6. **E. Raudonytė-Svirbutavičienė**, V. Vičkačkaitė, A. Žarkov, A. Katelnikovas. "Clean photochemical synthesis of semiconductor-silver nanocomposites and their photocatalytic performance for tributyltin degradation". *2nd International Conference on Green Chemistry and Sustainable Engineering*, Rome, Italy, July 20-22 (2016) 83-84
7. **E. Raudonytė-Svirbutavičienė**, C.W. Tai, A. Neagu, A. Katelnikovas. "Light driven synthesis of nanostructures". *Open Readings 2017. 60th International conference for students of physics and natural sciences.* Vilnius, Lithuania, March 14-17 (2017) 163
8. **E. Raudonytė-Svirbutavičienė**, A. Katelnikovas. "UV Light driven synthesis of plasmonic nanoparticles on ceria support: optimisation and potential applications in photocatalysis". *2nd international Conference Nanophotonics and Micro/Nano Optics*. Barcelona, Spain, September 13 – 15 (2017) 217-218

10.2. Publications Not Included in the Thesis

10.2.1. Journal articles

1. **E. Raudonytė-Svirbutavičienė**, H. Bettentrup, D. Uhlich, S. Šakirzanovas, O. Opuchovič, S. Tautkus, A. Katelnikovas. "On the $Ce^{3+} \rightarrow Cr^{3+}$ energy transfer in $Lu_3Al_5O_{12}$ garnets". Optical Materials **37** (2014) 204 – 210
2. R. Stakėnienė, K. Jokšas, A. Galkus, **E. Raudonytė-Svirbutavičienė**. "Aliphatic and polycyclic aromatic hydrocarbons in the bottom sediments from Klaipėda Harbour, Lithuania (Baltic Sea)". Chemistry and Ecology **32** (2016) 357 – 377
3. I. Mikalauskaitė, **E. Raudonytė-Svirbutavičienė**, A. Linkevičiūtė, M. Urbonas, A. Katelnikovas. "Luminescence and luminescence quenching of $Sr_3Lu_2(Si_3O_9)_2:Ce^{3+}$ phosphors". Journal of Luminescence 184 (2017) 185 – 190

References

[1] M.A. Fox, M.T. Dulay, Heterogeneous Photocatalysis, Chem. Rev., 93 (1993) 341-357.
[2] A. Kudo, Y. Miseki, Heterogeneous Photocatalyst Materials for Water Splitting, Chem. Soc. Rev., 38 (2009) 253-278.
[3] W.H. Brattain, C.G.B. Garrett, Experiments on the Interface between Germanium and an Electrolyte, Bell System Technical Journal, 34 (1955) 129-176.
[4] A. Fujishima, K. Honda, Electrochemical Photolysis of Water at a Semiconductor Electrode, Nature, 238 (1972) 37-38.
[5] A. Fujishima, K. Honda, Electrochemical Evidence for the Mechanism of the Primary Stage of Photosynthesis, Bull Chem Soc Japan, 44 (1971) 1148-1150.
[6] A.J. Nozik, Photoelectrochemical Devices for Solar Energy Conversion, in: F. Cardon, W.P. Gomes, W. Dekeyser (Eds.) Photovoltaic and Photoelectrochemical Solar Energy Conversion, Springer US, Boston, MA, 1981, pp. 263-312.
[7] S. Linic, P. Christopher, D.B. Ingram, Plasmonic-metal Nanostructures for Efficient Conversion of Solar to Chemical Energy, Nat. Mater., 10 (2011) 911-921.
[8] S. Mubeen, G. Hernandez-Sosa, D. Moses, J. Lee, M. Moskovits, Plasmonic Photosensitization of a wide Band gap Semiconductor: Converting Plasmons to Charge Carriers, Nano Lett., 11 (2011) 5548-5552.
[9] C. Chen, W. Ma, J. Zhao, Semiconductor-mediated Photodegradation of Pollutants under Visible-light Irradiation, Chem. Soc. Rev., 39 (2010) 4206-4219.
[10] S. Sarina, E.R. Waclawik, H. Zhu, Photocatalysis on Supported Gold and Silver Nanoparticles under Ultraviolet and Visible Light Irradiation, Green Chem., 15 (2013) 1814-1833.
[11] S.T. Kochuveedu, Y.H. Jang, D.H. Kim, A Study on the Mechanism for theIinteraction ofLight with Noble Metal-metal OxideSsemiconductor Nanostructures for Various Photophysical Applications, Chem. Soc. Rev., 42 (2013) 8467-8493.
[12] V. Aruoja, H.-C. Dubourguier, K. Kasemets, A. Kahru, Toxicity of Nanoparticles of CuO, ZnO and TiO2 to Microalgae Pseudokirchneriella Subcapitata, Sci. Total Environ., 407 (2009) 1461-1468.
[13] R.K. Shukla, A. Kumar, D. Gurbani, A.K. Pandey, S. Singh, A. Dhawan, TiO2 Nanoparticles Induce Oxidative DNA Damage and Apoptosis in Human Liver Cells, Nanotoxicology, 7 (2013) 48-60.
[14] P.O. Andersson, C. Lejon, B. Ekstrand-Hammarström, C. Akfur, L. Ahlinder, A. Bucht, L. Österlund, Polymorph- and Size-Dependent Uptake and Toxicity of TiO_2 Nanoparticles in Living Lung Epithelial Cells, Small, 7 (2011) 514-523.
[15] R.J. Miller, H.S. Lenihan, E.B. Muller, N. Tseng, S.K. Hanna, A.A. Keller, Impacts of Metal Oxide Nanoparticles on Marine Phytoplankton, Environ. Sci. Techn., 44 (2010) 7329-7334.
[16] S. Bandyopadhyay, J.R. Peralta-Videa, G. Plascencia-Villa, M. José-Yacamán, J.L. Gardea-Torresdey, Comparative Toxicity Assessment of CeO2 and ZnO Nanoparticles towards Sinorhizobium Meliloti, a Symbiotic Alfa associated Bacterium: Use of Advanced Microscopic and Spectroscopic Techniques, J. Hazard. Mater., 241–242 (2012) 379-386.
[17] T. Xia, M. Kovochich, M. Liong, L. Mädler, B. Gilbert, H. Shi, J.I. Yeh, J.I. Zink, A.E. Nel, Comparison of the Mechanism of Toxicity of Zinc Oxide and Cerium

Oxide Nanoparticles Based on Dissolution and Oxidative Stress Properties, ACS Nano, 2 (2008) 2121-2134.
[18] C. Sun, H. Li, L. Chen, Nanostructured Ceria-based Materials: Synthesis, Properties, and Applications, Energy Environ. Sci., 5 (2012) 8475-8505.
[19] S.P.S. Badwal, D. Fini, F.T. Ciacchi, C. Munnings, J.A. Kimpton, J. Drennan, Structural and Microstructural Stability of Ceria - Gadolinia Electrolyte Exposed to Reducing Environments of High Temperature Fuel Cells, J. Mater. Chem. A, 1 (2013) 10768-10782.
[20] J. Hou, L. Bi, J. Qian, Z. Zhu, J. Zhang, W. Liu, High Performance Ceria-Bismuth Bilayer Electrolyte Low Temperature Solid Oxide Fuel Cells (LT-SOFCs) Fabricated by Combining Co-pressing with Drop-coating, J. Mater. Chem. A, 3 (2015) 10219-10224.
[21] A. Younis, D. Chu, Y.V. Kaneti, S. Li, Tuning the Surface Oxygen Concentration of {111} Surrounded Ceria Nanocrystals for Enhanced Photocatalytic Activities, Nanoscale, 8 (2016) 378-387.
[22] S. Imamura, H. Yamada, K. Utani, Combustion Activity of Ag/CeO_2 Composite Catalyst, Appl. Catal. A, 192 (2000) 221-226.
[23] J. Tian, Z. Zhao, A. Kumar, R.I. Boughton, H. Liu, Recent Progress in Design, Synthesis, and Applications of one-dimensional TiO_2 Nanostructured Surface Heterostructures: a Review, Chem. Soc. Rev., 43 (2014) 6920-6937.
[24] S.K. Cushing, J. Li, F. Meng, T.R. Senty, S. Suri, M. Zhi, M. Li, A.D. Bristow, N. Wu, Photocatalytic Activity Enhanced by Plasmonic Resonant Energy Transfer from Metal to Semiconductor, J. Am. Chem. Soc., 134 (2012) 15033-15041.
[25] K. Awazu, M. Fujimaki, C. Rockstuhl, J. Tominaga, H. Murakami, Y. Ohki, N. Yoshida, T. Watanabe, A Plasmonic Photocatalyst Consisting of Silver Nanoparticles Embedded in Titanium Dioxide, J. Am. Chem. Soc., 130 (2008) 1676-1680.
[26] Q. Zhang, D.Q. Lima, I. Lee, F. Zaera, M. Chi, Y. Yin, A Highly Active Titanium Dioxide Based Visible-Light Photocatalyst with Nonmetal Doping and Plasmonic Metal Decoration, Angew. Chem., 123 (2011) 7226-7230.
[27] N. Krishnamurthy, C.K. Gupta, Extractive Metallurgy of Rare Earths, CRC Press, 2004.
[28] N.V. Skorodumova, S.I. Simak, B.I. Lundqvist, I.A. Abrikosov, B. Johansson, Quantum Origin of the Oxygen Storage Capability of Ceria, Phys. Rev. Lett., 89 (2002) 166601.
[29] H. Li, G. Wang, F. Zhang, Y. Cai, Y. Wang, I. Djerdj, Surfactant-assisted Synthesis of CeO2 Nanoparticles and their Application in Wastewater Treatment, RSC Adv., 2 (2012) 12413-12423.
[30] L. Tye, N.A. El-Masry, T. Chikyow, P. McLarty, S.M. Bedair, Electrical Characteristics of Epitaxial CeO2 on Si(111), App. Phys. Lett., 65 (1994) 3081-3083.
[31] M. Aguirre, M. Paulis, J.R. Leiza, UV Screening Clear Coats Based on Encapsulated CeO2 Hybrid Latexes, J Mater. Chem. A, 1 (2013) 3155-3162.
[32] W. Duan, A. Xie, Y. Shen, X. Wang, F. Wang, Y. Zhang, J. Li, Fabrication of Superhydrophobic Cotton Fabrics with UV Protection Based on CeO2 Particles, Industr. & Engin. Chem. Res., 50 (2011) 4441-4445.
[33] D.R. Lide, CRC Handbook of chemistry and physics, CRC Press, Boca Raton, Fla. [u.a.], 2006.
[34] Y. Li, Q. Sun, M. Kong, W. Shi, J. Huang, J. Tang, X. Zhao, Coupling Oxygen Ion Conduction to Photocatalysis in Mesoporous Nanorod-like Ceria Significantly Improves Photocatalytic Efficiency, J. Phys. Chem. C, 115 (2011) 14050-14057.

[35] B. Murugan, A.V. Ramaswamy, Defect-Site Promoted Surface Reorganization in Nanocrystalline Ceria for the Low-Temperature Activation of Ethylbenzene, J. Am. Chem. Soc., 129 (2007) 3062-3063.
[36] C. Sicard, M. Perullini, C. Spedalieri, T. Coradin, R. Brayner, J. Livage, M. Jobbágy, S.A. Bilmes, CeO2 Nanoparticles for the Protection of Photosynthetic Organisms Immobilized in Silica Gels, Chem. Mater., 23 (2011) 1374-1378.
[37] O. Parlak, M.M. Demir, Toward Transparent Nanocomposites Based on Polystyrene Matrix and PMMA-Grafted CeO2 Nanoparticles, ACS Appl.Mater.Interfaces, 3 (2011) 4306-4314.
[38] S.B. Khan, M. Faisal, M.M. Rahman, A. Jamal, Exploration of CeO2 Nanoparticles as a Chemi-sensor and Photo-catalyst for Environmental Applications, Sci. Total Environ., 409 (2011) 2987-2992.
[39] X. Guo, R. Waser, Electrical Properties of the Grain boundaries of Oxygen Ion Conductors: Acceptor-doped Zirconia and Ceria, Progr. in Mater. Sci., 51 (2006) 151-210.
[40] V. Esposito, E. Traversa, Design of Electroceramics for Solid Oxides Fuel Cell Applications: Playing with Ceria, J. Am. Ceram. Soc., 91 (2008) 1037-1051.
[41] E.P. Murray, T. Tsai, S.A. Barnett, A direct-methane Fuel Cell with a Ceria-based Anode, Nature, 400 (1999) 649-651.
[42] S. Nakatsuji, K. Kuga, Y. Machida, T. Tayama, T. Sakakibara, Y. Karaki, H. Ishimoto, S. Yonezawa, Y. Maeno, E. Pearson, G.G. Lonzarich, L. Balicas, H. Lee, Z. Fisk, Superconductivity and Quantum Criticality in the Heavy-Fermion System [beta]-$YbAlB_4$, Nat Phys, 4 (2008) 603-607.
[43] N. Tsujii, H. Kontani, K. Yoshimura, Universality in Heavy Fermion Systems with General Degeneracy, Phys. Rev. Lett., 94 (2005) 057201.
[44] A. Barla, J. Derr, J.P. Sanchez, B. Salce, G. Lapertot, B.P. Doyle, R. Rüffer, R. Lengsdorf, M.M. Abd-Elmeguid, J. Flouquet, High-Pressure Ground State of SmB_6 : Electronic Conduction and Long Range Magnetic Order, Phys. Rev. Lett., 94 (2005) 166401.
[45] T. Park, V.A. Sidorov, F. Ronning, J.X. Zhu, Y. Tokiwa, H. Lee, E.D. Bauer, R. Movshovich, J.L. Sarrao, J.D. Thompson, Isotropic Quantum Scattering and Unconventional Superconductivity, Nature, 456 (2008) 366-368.
[46] E.M. Motoyama, G. Yu, I.M. Vishik, O.P. Vajk, P.K. Mang, M. Greven, Spin Correlations in the Electron-doped High-transition-temperature Superconductor Nd_2-xCexCuO$_4$, Nature, 445 (2007) 186-189.
[47] J. Yoshida, S. Abe, D. Takahashi, Y. Segawa, Y. Komai, H. Tsujii, K. Matsumoto, H. Suzuki, Y. Ōnuki, Novel Quantum Criticality in $CeRu_2Si_2$ near Absolute Zero Observed by Thermal Expansion and Magnetostriction, Phys. Rev. Lett., 101 (2008) 256402.
[48] J.P. Rueff, J.P. Itié, M. Taguchi, C.F. Hague, J.M. Mariot, R. Delaunay, J.P. Kappler, N. Jaouen, Probing the γ−α Transition in Bulk Ce under Pressure: A Direct Investigation by Resonant Inelastic X-Ray Scattering, Phys. Rev. Lett., 96 (2006) 237403.
[49] P. Gao, Z. Kang, W. Fu, W. Wang, X. Bai, E. Wang, Electrically Driven Redox Process in Cerium Oxides, J. Am. Chem. Soc., 132 (2010) 4197-4201.
[50] A. Pfau, K.D. Schierbaum, The electronic structure of stoichiometric and reduced CeO2 surfaces: an XPS, UPS and HREELS study, Surface Science, 321 (1994) 71-80.
[51] M. Coey, K. Ackland, M. Venkatesan, S. Sen, Collective magnetic response of CeO_2 nanoparticles, Nat Phys, advance online publication (2016).

[52] R. Gillen, S.J. Clark, J. Robertson, Nature of the Electronic Band gap in Lanthanide Oxides, Phys.Rev. B, 87 (2013) 125116.
[53] J.-D. Cafun, K.O. Kvashnina, E. Casals, V.F. Puntes, P. Glatzel, Absence of Ce3+ Sites in Chemically Active Colloidal Ceria Nanoparticles, ACS Nano, 7 (2013) 10726-10732.
[54] F. Goubin, X. Rocquefelte, M.-H. Whangbo, Y. Montardi, R. Brec, S. Jobic, Experimental and Theoretical Characterization of the Optical Properties of CeO_2, $SrCeO_3$, and Sr_2CeO_4 Containing Ce^{4+} (f0) Ions, Chem. Mater., 16 (2004) 662-669.
[55] E. Wuilloud, B. Delley, W.D. Schneider, Y. Baer, Spectroscopic Evidence for Localized and Extended f-Symmetry States in CeO_2, Phys. Rev. Lett., 53 (1984) 202-205.
[56] N.K. Renuka, N. Harsha, T. Divya, Supercharged Ceria Quantum Dots with Exceptionally high Oxygen Buffer Action, RSC Adv., 5 (2015) 38837-38841.
[57] M. Mogensen, N.M. Sammes, G.A. Tompsett, Physical, Chemical and Electrochemical Properties of Pure and Doped Ceria, Solid State Ionics, 129 (2000) 63-94.
[58] Z. Wang, Z.C. Kang, Functional and Smart Materials: Structural Evolution and Structure Analysis, Springer US, 1998.
[59] J.M. López, A.L. Gilbank, T. García, B. Solsona, S. Agouram, L. Torrente-Murciano, The prevalence of surface oxygen vacancies over the mobility of bulk oxygen in nanostructured ceria for the total toluene oxidation, Applied Catalysis B: Environmental, 174 (2015) 403-412.
[60] C.T. Campbell, C.H.F. Peden, Oxygen Vacancies and Catalysis on Ceria Surfaces, Science, 309 (2005) 713-714.
[61] C. Zhang, A. Michaelides, D.A. King, S.J. Jenkins, Oxygen Vacancy Clusters on Ceria: Decisive Role of Cerium f Electrons, Phys. Rev. B, 79 (2009) 075433.
[62] B.W. Sheldon, V.B. Shenoy, Space Charge Induced Surface Stresses: Implications in Ceria and other Ionic Solids, Phys Rev Lett, 106 (2011) 216104.
[63] J.P. Holgado, R. Alvarez, G. Munuera, Study of CeO_2 XPS Spectra by Factor Analysis: Reduction of CeO_2, Appl. Surf. Sci., 161 (2000) 301-315.
[64] M.A. Henderson, W.S. Epling, C.L. Perkins, C.H.F. Peden, U. Diebold, Interaction of Molecular Oxygen with the Vacuum-Annealed TiO2(110) Surface: Molecular and Dissociative Channels, J. Phys. Chem. B, 103 (1999) 5328-5337.
[65] K. Michel, J.-P. Eufinger, G. Ulbrich, M. Lerch, J. Janek, M.T. Elm, Combining two Redox Active Rare Earth Elements for Oxygen Storage - Electrical Properties and Defect Chemistry of Ceria-praseodymia Single Crystals, Phys. Chem. Chem.l Phys., 19 (2017) 17661-17669.
[66] S. Carrettin, P. Concepción, A. Corma, J.M. López Nieto, V.F. Puntes, Nanocrystalline CeO_2 Increases the Activity of Au for CO Oxidation by Two Orders of Magnitude, Angew. Chem. Internat. Ed., 43 (2004) 2538-2540.
[67] J. Guzman, S. Carrettin, A. Corma, Spectroscopic Evidence for the Supply of Reactive Oxygen during CO Oxidation Catalyzed by Gold Supported on Nanocrystalline CeO_2, J. Am. Chem. Soc., 127 (2005) 3286-3287.
[68] G.N. Vayssilov, Y. Lykhach, A. Migani, T. Staudt, G.P. Petrova, N. Tsud, T. Skála, A. Bruix, F. Illas, K.C. Prince, V.r. Matolı´n, K.M. Neyman, J. Libuda, Support Nanostructure Boosts Oxygen Transfer to Catalytically Active Platinum Nanoparticles, Nat Mater, 10 (2011) 310-315.
[69] A. Migani, G.N. Vayssilov, S.T. Bromley, F. Illas, K.M. Neyman, Greatly Facilitated Oxygen Vacancy Formation in Ceria Nanocrystallites, Chem. Commun. (Camb), 46 (2010) 5936-5938.

[70] H.L. Tuller, Ionic Conduction in Nanocrystalline Materials, Solid State Ionics, 131 (2000) 143-157.
[71] F. Esch, S. Fabris, L. Zhou, T. Montini, C. Africh, P. Fornasiero, G. Comelli, R. Rosei, Electron Localization Determines Defect Formation on Ceria Substrates, Science, 309 (2005) 752-755.
[72] M.Y. Chen, X.T. Zu, X. Xiang, H.L. Zhang, Effects of Ion Irradiation and Annealing on Optical and Structural Properties of CeO2 Films on Sapphire, Physica B: Condensed Matter, 389 (2007) 263-268.
[73] M. Ratner, D. Ratner, Nanotechnology: a gentle Introduction to the Next Big Idea, Prentice Hall Press, 2002.
[74] S. Lal, S. Link, N.J. Halas, Nano-optics from Sensing to Waveguiding, Nat Photon, 1 (2007) 641-648.
[75] M. Rycenga, C.M. Cobley, J. Zeng, W. Li, C.H. Moran, Q. Zhang, D. Qin, Y. Xia, Controlling the Synthesis and Assembly of Silver Nanostructures for Plasmonic Applications, Chem. Rev., 111 (2011) 3669-3712.
[76] M. Li, S.K. Cushing, N. Wu, Plasmon-enhanced Optical Sensors: a Review, Analyst, 140 (2015) 386-406.
[77] A.W. Sanders, D.A. Routenberg, B.J. Wiley, Y. Xia, E.R. Dufresne, M.A. Reed, Observation of Plasmon Propagation, Redirection, and Fan-out in Silver Nanowires, Nano Lett, 6 (2006) 1822-1826.
[78] D.K. Gramotnev, S.I. Bozhevolnyi, Plasmonics Beyond the Diffraction Limit, Nat Photon, 4 (2010) 83-91.
[79] G. Mie, Beiträge zur Optik trüber Medien, speziell kolloidaler Metallösungen, Annalen der Physik, 330 (1908) 377-445.
[80] K. Fuku, R. Hayashi, S. Takakura, T. Kamegawa, K. Mori, H. Yamashita, The Synthesis of Size- and Color-Controlled Silver Nanoparticles by Using Microwave Heating and their Enhanced Catalytic Activity by Localized Surface Plasmon Resonance, Angew Chem Int Ed Engl, 52 (2013) 7446-7450.
[81] M.A. El-Sayed, Some Interesting Properties of Metals Confined in Time and Nanometer Space of Different Shapes, Acc. Chem. Res., 34 (2001) 257-264.
[82] K.M. Mayer, J.H. Hafner, Localized Surface Plasmon Resonance Sensors, Chem. Rev., 111 (2011) 3828-3857.
[83] S. Link, M.A. El-Sayed, Shape and size dependence of radiative, non-radiative and Photothermal Properties of Gold Nanocrystals, Intern. Rev. Phys. Chem., 19 (2000) 409-453.
[84] L. Brus, Noble Metal Nanocrystals: Plasmon Electron Transfer Photochemistry and Single-Molecule Raman Spectroscopy, Acc. Chem. Res., 41 (2008) 1742-1749.
[85] P. Mulvaney, Surface Plasmon Spectroscopy of Nanosized Metal Particles, Langmuir, 12 (1996) 788-800.
[86] K.L. Kelly, E. Coronado, L.L. Zhao, G.C. Schatz, The Optical Properties of Metal Nanoparticles: The Influence of Size, Shape, and Dielectric Environment, J. Phys. Chem. B, 107 (2003) 668-677.
[87] E.J. Zeman, G.C. Schatz, An Accurate Electromagnetic Theory Study of Surface Enhancement Factors for Silver, Gold, Copper, Lithium, Sodium, Aluminum, Gallium, Indium, Zinc, and Cadmium, J. Phys. Chem., 91 (1987) 634-643.
[88] L. Tong, Q. Wei, A. Wei, J.-X. Cheng, Gold Nanorods as Contrast Agents for Biological Imaging: Optical Properties, Surface Conjugation and Photothermal Effects†, Photochem. Photob., 85 (2009) 21-32.

[89] P.D. Nallathamby, T. Huang, X.-H.N. Xu, Design and Characterization of Optical Nano Rulers of Single Nanoparticles Using Optical Microscopy and Spectroscopy, Nanoscale, 2 (2010) 1715-1722.
[90] Z. Xuming, C. Yu Lim, L. Ru-Shi, T. Din Ping, Plasmonic Photocatalysis, Rep. Prog. Phys., 76 (2013) 046401.
[91] H. Mattoussi, J. Cheon, Inorganic Nanoprobes for Biological Sensing and Imaging, Artech House, 2009.
[92] E.C. Le Ru, P.G. Etchegoin, Chapter 3 - Introduction to plasmons and plasmonics, in: Principles of Surface-Enhanced Raman Spectroscopy, Elsevier, Amsterdam, 2009, pp. 121-183.
[93] M. Grzelczak, L.M. Liz-Marzan, The Relevance of Light in the Formation of Colloidal Metal Nanoparticles, Chem. Soc. Rev., 43 (2014) 2089-2097.
[94] M.J. Kale, T. Avanesian, P. Christopher, Direct Photocatalysis by Plasmonic Nanostructures, ACS Catal., 4 (2014) 116-128.
[95] S. Gnanam, V. Rajendran, Synthesis of CeO_2 or α–Mn_2O_3 nanoparticles via sol–gel process and their optical properties, J. Sol-Gel Sci. Technol., 58 (2010) 62-69.
[96] H. Xiao, Z. Ai, L. Zhang, Nonaqueous Sol−Gel Synthesized Hierarchical CeO_2 Nanocrystal Microspheres as Novel Adsorbents for Wastewater Treatment, J. Phys. Chem. C, 113 (2009) 16625-16630.
[97] J. Zhang, H. Yang, S. Wang, W. Liu, X. Liu, J. Guo, Y. Yang, Mesoporous CeO_2 anoparticles assembled by hollow nanostructures: formation mechanism and enhanced catalytic properties, Cryst. Eng. Comm, 16 (2014) 8777-8785.
[98] C. Zhang, X. Zhang, Y. Wang, S. Xie, Y. Liu, X. Lu, Y. Tong, Facile electrochemical synthesis of CeO_2 hierarchical nanorods and nanowires with excellent photocatalytic activities, New J. Chem., 38 (2014) 2581-2586.
[99] M. Lin, Z.Y. Fu, H.R. Tan, J.P.Y. Tan, S.C. Ng, E. Teo, Hydrothermal Synthesis of CeO_2 Nanocrystals: Ostwald Ripening or Oriented Attachment?, Crystal Growth & Design, 12 (2012) 3296-3303.
[100] N. Padmanathan, S. Selladurai, Shape Controlled Synthesis of CeO_2 Nanostructures for High Performance Supercapacitor Electrodes, RSC Adv., 4 (2014) 6527-6534.
[101] H. Wang, J.-J. Zhu, J.-M. Zhu, X.-H. Liao, S. Xu, T. Ding, H.-Y. Chen, Preparation of nanocrystalline ceria particles by sonochemical and microwave assisted heating methods, PCCP, 4 (2002) 3794-3799.
[102] D.V. Pinjari, A.B. Pandit, Room Temperature Synthesis of Crystalline CeO2 Nanopowder: Advantage of Sonochemical Method over Conventional Method, Ultrason. Sonochem., 18 (2011) 1118-1123.
[103] P. Jamshidi, M. Salavati-Niasari, D. Ghanbari, H.R. Shams, Synthesis, Characterization, Photoluminescence and Photocatalytic Properties of CeO_2 Nanoparticles by the Sonochemical Method, J. Cluster Sci., 24 (2013) 1151-1162.
[104] M. Taguchi, S. Takami, T. Adschiri, T. Nakane, K. Sato, T. Naka, Supercritical Hydrothermal Synthesis of Hydrophilic Polymer-Modified Water-dispersible CeO_2 Nanoparticles, Cryst. Eng. Comm, 13 (2011) 2841-2848.
[105] C. Slostowski, S. Marre, O. Babot, T. Toupance, C. Aymonier, CeO2 Nanocrystals from Supercritical Alcohols: New Opportunities for Versatile Functionalizations?, Langmuir, 30 (2014) 5965-5972.
[106] V. Ramamurthy, J. Sivaguru, Supramolecular Photochemistry as a Potential Synthetic Tool: Photocycloaddition, Chem Rev, 116 (2016) 9914-9993.
[107] S.F. Chen, J.P. Li, K. Qian, W.P. Xu, Y. Lu, W.X. Huang, S.H. Yu, Large Scale Photochemical Synthesis of M@TiO_2 Nanocomposites (M = Ag, Pd, Au, Pt)

and their Optical Properties, CO Oxidation Performance, and Antibacterial Effect, Nano Res., 3 (2010) 244-255.
[108] J.C. Scaiano, K.G. Stamplecoskie, G.L. Hallett-Tapley, Photochemical Norrish type I Reaction as a Tool for Metal Nanoparticle Synthesis: Importance of Proton Coupled Electron Transfer, Chem. Commun., 48 (2012) 4798-4808.
[109] T.-L. Wee, B.D. Sherman, D. Gust, A.L. Moore, T.A. Moore, Y. Liu, J.C. Scaiano, Photochemical Synthesis of a Water Oxidation Catalyst Based on Cobalt Nanostructures, J. Am. Chem. Soc., 133 (2011) 16742-16745.
[110] K.L. McGilvray, J. Granger, M. Correia, J.T. Banks, J.C. Scaiano, Opportunistic Use of Tetrachloroaurate Photolysis in the Generation of Reductive Species for the Production of Gold Nanostructures, Phys. Chem. Chem. Phys., 13 (2011) 11914-11918.
[111] D. Malyshev, F. Bosca, C.-O.L. Crites, G.L. Hallett-Tapley, J.C. Netto-Ferreira, E.I. Alarcon, J.C. Scaiano, Size-controlled Photochemical Synthesis of Niobium Nanoparticles, Dalton Trans., 42 (2013) 14049-14052.
[112] O. Shvydkiv, A. Yavorskyy, S.B. Tan, K. Nolan, N. Hoffmann, A. Youssef, M. Oelgemoller, Microphotochemistry: a Reactor Comparison Study Using the Photosensitized Addition of Isopropanol to Furanones as a Model Reaction, Photochem. & Photobiolog. Sci., 10 (2011) 1399-1404.
[113] Y. Fu, L. Liu, H.-Z. Yu, Y.-M. Wang, Q.-X. Guo, Quantum-Chemical Predictions of Absolute Standard Redox Potentials of Diverse Organic Molecules and Free Radicals in Acetonitrile, J. Am. Chem. Soc., 127 (2005) 7227-7234.
[114] M.C. Rath, Y. Sunitha, H.N. Ghosh, S.K. Sarkar, T. Mukherjee, Investigation of the Dynamics of Radiolytic Formation of ZnO Nanostructured Materials by Pulse Radiolysis, Radiat. Phys. Chem., 78 (2009) 77-80.
[115] V. Čuba, T. Gbur, V. Múčka, M. Nikl, R. Kučerková, M. Pospíšil, I. Jakubec, Properties of ZnO Nanocrystals Prepared by Radiation Method, Radiat. Phys. Chem., 79 (2010) 27-32.
[116] T. Gbur, V. Čuba, V. Múčka, M. Nikl, K. Knížek, M. Pospíšil, I. Jakubec, Photochemical Preparation of ZnO Nanoparticles, J. Nanopart. Res., 13 (2011) 4529-4537.
[117] K. Kamada, K. Horiguchi, T. Hyodo, Y. Shimizu, Photochemical Synthesis of Monodispersed Ceria Nanocrystals in Simple Cerium Nitrate Solution without Additives, Crystal Growth & Design, 11 (2011) 1202-1207.
[118] B.L. Evans, A.D. Yoffe, Structure and Stability of Inorganic Azides. II. Some Physical and Optical Properties, and the Fast Decomposition of Solid Monovalent Inorganic Azides, Proceedings of the Royal Society of London A: Mathematical, Physical and Engineering Sciences, 250 (1959) 346-366.
[119] D. Habibi, M. Nasrollahzadeh, T.A. Kamali, Green synthesis of the 1-substituted 1H-1,2,3,4-tetrazoles by application of the Natrolite zeolite as a new and reusable heterogeneous catalyst, Green Chem., 13 (2011) 3499-3504.
[120] K. Nishioka, Y. Niidome, S. Yamada, Photochemical Reactions of Ketones to Synthesize Gold Nanorods, Langmuir, 23 (2007) 10353-10356.
[121] Y. Yonezawa, T. Sato, M. Ohno, H. Hada, Photochemical formation of colloidal metals, Journal of the Chemical Society, Faraday Transact. 1: Physical Chemistry in Condensed Phases, 83 (1987) 1559-1567.
[122] R. Muthivhi, S. Parani, B. May, O.S. Oluwafemi, Green Synthesis of Gelatin-noble Metal Polymer Nanocomposites for Sensing of Hg Ions in Aqueous Media, Nano-Structures & Nano-Objects, 13 (2018) 132-138.

[123] W.-y. Huang, G.-c. Xu, Characterization of Nano-Ag/PVP Composites Synthesized via Ultra-violet Irradiation, Journal of Coal Science and Engineering (China), 16 (2010) 188-192.
[124] Y. Li, M.A. El-Sayed, The Effect of Stabilizers on the Catalytic Activity and Stability of Pd Colloidal Nanoparticles in the Suzuki Reactions in Aqueous Solution†, J. Phys. Chem. B, 105 (2001) 8938-8943.
[125] R. Narayanan, M.A. El-Sayed, Effect of Catalysis on the Stability of Metallic Nanoparticles: Suzuki Reaction Catalyzed by PVP-Palladium Nanoparticles, J. Am. Chem. Soc., 125 (2003) 8340-8347.
[126] L.K. Yeung, R.M. Crooks, Heck Heterocoupling within a Dendritic Nanoreactor, Nano Lett., 1 (2001) 14-17.
[127] N.R. Jana, Z.L. Wang, T. Pal, Redox Catalytic Properties of Palladium Nanoparticles: Surfactant and Electron Donor−Acceptor Effects, Langmuir, 16 (2000) 2457-2463.
[128] P.V. Viet, B.T. Phan, D. Mott, S. Maenosono, T.T. Sang, C.M. Thi, L.V. Hieu, Silver nanoparticle loaded TiO_2 nanotubes with high photocatalytic and antibacterial activity synthesized by photoreduction method, J. Photochem.Photobio. A: Chemistry, 352 (2018) 106-112.
[129] M. Sun, Y. Fang, Y. Kong, X. Yuan, J. Shi, A. Umar, Direct in situ Synthesis of Fe_2O_3-codoped N-doped TiO_2 Nanoparticles with Enhanced Photocatalytic and Photo-electrochemical Properties, J. Alloys Compd., 705 (2017) 89-97.
[130] S. Scirè, C. Crisafulli, S. Giuffrida, C. Mazza, P.M. Riccobene, A. Pistone, G. Ventimiglia, C. Bongiorno, C. Spinella, Supported Silver Catalysts Prepared by Deposition in Aqueous Solution of Ag Nanoparticles Obtained through a Photochemical Approach, Appl. Catal. A, 367 (2009) 138-145.
[131] E. Elmalem, A.E. Saunders, R. Costi, A. Salant, U. Banin, Growth of Photocatalytic CdSe–Pt Nanorods and Nanonets, Adv. Mater., 20 (2008) 4312-4317.
[132] M. Behrens, Coprecipitation: An Excellent Tool for the Synthesis of Supported Metal Catalysts – from the Understanding of the well known Recipes to New Materials, Catal. Today, 246 (2015) 46-54.
[133] A. Wood, M. Giersig, P. Mulvaney, Fermi Level Equilibration in Quantum Dot−Metal Nanojunctions, J. Phys. Chem. B, 105 (2001) 8810-8815.
[134] P.D. Cozzoli, R. Comparelli, E. Fanizza, M.L. Curri, A. Agostiano, D. Laub, Photocatalytic Synthesis of Silver Nanoparticles Stabilized by TiO_2 Nanorods: A Semiconductor/Metal Nanocomposite in Homogeneous Nonpolar Solution, J. Am. Chem. Soc., 126 (2004) 3868-3879.
[135] A. Takai, P.V. Kamat, Capture, Store, and Discharge. Shuttling Photogenerated Electrons across TiO_2–Silver Interface, ACS Nano, 5 (2011) 7369-7376.
[136] W.-W. Zhan, Q.-L. Zhu, S. Dang, Z. Liu, M. Kitta, K. Suenaga, L.-S. Zheng, Q. Xu, Synthesis of Highly Active Sub-Nanometer Pt@Rh Core–Shell Nanocatalyst via a Photochemical Route: Porous Titania Nanoplates as a Superior Photoactive Support, Small, 13 (2017) 1603879-n/a.
[137] T. Mokari, E. Rothenberg, I. Popov, R. Costi, U. Banin, Selective Growth of Metal Tips onto Semiconductor Quantum Rods and Tetrapods, Science, 304 (2004) 1787-1790.
[138] K.L. McGilvray, M.R. Decan, D. Wang, J.C. Scaiano, Facile Photochemical Synthesis of Unprotected Aqueous Gold Nanoparticles, J. Am. Chem. Soc., 128 (2006) 15980-15981.

[139] S. Imamura, T. Higashihara, Y. Saito, H. Aritani, H. Kanai, Y. Matsumura, N. Tsuda, Decomposition of Methanol on Pt-loaded Ceria, Catal. Today, 50 (1999) 369-380.
[140] Y.L. Chen, L.-C. Kuo, M.L. Tseng, H.M. Chen, C.-K. Chen, H.J. Huang, R.-S. Liu, D.P. Tsai, ZnO nanorod optical disk photocatalytic reactor for photodegradation of methyl orange, Opt. Express, 21 (2013) 7240-7249.
[141] P. Wang, B. Huang, Y. Dai, M.H. Whangbo, Plasmonic photocatalysts: harvesting visible light with noble metal nanoparticles, Phys. Chem. Chem. Phys. PCCP, 14 (2012) 9813-9825.
[142] A. Kadam, R. Dhabbe, D.-S. Shin, K. Garadkar, J. Park, Sunlight driven high photocatalytic activity of Sn doped N-TiO_2 nanoparticles synthesized by a microwave assisted method, Ceramics International, 43 (2017) 5164-5172.
[143] M. Abid, S. Bouattour, A.M. Ferraria, D.S. Conceição, A.P. Carapeto, L.F. Vieira Ferreira, A.M. Botelho do Rego, M.M. Chehimi, M. Rei Vilar, S. Boufi, Facile functionalization of cotton with nanostructured silver/titania for visible-light plasmonic photocatalysis, Journal of Colloid and Interface Science, 507 (2017) 83-94.
[144] C. Langhammer, Z. Yuan, I. Zorić, B. Kasemo, Plasmonic Properties of Supported Pt and Pd Nanostructures, Nano Lett., 6 (2006) 833-838.
[145] P. Christopher, H. Xin, S. Linic, Visible-light-enhanced Catalytic Oxidation Reactions on Plasmonic Silver Nanostructures, Nat. Chem., 3 (2011) 467-472.
[146] H.A. Atwater, A. Polman, Plasmonics for Improved Photovoltaic Devices, Nat. Mater., 9 (2010) 205-213.
[147] G. Baffou, R. Quidant, Nanoplasmonics for Chemistry, Chem. Soc. Rev., 43 (2014) 3898-3907.
[148] C. Hu, T. Peng, X. Hu, Y. Nie, X. Zhou, J. Qu, H. He, Plasmon-induced Photodegradation of Toxic Pollutants with Ag-AgI/Al2O3 under Visible-light Irradiation, J. Am. Chem. Soc., 132 (2010) 857-862.
[149] E. Kowalska, O.O. Mahaney, R. Abe, B. Ohtani, Visible-light-induced photocatalysis through surface plasmon excitation of gold on titania surfaces, Phys.Cchem. Chem. Phys. PCCP, 12 (2010) 2344-2355.
[150] W.J. Youngblood, S.-H.A. Lee, Y. Kobayashi, E.A. Hernandez-Pagan, P.G. Hoertz, T.A. Moore, A.L. Moore, D. Gust, T.E. Mallouk, Photoassisted Overall Water Splitting in a Visible Light-Absorbing Dye-Sensitized Photoelectrochemical Cell, J. Am. Chem. Soc., 131 (2009) 926-927.
[151] A. Tcherniak, J.W. Ha, S. Dominguez-Medina, L.S. Slaughter, S. Link, Probing a Century Old Prediction One Plasmonic Particle at a Time, Nano Lett., 10 (2010) 1398-1404.
[152] L. Wang, C. Clavero, Z. Huba, K.J. Carroll, E.E. Carpenter, D. Gu, R.A. Lukaszew, Plasmonics and Enhanced Magneto-optics in Core-shell Co-Ag Nanoparticles, Nano Lett., 11 (2011) 1237-1240.
[153] Z. Wang, J. Liu, W. Chen, Plasmonic Ag/AgBr Nanohybrid: Synergistic Effect of SPR with Photographic Sensitivity for Enhanced Photocatalytic Activity and Stability, Dalton Trans., 41 (2012) 4866-4870.
[154] E.A. Betterton, Environmental Fate of Sodium Azide Derived from Automobile Airbags, Crit. Rev. Environ. Sci. Technol., 33 (2003) 423-458.
[155] Y. Hu, J. Chen, X. Xue, T. Li, Y. Xie, Room-Temperature Irradiation Route To Synthesize a Large-Scale Single-Crystalline ZnO Hexangular Prism, Inorg. Chem., 44 (2005) 7280-7282.

[156] S. Giuffrida, L.L. Costanzo, G. Ventimiglia, C. Bongiorno, Photochemical Synthesis of Copper Nanoparticles Incorporated in Poly(vinyl pyrrolidone), J. Nanopart. Res., 10 (2008) 1183-1192.
[157] P.W.M. Jacobs, A.R.T. Kureishy, The Photochemical Decomposition of Sodium Azide, Can. J. Chem., 44 (1966) 703-709.
[158] K. Zoschke, H. Börnick, E. Worch, Vacuum-UV radiation at 185 nm in Water Treatment – A review, Water Research, 52 (2014) 131-145.
[159] K. Mallick, M.J. Witcomb, M.S. Scurrell, Polymer Stabilized Silver Nanoparticles: A Photochemical Synthesis Route, J. Mater.Sci., 39 4459-4463.
[160] S. Kapoor, T. Mukherjee, Photochemical Formation of Copper Nanoparticles in Poly(N-vinylpyrrolidone), Chem. Phys. Lett., 370 (2003) 83-87.
[161] A. Nezamzadeh-Ejhieh, M. Karimi-Shamsabadi, Comparison of Photocatalytic Efficiency of Supported CuO onto Micro and Nano Particles of Zeolite X in Photodecolorization of Methylene blue and Methyl orange Aqueous Mixture, Appl.Catal.A, 477 (2014) 83-92.
[162] Z. Li, R. Liu, Y. Xu, Larger Effect of Sintering Temperature Than Particle Size on the Photocatalytic Activity of Anatase TiO_2, J. Phys. Chem. C, 117 (2013) 24360-24367.
[163] J.G. Li, T. Ikegami, J.H. Lee, T. Mori, Characterization and sintering of nanocrystalline CeO_2 powders synthesized by a mimic alkoxide method, Acta Mater., 49 (2001) 419-426.
[164] M.A. Gondal, T.A. Saleh, Q.A. Drmosh, Synthesis of nickel oxide nanoparticles using pulsed laser ablation in liquids and their optical characterization, Appl. Surf. Sci., 258 (2012) 6982-6986.
[165] S. Tsunekawa, K. Ishikawa, Z.Q. Li, Y. Kawazoe, A. Kasuya, Origin of Anomalous Lattice Expansion in Oxide Nanoparticles, Phys. Rev. Lett., 85 (2000) 3440-3443.
[166] E.K. Goharshadi, S. Samiee, P. Nancarrow, Fabrication of cerium oxide nanoparticles: Characterization and optical properties, J. Colloid Interface Sci., 356 (2011) 473-480.
[167] D. Marrocchelli, S.R. Bishop, H.L. Tuller, B. Yildiz, Understanding Chemical Expansion in Non-Stoichiometric Oxides: Ceria and Zirconia Case Studies, Adv. Funct. Mater., 22 (2012) 1958-1965.
[168] F. Zhang, S.-W. Chan, J.E. Spanier, E. Apak, Q. Jin, R.D. Robinson, I.P. Herman, Cerium Oxide Nanoparticles: Size-selective Formation and Structure Analysis, Appl. Phys. Lett., 80 (2002) 127-129.
[169] P. Dutta, S. Pal, M.S. Seehra, Y. Shi, E.M. Eyring, R.D. Ernst, Concentration of Ce3+ and Oxygen Vacancies in Cerium Oxide Nanoparticles, Chem. Mater., 18 (2006) 5144-5146.
[170] B. Choudhury, P. Chetri, A. Choudhury, Annealing Temperature and Oxygen-vacancy-dependent Variation of Lattice Strain, Band Gap and Luminescence Properties of CeO_2 Nanoparticles, J. Exp. Nanosci., 10 (2015) 103-114.
[171] I. Kosacki, V. Petrovsky, H.U. Anderson, P. Colomban, Raman Spectroscopy of Nanocrystalline Ceria and Zirconia Thin Films, J. Am. Ceram. Soc., 85 (2002) 2646-2650.
[172] S. Phokha, S. Pinitsoontorn, P. Chirawatkul, Y. Poo-arporn, S. Maensiri, Synthesis, characterization, and magnetic properties of monodisperse CeO2 nanospheres prepared by PVP-assisted hydrothermal method, Nanoscale Res. Lett., 7 (2012) 1-13.

[173] V. Bolis, G. Magnacca, G. Cerrato, C. Morterra, Microcalorimetric and IR-spectroscopic Study of the Room Temperature Adsorption of CO_2 on Pure and Sulphated t-ZrO_2, Thermochim. Acta, 379 (2001) 147-161.
[174] A. Azam, A.S. Ahmed, M. Oves, M.S. Khan, S.S. Habib, A. Memic, Antimicrobial activity of metal oxide nanoparticles against Gram-positive and Gram-negative bacteria: a comparative study, Int. J. Nanomed., 7 (2012) 6003-6009.
[175] K. Mohan Kumar, B.K. Mandal, K. Siva Kumar, P. Sreedhara Reddy, B. Sreedhar, Biobased Green Method to Synthesise Palladium and Iron Nanoparticles using Terminalia Chebula Aqueous Extract, Spectrochim. Acta, Part A, 102 (2013) 128-133.
[176] I. Rawal, Facial Synthesis of Hexagonal Metal Oxide Nanoparticles for Low Temperature Ammonia Gas Sensing Applications, RSC Adv., 5 (2015) 4135-4142.
[177] A.A. Ansari, P.R. Solanki, B.D. Malhotra, Hydrogen Peroxide Sensor Based on Horseradish Peroxidase Immobilized Nanostructured Cerium Oxide Film, J. Biotechnol., 142 (2009) 179-184.
[178] R. Si, Y.-W. Zhang, L.-P. You, C.-H. Yan, Self-Organized Monolayer of Nanosized Ceria Colloids Stabilized by Poly(vinylpyrrolidone), J. Phys. Chem. B, 110 (2006) 5994-6000.
[179] Y. Wang, F. Wang, Q. Song, Q. Xin, S. Xu, J. Xu, Heterogeneous Ceria Catalyst with Water-Tolerant Lewis Acidic Sites for One-Pot Synthesis of 1,3-Diols via Prins Condensation and Hydrolysis Reactions, J. Am. Chem. Soc., 135 (2013) 1506-1515.
[180] A.S. Deshpande, N. Pinna, P. Beato, M. Antonietti, M. Niederberger, Synthesis and Characterization of Stable and Crystalline $Ce_{1-x}Zr_xO_2$ Nanoparticle Sols, Chem. Mater., 16 (2004) 2599-2604.
[181] A. Elbourne, S. Cronshaw, K. Voitchovsky, G.G. Warr, R. Atkin, Near surface properties of mixtures of propylammonium nitrate with n-alkanols 1. Nanostructure, Phys. Chem. Chem. Phys., 17 (2015) 26621-26628.
[182] O. Spalla, P. Kékicheff, Adhesion between Oxide Nanoparticles: Influence of Surface Complexation, J. Coll.Inter. Sci., 192 (1997) 43-65.
[183] H.S. Potdar, D.-W. Jeong, K.-S. Kim, H.-S. Roh, Synthesis of Highly Active Nano-Sized Pt/CeO2 Catalyst via a Cerium Hydroxy Carbonate Precursor for Water Gas Shift Reaction, Catal. Lett., 141 (2011) 1268-1274.
[184] C. Ho, J.C. Yu, T. Kwong, A.C. Mak, S. Lai, Morphology-Controllable Synthesis of Mesoporous CeO2 Nano- and Microstructures, Chem. Mater., 17 (2005) 4514-4522.
[185] L. Truffault, M.-T. Ta, T. Devers, K. Konstantinov, V. Harel, C. Simmonard, C. Andreazza, I.P. Nevirkovets, A. Pineau, O. Veron, J.-P. Blondeau, Application of Nanostructured Ca doped CeO_2 for Ultraviolet Filtration, Mater. Res. Bull., 45 (2010) 527-535.
[186] S. Samiee, E.K. Goharshadi, Effects of different precursors on size and optical properties of ceria nanoparticles prepared by microwave-assisted method, Mater. Res. Bull., 47 (2012) 1089-1095.
[187] S. Tsunekawa, J.-T. Wang, Y. Kawazoe, A. Kasuya, Blueshifts in the Utraviolet Absorption Spectra of Cerium Oxide Nanocrystallites, J. Appl. Phys., 94 (2003) 3654-3656.
[188] T. Masui, K. Fujiwara, K.-i. Machida, G.-y. Adachi, T. Sakata, H. Mori, Characterization of Cerium(IV) Oxide Ultrafine Particles Prepared Using Reversed Micelles, Chem. Mat., 9 (1997) 2197-2204.

[189] P. Patsalas, S. Logothetidis, L. Sygellou, S. Kennou, Structure-dependent electronic properties of nanocrystalline cerium oxide films, Phys. Rev. B, 68 (2003) 035104.
[190] E. Raudonyte-Svirbutaviciene, L. Mikoliunaite, A. Drabavicius, R. Juskenas, S. Sakirzanovas, T. Justel, A. Katelnikovas, Photochemical Synthesis of CeO_2 Nanoscale Particles Using Sodium Azide as a Photoactive Material: Effects of the Annealing Temperature and Polyvinylpyrrolidone Addition, RSC Adv., 6 (2016) 107065-107074.
[191] K.K. Nanda, A. Maisels, F.E. Kruis, H. Fissan, S. Stappert, Higher Surface Energy of Free Nanoparticles, Phys. Rev. Lett., 91 (2003) 106102.
[192] G. Dukovic, M.G. Merkle, J.H. Nelson, S.M. Hughes, A.P. Alivisatos, Photodeposition of Pt on Colloidal CdS and CdSe/CdS Semiconductor Nanostructures, Adv. Mater., 20 (2008) 4306-4311.
[193] H. Yu, Q. Zhang, H. Liu, M. Dahl, J.B. Joo, N. Li, L. Wang, Y. Yin, Thermal synthesis of Silver Nanoplates Revisited: a Modified Photochemical Process, ACS Nano, 8 (2014) 10252-10261.
[194] J.E. Millstone, S.J. Hurst, G.S. Métraux, J.I. Cutler, C.A. Mirkin, Colloidal Gold and Silver Triangular Nanoprisms, Small, 5 (2009) 646-664.
[195] H. Yu, Q. Zhang, H. Liu, M. Dahl, J.B. Joo, N. Li, L. Wang, Y. Yin, Thermal Synthesis of Silver Nanoplates Revisited: A Modified Photochemical Process, ACS Nano, 8 (2014) 10252-10261.
[196] Y. Xia, N.J. Halas, Shape-Controlled Synthesis and Surface Plasmonic Properties of Metallic Nanostructures, MRS Bulletin, 30 (2005) 338-348.
[197] S. Link, M.A. El-Sayed, Spectral Properties and Relaxation Dynamics of Surface Plasmon Electronic Oscillations in Gold and Silver Nanodots and Nanorods, J. Phys. Chem. B, 103 (1999) 8410-8426.
[198] S. Eustis, M.A. El-Sayed, Why Gold Nanoparticles are More Precious than Pretty Gold: Noble Metal Surface Plasmon Resonance and its Enhancement of the Radiative and Nonradiative Properties of Nanocrystals of Different Shapes, Chem. Soc. Rev., 35 (2006) 209-217.
[199] R. Jin, Y. Charles Cao, E. Hao, G.S. Metraux, G.C. Schatz, C.A. Mirkin, Controlling Anisotropic Nanoparticle Growth through Plasmon Excitation, Nature, 425 (2003) 487-490.
[200] Q. Zhang, J. Ge, T. Pham, J. Goebl, Y. Hu, Z. Lu, Y. Yin, Reconstruction of Silver Nanoplates by UV Irradiation: Tailored Optical Properties and Enhanced Stability, Angew. Chem., 121 (2009) 3568-3571.
[201] M.A. Behnajady, N. Modirshahla, R. Hamzavi, Kinetic study on Photocatalytic Degradation of C.I. Acid Yellow 23 by ZnO Photocatalyst, J. Hazard. Mater., 133 (2006) 226-232.
[202] K. Krumova, G. Cosa, Chapter 1 Overview of Reactive Oxygen Species, in: Singlet Oxygen: Applications in Biosciences and Nanosciences, Volume 1, The Royal Society of Chemistry, 2016, pp. 1-21.
[203] M. Chen, L.Y. Wang, J.T. Han, J.Y. Zhang, Z.Y. Li, D.J. Qian, Preparation and Study of Polyacryamide-stabilized Silver Nanoparticles through a one-pot Process, J. Phys. Chem. B, 110 (2006) 11224-11231.
[204] J. Lee, J.D. Fortner, J.B. Hughes, J.-H. Kim, Photochemical Production of Reactive Oxygen Species by C60 in the Aqueous Phase During UV Irradiation, Environ. Sci. Techn., 41 (2007) 2529-2535.

[205] L. Jakob, T.M. Hashem, S. Bürki, N.M. Guindy, A.M. Braun, Vacuum-ultraviolet (VUV) photolysis of water: oxidative degradation of 4-chlorophenol, Journal of Photochem.Photobio. A: Chemistry, 75 (1993) 97-103.
[206] The absolute energy positions of conduction and valence bands of selected semiconducting minerals, Am. Min., 85 (2000) 543-556.
[207] S. Kim, J.S. Lee, C. Mitterbauer, Q.M. Ramasse, M.C. Sarahan, N.D. Browning, H.J. Park, Anomalous Electrical Conductivity of Nanosheaves of CeO_2, Chem. Mater., 21 (2009) 1182-1186.
[208] A. Corma, P. Atienzar, H. Garcia, J.-Y. Chane-Ching, Hierarchically Mesostructured Doped CeO_2 with Potential for Solar-cell Use, Nat. Mater., 3 (2004) 394-397.
[209] S. Robl, M. Worner, D. Maier, A.M. Braun, Formation of hydrogen peroxide by VUV-photolysis of water and aqueous solutions with methanol, Photochem. & Photobio. Sci., 11 (2012) 1041-1050.
[210] G.V. Buxton, C.L. Greenstock, W.P. Helman, A.B. Ross, Critical Review of Rate Constants for Reactions of Hydrated Electrons, Hydrogen Atoms and Hydroxyl Radicals (·OH/·O−) in Aqueous Solution, J. Phys. Chem. Ref. Data, 17 (1988) 513-886.
[211] W. Choi, M.R. Hoffmann, Photoreductive Mechanism of CCl_4 Degradation on TiO_2 Particles and Effects of Electron Donors, Environ. Sci. Techn., 29 (1995) 1646-1654.
[212] H. Hada, Y. Yonezawa, A. Yoshida, A. Kurakake, Photoreduction of Silver ion in Aqueous and Alcoholic Solutions, J. Phys. Chem., 80 (1976) 2728-2731.
[213] N. Sasirekha, P. Sangeetha, Y.-W. Chen, Bimetallic Au–Ag/CeO_2 Catalysts for Preferential Oxidation of CO in Hydrogen-Rich Stream: Effect of Calcination Temperature, J. Phys. Chem. C, 118 (2014) 15226-15233.
[214] A.M. Ferraria, A.P. Carapeto, A.M. Botelho do Rego, X-ray Photoelectron Spectroscopy: Silver Salts Revisited, Vacuum, 86 (2012) 1988-1991.
[215] P. Prieto, V. Nistor, K. Nouneh, M. Oyama, M. Abd-Lefdil, R. Díaz, XPS Study of Silver, Nickel and Bimetallic Silver–Nickel Nanoparticles Prepared by Seed-mediated Growth, Appl. Surf. Sci., 258 (2012) 8807-8813.
[216] M. Gozdziewska, G. Cichowicz, K. Markowska, K. Zawada, E. Megiel, Nitroxide-coated Silver Nanoparticles: Synthesis, Surface Physicochemistry and Antibacterial Activity, RSC Adv., 5 (2015) 58403-58415.
[217] X. Tang, J. Chen, Y. Li, Y. Li, Y. Xu, W. Shen, Complete oxidation of formaldehyde over Ag/MnOx–CeO2 catalysts, Chem. Eng. J., 118 (2006) 119-125.
[218] G.I.N. Waterhouse, G.A. Bowmaker, J.B. Metson, Oxidation of a Polycrystalline Silver Foil by Reaction with Ozone, Appl. Surf. Sci., 183 (2001) 191-204.
[219] B. Wiley, T. Herricks, Y. Sun, Y. Xia, Polyol Synthesis of Silver Nanoparticles: Use of Chloride and Oxygen to Promote the Formation of Single-Crystal, Truncated Cubes and Tetrahedrons, Nano Lett., 4 (2004) 1733-1739.
[220] X. Lu, H.-Y. Tuan, J. Chen, Z.-Y. Li, B.A. Korgel, Y. Xia, Mechanistic Studies on the Galvanic Replacement Reaction between Multiply Twinned Particles of Ag and $HAuCl_4$ in an Organic Medium, J. Am. Chem. Soc., 129 (2007) 1733-1742.
[221] S. George, S. Lin, Z. Ji, C.R. Thomas, L. Li, M. Mecklenburg, H. Meng, X. Wang, H. Zhang, T. Xia, J.N. Hohman, S. Lin, J.I. Zink, P.S. Weiss, A.E. Nel, Surface Defects on Plate-Shaped Silver Nanoparticles Contribute to Its Hazard Potential in a Fish Gill Cell Line and Zebrafish Embryos, ACS Nano, 6 (2012) 3745-3759.

[222] V.V. Pinto, M.J. Ferreira, R. Silva, H.A. Santos, F. Silva, C.M. Pereira, Long Time Effect on the Stability of Silver Nanoparticles in Aqueous Medium: Effect of the Synthesis and Storage Conditions, Colloids and Surfaces A: Physicochemical and Engineering Aspects, 364 (2010) 19-25.
[223] A. Henglein, M. Giersig, Formation of Colloidal Silver Nanoparticles: Capping Action of Citrate, J. Phys. Chem. B, 103 (1999) 9533-9539.
[224] J.G. Rodríguez, O. Solaun, J. Larreta, M.J. Belzunce Segarra, J. Franco, J. Ignacio García Alonso, C. Sariego, V. Valencia, Á. Borja, Baseline of Butyltin Pollution in Coastal Sediments within the Basque Country (northern Spain), in 2007–2008, Mar. Pollut. Bull., 60 (2010) 139-145.
[225] B.R. Ganapuram, M. Alle, R. Dadigala, Catalytic Reduction of Methylene Blue and Congo Red Dyes Using Green Synthesized Gold Nanoparticles Capped by Salmalia Malabarica gum, Int. Nano Lett., 5 (2015).
[226] K. Duhamel, G. Blanchard, G. Dorange, G. Martin, Recovery of all Species from Photolytic Degradation of Tributyltin Compounds TBTX (X = Cl, OSn Bu3), Appl. Organom. Chem., 1 (1987) 133-142.
[227] A. Cruz, A.M. Anselmo, S. Suzuki, S. Mendo, Tributyltin (TBT): A Review on Microbial Resistance and Degradation, Critical Reviews in Environ. Sci. Techn., 45 (2015) 970-1006.
[228] E.D. Goldberg, TBT: An Environmental Dilemma, Environ., 28 (1986) 17-44.
[229] J. Muff, M.E. Simonsen, E.G. Søgaard, Removal of Tributyltin from Contaminated Seawater by Combinations of Photolytic and TiO2 Mediated Photocatalytic Processes, J. Environ.l Chem. Engin., 5 (2017) 3201-3206.
[230] Y. Zhao, Z. Huang, W. Chang, C. Wei, X. Feng, L. Ma, X. Qi, Z. Li, Microwave-assisted Solvothermal Synthesis of Hierarchical TiO_2 Microspheres for Efficient Electro-field-assisted-Photocatalytic Removal of Tributyltin in Tannery Wastewater, Chemosphere, 179 (2017) 75-83.

ACKNOWLEDGEMENTS

Finally, the day has come when I can put a finishing touch on this dissertation by expressing my gratitude to all the people who guided and supported me throughout this long and adventurous scientific journey.

First of all I would like to thank my supervisor, Assoc. Prof. Dr. Arturas Katelnikovas whose maddening attention to detail drove me to gain new perspectives. This thesis would not have seen the light of day without the lamps constructed (and repaired after some misterious incidents) by him. I am also grateful to my scientific consultant Prof. Dr. Thomas Jüstel for all the useful advices and prompt answers to my questions.

Nothing would have been possible without collaborations and I sure was lucky to have fruitful ones. Foremost, I would like to thank Prof. Dr. Vida Vičkačkaitė not only for the GC/MS measurements, but also for the trust in my ideas and her contagious enthusiasm. I am thankful to Dr. Vitalija Jasulaitienė for XPS measurements, Dr. Aleksej Žarkov for ICP-OES, Olga Opuchovič for TG-DTG analysis, Dr. Lina Mykoliūnaitė for Raman spectroscopy measurements, Dr. Linas Vilčiauskas for valuable observations and to Prof. Dr. Simas Šakirzanovas for the working place.

I also want to express my gratitude to Prof. Dr. Aivaras Kareiva and Prof. Dr.Stasys Tautkus. Whenever I had problems related to the study process, internships or equipment, I knew they would not refuse to help.

My collegues from Nature Research center, especially my boss Dr. Kęstutis Jokšas, deserve a special thanks for all the support and encouragement they gave.

I am super happy to have had the chance to join Prof. Dr. Gunnar Svenssons group at MMK, Stockholm university. Thank you, Prof. Svensson, for the warm welcome and all the help provided. Dr. Cheuk Wai-Tai should be acknowledged for the valuable lessons on TEM and for the patience of a saint during the trainings. I am also indebted to Assoc. Prof. Dr. Germán Salazar Alvarez who has offered much advice and insight throughout my work. A special thanks goes to a future doctor Alexandra Neagu: not only did she borrow me books and other stuff, gave useful tips and did all the important job with TEM, but also did she become one of my closest friends in Stockholm.

Staying in Padova was by no means less amazing for which I am mostly thankful to my supervisors, Prof. Dr. Gaetano Granozzi and Assoc. Prof. Dr. Stefano Agnoli. Dr. Francesco Carraro deserves a separate thanks for teaching me a lot on the solvothermal synthesis and answering endless amount of questions, both on scientific and cultural topics.

I would also like to say many thanks to all the guys from MMK (Stockholm University) and SSCG (University of Padova) who made me feel at home and were always ready to lend a hand. However, most of the work was done in Vilnius University, Faculty of Chemistry and I must say it was a big pleasure to work in such a friendly and cheerful environment.

I should not forget my dear old friends who did not forgot me when I dived deep into the science. Not less am I indebted to a bunch of wonderful people met during my scientific travels. Thank you friends, not only for experiencing all the breathtaking and funny adventures together, but also for just being there when I needed the most.

Last but definitely not least, the most special thanks goes to my family. To my parents who gave me wings and have always supported me in everything I do. To my amazing grandparents for being proud of me even when there was no big reason for that. To my genius little sister who, although being significantly younger than me, has always been an inspiration. Finally, to my darling, the best husband in the world for surviving this complex period with or without (that is, during my travels) me.

Ačiū Jums, brangieji žmonės!!!